Doctoral Thesis

Thesis Title

Experimental Studies on Stacked Screen Regenerator Used for Thermoacoustic Engines

Department of Mechanical Systems and Design
Graduate school of Engineering,
TOHOKU UNIVERSITY

HSU SHU HAN

(ID No. B3TD1005)

TOHOKU UNIVERSITY
Graduate School of Engineering

Experimental Studies on Stacked Screen Regenerator Used for Thermoacoustic Engines

（熱音響エンジンに用いる積層金網蓄熱器に関する実験的研究）

A dissertation submitted for the degree of Doctor of Philosophy (Engineering)

Department of Mechanical Systems and Design

by

Shu Han HSU

October 6，2017

Experimental Studies on Stacked Screen Regenerator Used for Thermoacoustic Engines

HSU Shu Han

Abstract

A stacked-screen regenerator, made of a pile of metallic mesh screens and having numerous tortuous flow channels, was experimentally investigated by measuring acoustic fields and acoustically-driven heat powers when acoustic gas oscillations were excited in the regenerator. This thesis accomplished a method to model the regenerator with a bundle of regular cylindrical tubes with an *effective radius*—r_{eff}, which was characterized by two dimensionless parameters intrinsic to oscillatory gas flows. The knowledge of r_{eff} applicable to various oscillating flow conditions can be used for improving a thermoacoustic engine design.

The thermoacoustic engine is a novel heat engine producing large acoustic powers from supplied heat. The thermodynamic cycles responsible for the energy conversions are executed by acoustic gas oscillations in a regenerator, being a porous media with tiny flow channels, through isothermal expansion and compression. The thermoacoustic engine is potentially an alternative device of conventional mechanical heat engines because a use of acoustic waves in place of mechanical moving parts can avoid problems such as friction, piston sealing, complexity and so on. Also, the thermoacoustic engine is an external combustion engine without using any environmentally harmful working gases. This engine should serve as a durable and sustainable solution with a low manufacturing cost.

In order to achieve a high thermal efficiency comparable to mechanical heat engines, the stacked-screen regenerator is indispensable to the thermoacoustic engine because it achieves an excellent thermal contact with the working gas due to high surface-area-to-volume ratio. A full theoretical formulation of the stacked-screen regenerator, however, is generally difficult because of its tortuous pore structure. Therefore, the stacked-screen regenerator still remains an obstacle for a precise estimation of the engine performance.

In a regenerator with regular flow channels, thermal interactions between the gas and the channel walls are theoretically understood by the thermoacoustic theory derived from linearized equations of the hydrodynamics. Under the framework of the thermoacoustic theory, the present

study aims to characterize the stacked-screen regenerator with a bundle of regular cylindrical tubes, in order to improve the numerical simulation codes for practical engine design. Systematic investigations are outlined as follows.

Chapter 1 introduces the background of the present study. At the beginning, the thermoacoustic theory was devoted to understand the early observations of thermoacoustic self-sustained oscillations, and later it was recognized as the basis of the development of thermoacoustic engines. It also serves as a starting point of the current research. For the stacked-screen regenerator, a comprehensive literature review is given from two perspectives of mechanical Stirling engine and acoustical studies. On the basis of the current understanding the thermoacoustic engines and the regenerator, objectives of this study are stated.

In Chapter 2, by testing stacked-screen regenerators in either pressurized helium or argon gases at 0.45 MPa with ambient temperature, the oscillatory flow resistance is experimentally obtained from measured acoustic power decreases across the regenerator. The results are compared with three empirical equations frequently used in the Stirling and thermoacoustic engines. An empirical equation of the flow resistance proposed by Obayashi et al., parameterized with two non-dimensional parameters of Re_h and r_0/δ_ν, presents the better agreements with experimental results than the others that are given by using merely one of them, where Re_h represents the Reynolds number based on the velocity amplitude of the oscillation, and δ_ν signifies the viscous penetration depth relating to the oscillation angular frequency ω. In the empirical equation, r_0 = ($\sqrt{d_\mathrm{h}d_\mathrm{w}}/2$, where d_h and d_w respectively denote the hydraulic diameter and wire diameter of the mesh screen), is an effective radius of Ueda et al., which models tortuous flow channels of the stacked-screen regenerator as a bundle of cylindrical tubes when the velocity amplitudes are extremely small.

In Chapter 3, the capillary-tube-based modeling for the stacked-screen regenerator has been further applied to derive a velocity-dependent effective radius r_eff from the flow resistance empirical equation of Obayashi et al. Under the framework of the thermoacoustic theory, the experimental effective radius $r_\mathrm{eff,exp.}$ is numerically obtained from the measured acoustic pressure and axial acoustic particle velocity at both ends of differentially heated regenerators, in either pressurized helium or argon gases at 0.45 MPa. Agreements between r_eff and $r_\mathrm{eff,exp.}$ verify that the proposed effective radius r_eff based on uniform temperature experiments is capable of characterizing thermoacoustic power productions induced by the stacked-screen regenerator with temperature gradients.

In Chapter 4, the acoustically driven heat flow transmitted through the regenerator in the oscillatory flow of the argon gas having the mean pressure of 0.45 MPa has been measured and compared with four different empirical equations used in the thermoacoustic and Stirling engine designs. Four empirical formulations reproduce the measured heat flow rates to a similar degree. Among them, the effective radius of Ueda et al. is found to give the simplest formulation and the best accuracy. In addition, acoustic fields at both ends of the regenerator for transmitting the heat flow are measured to numerically calculate the experimental effective radius and compared with r_eff again. Results suggest that two effective pore radii r_eff and r_0 are necessary to account for the acoustic power change and the heat power flowing through the stacked-screen regenerator, respectively.

In Chapter 5, two types of the thermoacoustic engines have been built by installing the stacked-screen regenerator in the straight tube and looped tube. The spontaneous oscillations in the two engines are reported including the start-up temperature ratio and the growth of saturation oscillations. Also, based on the transfer matrix characterized by the thermoacoustic theory, a numerical calculation method using the imaginary frequency has been proposed for evaluating performances of the whole thermoacoustic engine system. The imaginary frequency indicates an attenuation/growth rate of the instantaneous amplitude of oscillations. The proposed calculation method is able to predict the start-up temperature ratio by using r_0, and also to estimate the evolutions of steady oscillations and the thermal efficiency using r_0 and r_{eff}. Calculation results are verified by two experimental cases of stacked-screen regenerators of #50 and #40 mesh numbers in the straight-tube thermoacoustic engine filled with pressurized nitrogen gas at 0.6 MPa.

In Chapter 6, each of sub-studies in this thesis is individually summarized and it is concluded that the stacked-screen regenerator is phenomenologically characterized by two effective radii r_{eff} and r_0 respectively for capturing the acoustic powers and heat powers transmitted through the regenerator. The author is convinced that the conventional evaluation methods of the thermoacoustic engine utilizing the stacked-screen regenerator are improved by using these two effective radii. Also, an outlook for improving the current study is given.

Contents

Abstract **i**

List of figures **vii**

List of tables **xiii**

List of symbols **xv**

1 Introduction **1**

1.1 Thermoacoustic oscillations and thermoacoustic heat engines 1

1.1.1 History of thermoacoustic oscillations 1

1.1.2 Theoretical studies on thermoacoustic oscillations 3

1.1.3 Types of thermoacoustic engines 6

1.2 Stacked-screen regenerator 11

1.2.1 Required flow properties 11

1.2.2 Literature review 11

1.3 Dimensional analysis 15

1.4 Objectives of this study 18

1.5 Thesis outline 19

2 Flow resistance of the stacked-screen regenerator **21**

2.1 Introduction 21

2.2 Empirical equations of viscous flow resistance 22

2.3 Experimental setup 23

2.3.1 Configuration of loudspeaker for experiment 23

2.3.2 Experimental procedure 24

2.4 Experimental results . . . 29

2.5 Conclusions . . . 32

3 Cylindrical modeling of a stacked-screen regenerator 35

3.1 Introduction . . . 35

3.1.1 Derivation of effective radius . . . 36

3.1.2 Use of effective radius . . . 37

3.2 Experimental procedure . . . 38

3.3 Derivation of experimental effective radius . . . 42

3.4 Comparisons of effective radii . . . 45

3.5 Conclusions . . . 51

4 Measurement of heat flow transmitted through regenerators 53

4.1 Introduction . . . 53

4.2 Axial heat flow estimated by empirical equations . . . 54

4.3 Experimental procedure . . . 56

4.4 Results and Discussion . . . 59

4.4.1 Regular flow channel regenerator . . . 59

4.4.2 Stacked-screen regenerator . . . 60

4.4.3 Discussion . . . 62

4.5 Conclusions . . . 66

5 Experimental verification of the effective radii 67

5.1 Introduction . . . 67

5.2 Experimental method . . . 69

5.2.1 Model thermoacoustic engines . . . 69

5.2.2 Experimental procedure . . . 70

5.3 Calculation method . . . 72

5.3.1 Transfer matrices . . . 72

5.3.2 Calculation of stability curve . . . 73

5.3.3 Calculation of oscillation amplitude . . . 74

5.4 Experimental result and discussion . . . 76

5.4.1 Stability curve 76

5.4.2 Evolution of pressure amplitude 79

5.4.3 Thermal efficiency of thermoacoustic engine and acoustic field 81

5.4.4 Discussion 83

5.5 Conclusions 83

6 Conclusions and recommendations for future work **85**

6.1 Acoustic power dissipation with uniform temperature 85

6.2 Effective radius 86

6.3 Heat transportation by oscillation flow 86

6.4 Usage of imaginary oscillation frequency 87

6.5 Outlook 87

Appendix A Experiments with high acoustic impedance **89**

A.1 Introduction 89

A.2 Experimental procedure 91

A.3 Experimental results and discussion 93

A.3.1 Constant velocity amplitude 93

A.3.2 Constant acoustic impedance 95

A.3.3 Discussion 98

A.4 Conclusions 99

Appendix B Publications **103**

B.1 Journal papers 103

B.2 Proceedings papers 103

References **105**

Acknowledgements **113**

Vita **115**

東北大学

Experimental Studies on Stacked Screen Regenerator Used for Thermoacoustic Engines

TOHOKU
UNIVERSITY

HSU Shu Han

Supervisor: Prof. BIWA Tetsushi

Graduate School of Engineering

This dissertation is submitted for the degree of
Doctor of Philosophy

Department of Mechanical
Systems and Design

October 2017

Copyright © 2017 HSU Shu Han

Typeset with XƎLaTeX document preparation system under Mac OS X TexShop software (version 3.88)
Modified from a Ph. D. thesis LaTeX template for Cambridge University Engineering Department (version 2.1),
contributed by Krishna Kumar: https://github.com/kks32/phd-thesis-template/

I would like to dedicate this thesis to my loving parents, and the Japanese god of the thermoacousitcs—吉備津彦命 (Kibitsu-hiko-no-mikoto).

Declaration

I hereby declare that this dissertation titled as “Experimental Studies on Stacked-Screen Regenerator Used for Thermoacoustic Engines” is my original work and have not been submitted in whole, or in part for any other degree or qualification in this, or any other university, except where indicated by specific reference in the contents is made to the work of others. This dissertation contains fewer than 30,000 words including equations, tables, footnotes, appendices, and references and has fewer than 45 figures.

HSU Shu Han
October 2017

List of figures

1.1 Examples of thermoacoustic oscillation systems. 2

1.2 Thermoacoustic function versus $r/\delta_\sharp$. 4

1.3 Energy flow distributions in the traveling wave engine. 6

1.4 Energy flow distributions in the standing wave engine. 7

1.5 Ceramic honeycomb catalysts, made of regular square pores. 8

1.6 The standing wave thermoacoustic engine (reproduced from Reference 16). . . 8

1.7 The standing wave thermoacoustic refrigerator applied as a beer cooler (reproduced from Reference 16). 9

1.8 Traveling wave thermoacoustic engine 10

1.9 The 4-stage traveling wave thermoacoustic engine proposed by de Blok, cited from Reference 21. 11

1.10 Stacked mesh screens used in regenerators. 12

2.1 Loudspeaker configuration. 25

2.2 Schematic diagram of the experimental setup. (Figure adapted from Reference 57 and modified by author.) 26

2.3 Photo of experimental configuration, which shows one end of the 40-mm-inner-diameter cylindrical tube and the regenerator holder. Two series speaker pairs arranged in opposite are harnessed in the one end of the cylindrical tube, where total eight loudspeakers were used in this experimental setup. 27

2.4 Measured acoustic field with #100 mesh, $|V| = 0.45$ m/s, 44 Hz, and argon gas. The black and blue curves in (a) represent the pressure amplitude $|P|$ and the amplitude $|U|$ of the cross-sectional averaged velocity, respectively. The black and blue curves in (b) represent the magnitude of acoustic impedance $|Z|$ and its phase $\arg[Z]$, respectively. Also, black lines shown in (c) represent acoustic power distributions in the upstream and downstream of the regenerator, and the acoustic power difference ΔW between the both ends of the regenerator is determined with $\Delta W = W_1 - W_2$. 28

2.5 Schematic diagram of the relation of velocity V in the regenerator and the velocity U in the pipe. The volume porosity is expressed by ϕ. 30

2.6 Acoustic power decrease ΔW versus the velocity amplitude $|V|$ of regenerators. 31

2.7 Comparisons among the experimental flow resistance R, empirical Equations (2.7), (2.8) and (2.9) for the stacked-screen regenerator, and the theoretical calculation for the ceramic honeycomb. Experimental results are shown by symbols with error bars, resistances given by Equations (2.7), (2.8) and (2.9) are shown by dashed, doted and solid lines, respectively; the theoretical resistances for the ceramic honeycomb are shown by thin lines. (Figures adapted from Reference 57 and modified by author.) 33

2.8 Comparisons between experimental flow resistance R and R_O for the stacked-screen regenerator using No. 100 mesh at various oscillation frequencies of 20, 44 and 100 Hz. Experimental results are presented by symbols with error bars. Predicted R_O values are shown by lines. (Figures adapted from Reference 57 and modified by author.) 34

3.1 Schematic diagram of the experimental setup. (Figure adapted from Reference 57 and modified by author.) 39

3.2 Acoustic field obtained with $|V| = 0.6$ m/s, $\Delta T = 250$ K and oscillation frequency = 44 Hz for Ar with mean pressure of 0.45 MPa. The black and blue curves in (a) represent the pressure amplitude $|P|$ and the amplitude $|U|$ of the cross-sectional averaged velocity, respectively. The black and blue curves in (b) represent the magnitude of acoustic impedance $|Z|$ and its phase $\arg[Z]$, respectively. Also, black lines shown in (c) represent acoustic power distributions in the upstream and downstream of the regenerator, and the thermoacoustic power production is observed between the both ends of the regenerator. 40

3.3 Examples of experiments of acoustic power conducting through the regenerator. 41

3.4 Error ε vs the radius r for the stacked-screen regenerator when the working gas is Ar. The oscillating frequency is 44.0 Hz. The mesh number is 30. The temperature difference is 100 K and $|V| = 0.427$ m/s. (Figure adapted from Reference 57 and modified by author.) 44

3.5 Comparison of the experimental effective radius $r_{\text{eff,exp}}$ and the actual flow channel size of the ceramic honeycomb. Experimental results are shown by symbols. The horizontal line represents one-half of the hydraulic diameter (= 340 μm). (Figure adapted from Reference 57 and modified by author.) 44

3.6 Comparison between the experimental effective radius $r_{\text{eff,exp}}$ with error bars and the predicted r_{eff} obtained using the empirical equation of Obayashi et al. for stacked-screen regenerators, where (a)–(d) show the results for Ar. Experimental results are shown by symbols with error bars; predicted values are shown by curves. (Figures adapted from Reference 57 and modified by author.) 46

3.7 Comparison between the experimental effective radius $r_{\text{eff,exp}}$ with error bars and the predicted r_{eff} obtained using the empirical equation of Obayashi et al. for stacked-screen regenerators, where (a)–(d) show the results for He. Experimental results are shown by symbols with error bars; predicted values are shown by curves. (Figures adapted from Reference 57 and modified by author.) 47

3.8 Comparison between the experimental effective radius $r_{\text{eff,exp}}$ of #100 mesh screens with error bars and predicted r_{eff} obtained using the empirical equation of Obayashi et al. at oscillation frequencies of 20 and 100 Hz, in (a) and (b), respectively, for Ar. Experimental results are shown by symbols with error bars. Predictions are shown by the curves. (Figures adapted from Reference 57 and modified by author.) 49

3.9 Comparison between the experimental effective radius $r_{\text{eff,exp}}$ of #100 mesh screens with error bars and predicted r_{eff} obtained using the empirical equation of Obayashi et al. at oscillation frequencies of 20 and 100 Hz, in (a) and (b), respectively, for He. Experimental results are shown by symbols with error bars. Predictions are shown by curves. (Figures adapted from Reference 57 and modified by author.) 50

4.1 Schematic diagram of the experimental setup. (Figure adapted from Reference 64 and modified by author.) 58

4.2 Comparison between the experimental heat flow rate $|Q|$ and theoretical calculations is given by Equation (4.3) for the ceramic honeycomb catalyst, where experimentally obtained results are shown as symbols with error bars. The theoretical calculations of $|Q|$ and $|Q_{\text{D}}|$ are shown respectively as solid and dashed curves. (Figure adapted from Reference 64 and modified by author.) 60

4.3 Experimental heat flow rate $|Q|$ and predictions given by respective empirical equations cited in this study for stacked-screen regenerators tested in pressurized helium gas with 0.45 MPa and with oscillation frequency of 200 Hz. Each panel presents identical experimentally obtained results by symbols with error bars. The empirical predictions are given respectively as (a) for Ueda et al.; (b) for Swift and Ward; (c) for Tanaka et al.; (d) for Gedeon and Wood. (Figures adapted from Reference 64 and modified by author.) 61

4.4 Comparisons between the experimental heat flow $|Q|$ and predictions given by the empirical equations. The mesh number of the stacked screens is #30. The working gas is Ar gas with 0.45 MPa. The test frequencies are 140, 180, and 200 Hz. Every panel presents the same experimentally obtained results by symbols with error bars, and empirical predictions are given respectively as the following: (a) for Ueda et al.; (b) for Swift and Ward; (c) for Tanaka et al.; (d) for Gedeon and Wood. (Figures adapted from Reference 64 and modified by author.) . . . 62

4.5 Relation between $\mathrm{Im}\left[g_\mathrm{D}\right]$ and r/δ_α. The curve of $\mathrm{Im}\left[g_\mathrm{D}\right]$ was calculated from the thermoacoustic theory. The symbols represent the experimental values evaluated from Equation (4.16) with measured data and the thermal properties of the gas at the hot end of the regenerator (T_H=543 K). (Figure adapted from Reference 64 and modified by author.) 63

4.6 Relation between r_eff and $|V|$. Symbols represent the experimental effective radius of the stacked-screen regenerator of #30 mesh and # 80 mesh. The curve stands for Equation (4.17) with thermal properties of the gas determined from a temperature averaged in T_R and T_H. The horizontal dashed line represents the effective radius r_0 of Ueda et al. (Figure adapted from Reference 64 and modified by author.) 65

4.7 Comparisons between predictions of heat flow $|Q|$ given respectively by the effective radius of Ueda et al. and Hsu & Biwa, for stacked-screen regenerators in pressurized argon gas with 0.45 MPa and oscillation frequency of 200 Hz. (Figure adapted from Reference 64 and modified by author.) 65

5.1 Schematic diagram of the experimental setups of the looped tube engine (top) and the straigh tube engine (bottom). 69

5.2 Comparisons of stability curves between experiments and calculations. 77

5.3 Comparisons of stability curves between experiments and calculations for the regular flow channel regenerator, reported by Ueda et al. [72]. 78

5.4 Comparisons of stability curves between experiments and calculations for the regular flow channel regenerator, reported by Guédra et al. [73]. 78

5.5 Growth of saturation pressure amplitude $|P|$ at $x = 0.935$ m of the loop tube engine as a function of the temperature difference ΔT. 80

5.6 Growth of saturation pressure amplitude $|P|$ at $x = 0.155$ m of the straight tube engine as a function of the temperature difference ΔT. 80

5.7 Thermal efficiency determined by experiments and calculation. 81

5.8 Comparisons of acoustic field distribution between experimentations and calculations for the Standing wave thermoacoustic engine. 82

A.1 Measured acoustic field with #100 mesh, 44 Hz, $\Delta T = 250$ K, and argon gas. In (a), the black curve represents the pressure amplitude $|P|$, whereas the blue curve represents the radial averaged velocity amplitude $|U|$. In (b), the black curve represents the magnitude $|Z|$, and the blue curve presents the phase $\arg[Z]$ 92

A.2 Experimental results of ΔW in the case of Ar. The velocity amplitude was kept at 0.02 m/s. Colors represent the temperature difference ΔT of the regenerator. (Figure adapted from Reference 94 and modified by author.) 94

A.3 Experimental results of ΔW in the case of He. The velocity amplitude was kept at 0.05 m/s. Colors represent the temperature difference ΔT of the regenerator. (Figure adapted from Reference 94 and modified by author.) 94

A.4 Experimental results of W_T in the case of Ar. Colors represent the temperature difference ΔT of the regenerator. W_T represents the contribution of the temperature difference to the acoustic power production ΔW. (Figure adapted from Reference 94 and modified by author.) 96

A.5 Experimental results of W_T in the case of He. Colors represent the temperature difference ΔT of the regenerator. W_T represents the contribution of the temperature difference to the acoustic power production ΔW. (Figure adapted from Reference 94 and modified by author.) 96

A.6 Experimental results of $1/R_\mathrm{P}$ tested with #30 regenerator. Panels (a) and (b) are plotted with identical measured data with respective horizontal axes of $|P_\mathrm{ave}|$ and $|V|$. 97

A.7 Experimental results of $1/R_\mathrm{P}$ tested with stacked-screen regenerator of #30 mesh. Symbols are measured data, and curves are predictions using empirical equations of Nusselt number respectively proposed by Swift & Ward, Tanaka et al., and Gedeon & Wood. 100

A.8 Experimental results of $1/R_\mathrm{P}$ tested with #100 regenerator. Symbols are measured data, and curves are empirical fitting. 101

List of tables

2.1 Geometrical properties of regenerators. 29

3.1 Maximum deviations between predictions and experiments of r_{eff} in the case of 44 Hz. 45

3.2 Maximum deviations between predictions and experiments of r_{eff} in cases of 20.0 and 100 Hz. 48

4.1 Geometrical properties of regenerators. 57

5.1 Geometrical properties of regenerators used in the thermoacoustic engines. . . 70

5.2 Experimental conditions for testing the thermoacoustic engines. 71

A.1 Coefficients of polynomial fit. 95

List of symbols

Roman Letters

A	area	[m^2]
a	adiabatic sound speed	[m/s]
A_r	gas-occupied area, $= \phi A$	[m^2]
b	function of volume porosity used in Equation (4.7) of Swift and Ward, $= 3.81 - 11.29\phi + 9.47\phi^2$	[−]
c	heat capacity per unit mass	[$\mathrm{J/(kg \cdot K)}$]
c_1	function of volume porosity used in Equation (2.7), $= -2.82+10.7\phi-8.6\phi^2$	[−]
c_2	function of volume porosity used in Equation (2.7), $= 1268 - 3545\phi + 2544\phi^2$	[−]
c_p	isobaric heat capacity per unit mass	[$\mathrm{J/(kg \cdot K)}$]
d	characteristic length of the flow channel	[m]
d_h	hydraulic diameter	[m]
d_w	wire diameter of metallic mesh screen	[m]
$e_{1,2,3}$	coefficients of polynomial fit, Table A.1	[−]
Ec	Eckert number, $= \dfrac{V_0^2}{c_{\mathrm{p},0}\Theta}$	[−]
F	matrix element	[−]
f	Moody friction factor, Equation (1.10)	[−]
$\mathbb{G}$	gain coefficient for thermoacoustic equation, Equations (3.11) and (A.5)	[m^{-1}]
g	coefficient of acoustically driven heat power of Q_A, Equations (4.3)	[−]
g_c	integration coefficient used in oscillation temperature of Equation (4.7) of Swift and Ward	[−]

g_{v}	integration coefficient used in oscillation temperature of Equation (4.7) of Swift and Ward	[–]
g_{D}	coefficient of acoustically driven heat power of Q_{D}, Equations (4.3)	[–]
G_{S}	coefficient used in oscillation temperature of Equation (4.7) of Swift and Ward	[–]
Y_{S}	coefficient used in oscillation temperature of Equation (4.7) of Swift and Ward	[–]
h	convective heat transfer coefficient	$[\mathrm{W/(m^2 \cdot K)}]$
$\mathbf{i}$	unit position vector along i direction in the Cartesian coordinate system	[m]
J_n	Bessel function of the first kind with order n	[–]
$\mathbf{j}$	unit position vector along j direction in the Cartesian coordinate system	[m]
`ksFrac`	reduction factor of solid heat conduction of the regenerator made of stacked metallic mesh screens	[–]
k	thermal conductivity	$[\mathrm{W/(m \cdot K)}]$
$\mathbf{k}$	unit position vector along k direction in the Cartesian coordinate system	[m]
L	length of whole thermoacoustic engine system	[m]
l	length of regenerator	[m]
M	matrix	
N	number of cylindrical tubes	[–]
Nu	Nusselt number, $= \dfrac{hd}{k}$	[–]
$\mathcal{P}$	pressure, $= P_{\mathrm{m}} + p$	[Pa]
$\mathfrak{p}$	lattice pitch of the wire screen of square mesh	[m]
P	complex pressure amplitude of oscillation	[Pa]
p	oscillation pressure, $p(x,t) = \mathrm{Re}\Big[P(x) \cdot \exp(i\omega t)\Big]$	[Pa]
P_{m}	time-averaged pressure	[Pa]
Q	heat power (heat flow), Equations (1.8) and (4.3)	[W]
Q_{A}	compression-driven heat power, Equations (1.8) and (4.3)	[W]
Q_{D}	advection-driven heat power, Equations (1.8) and (4.3)	[W]
$\dfrac{1}{R_{\mathrm{P}}}$	thermal-relaxation resistance, Equations (A.4) and (A.10)	$[\mathrm{m^2/(Pa \cdot s)}]$

R	flow resistance, Equation (2.6)	$[\mathrm{Pa \cdot s/m^4}]$
r	flow channel radius or radial coordinate	[m]
r_0	effective radius of Ueda et al.	[m]
R_ν	viscous resistance, Equation (2.4)	$[\mathrm{Pa \cdot s/m^4}]$
r_d	half spacing of parallel plates	[m]
r_eff	effective radius of Hsu and Biwa	[m]
Re	Reynolds number, $= \dfrac{V_0 d}{\nu}$	[−]
Re_ω	kinetic Reynolds number, $= \dfrac{\omega d_\mathrm{h}^2}{\nu}$	[−]
Re_h	Reynolds number characterized by the hydraulic diameter d_h, $= \dfrac{\lvert V\rvert d_\mathrm{h}}{\nu}$	[−]
s	complex amplitude of entropy oscillation, Equations (4.2) and (4.10)	[J/K]
$\mathcal{T}$	temperature, $= T_\mathrm{m}$ + oscillation temperature	[K]
t	short time interval	[s]
$\mathscr{T}$	complex amplitudes of temperature oscillations, $= \mathscr{T}(r, x)$	[K]
T	radial-averaged complex temperature amplitude of oscillation	[K]
t	time	[s]
T_m	time-averaged temperature	[K]
$\mathcal{U}$	complex amplitudes of velocity oscillations, $= \mathcal{U}(r, x)$	[m/s]
U	radial-averaged complex velocity amplitude of oscillation	[m/s]
u	radial-averaged oscillation velocity, $u(x,t) = \mathrm{Re}\Big[U(x) \cdot \exp(i\omega t)\Big]$	[m/s]
V	(spatial mean) complex velocity amplitude of oscillation in regenerator region	[m/s]
V_0	representative velocity of flow	[m/s]
$\mathbf{v}$	velocity vector	[m/s]
W	acoustic power (work flow), Equations (1.7) and (2.1)	[W]
W_ν	viscous power dissipation, Equation (A.7)	[W]
W_P	thermal-relaxation power dissipation, Equation (A.8)	[W]

W_T	thermoacoustic power production, Equation (A.9)	[W]
x	coordinate along sound-propagation direction	[m]
x	position vector	[m]
$\mathbb{Y}$	admittance coefficient for thermoacoustic equation, Equation (3.10)	$[\mathrm{m}^2/(\mathrm{Pa}\cdot\mathrm{s})]$
$\mathbb{Z}$	impedance coefficient for thermoacoustic equation, Equation (3.9)	$[\mathrm{Pa}\cdot\mathrm{s}/\mathrm{m}^4]$
Z	specific acoustic impedance	$[\mathrm{Pa}\cdot\mathrm{s}/\mathrm{m}]$
z	integral variable in the temperature Equation (4.7) of Swift and Ward	[−]
Z_a	impedance of acoustical system	$[\mathrm{Pa}\cdot\mathrm{s}/\mathrm{m}^3]$
Z_me	impedance of mechanical system	$[\mathrm{Pa}\cdot\mathrm{s}/\mathrm{m}^3]$

Greek Letters

α	thermal diffusivity	$[\mathrm{m}^2/\mathrm{s}]$
β	thermal expansion coefficient	$[\mathrm{K}^{-1}]$
$\chi_\sharp$	thermoacoustic functions, the subscript of $\sharp = \nu$ and α respectively for the viscous and thermal effects, Equations (1.4) and (5.5) for circular cylindrical tubes, Equations (3.16) and (5.7) for parallel plates	[−]
$\delta_\sharp$	penetration depth, the subscript of $\sharp = \nu$ and α respectively for the viscous and thermal effects, Equations (1.3)	[−]
Δ	difference	[−]
η	thermal efficiency, Equation (5.3)	[−]
ε	error for determining the experimental effective radius, Equations (3.19) and (3.20)	[%]
ε_h	coefficient used in oscillation temperature of Equation (4.7) of Swift and Ward	[−]
ε_s	coefficient used in oscillation temperature of Equation (4.7) of Swift and Ward	[−]
γ	ratio of isobaric to isochoric specific heats	[−]
i	unit imaginary number $\sqrt{-1}$	[−]
λ	coefficient used in transfer matrix characterized by thermoacoustic equations, $= \dfrac{\tau\Delta x}{2}$	[−]
μ	dynamic viscosity	$[\mathrm{kg}/(\mathrm{m}\cdot\mathrm{s})]$
ν	kinematic viscosity	$[\mathrm{m}^2/\mathrm{s}]$

Φ	rate of work being down by the stresses in distorting the fluid	[W]
ϕ	volume porosity	[−]
π	ratio of a circle's circumference to its diameter, $\simeq 3.14\ ...$	[−]
ρ	density	[kg/m^3]
σ	Prandtl number	[−]
ξ	oscillation displacement amplitude of gas	[m]
ξ_0	non-dimensional oscillation displacement of gas, $= \dfrac{\xi}{d_\mathrm{h}}$	[−]
τ	coefficient used in transfer matrix characterized by thermoacoustic equations, $= \sqrt{\mathbb{G}^2 + 4\mathbb{Y}\mathbb{Z}}$	[m^{-1}]
Θ	representative temperature difference	[K]
θ	phase lead of P relative to U	[rad]
θ_P	phase lead of U relative to P, used in Equation (4.7) of Swift and Ward	[rad]
θ_T	phase lead of U relative to T, used in Equation (4.7) of Swift and Ward	[rad]
ω	oscillation angular frequency	[s^{-1}]

Superscripts

$*$	dimensionless form for a physical quantity

Subscripts

0	reference or representative
α	thermal
All	thermoacoustic engine
ave	spatial mean value in regenerator region
cal	calculation
†	-th segment of matrix
Emp.	empirical fitting
exp	experimental
G	Gedeon and Wood
HE	heat exchanger

H	hot end
i	along i direction in the Cartesian coordinate system
in	physical quantity entering the engine
j	along j direction in the Cartesian coordinate system
k	along k direction in the Cartesian coordinate system
L	the end of axial coordinate x of whole thermoacoustic engine system
m	mean
$\natural$	inlet-side ($\natural = 1$) and outlet-side ($\natural = 2$) of regenerator (unit)
ν	viscous
Nu	Nusselt number
OFF	absence of acoustic oscillations
ON	presence of acoustic oscillations
out	physical quantity going out of the engine
O	Obayashi et al.
o	origin of axial coordinate x of whole thermoacoustic engine system
tube	waveguide tube
REG	regenerator
R	ambient end
S	Swift and Ward
s	solid
TBT	thermal buffer tube
T	Tanaka et al.
$\vee, \wedge$	row ($\vee$) and column ($\wedge$) for matrix elements

Operators

$\lvert\cdots\rvert$	taking the absolute value of a number
$\arg[\cdots]$	taking the argument of a complex number
$\langle\cdots\rangle$	taking the cross-sectional average

$\exp(\cdots)$	taking the exponential function for a number
$\int \cdots dA$	surface integration over the cross-sectional area of the flow channel A
$\mathrm{Im}[\cdots]$	taking the imaginary part of a complex number
∇	nabla operator, $= \mathbf{i}\frac{\partial}{\partial x_i} + \mathbf{j}\frac{\partial}{\partial x_j} + \mathbf{k}\frac{\partial}{\partial x_k}$
$\mathrm{Re}[\cdots]$	taking the real part of a complex number
$\widetilde{\cdots}$	taking the conjugate of a complex number

Others

$\dot{\cdots}$	changing with Nusselt number
$\grave{\cdots}$	for heat exchangers with uniform temperature
#	number of mesh screen
%	percent

Chapter 1

Introduction

1.1 Thermoacoustic oscillations and thermoacoustic heat engines

1.1.1 History of thermoacoustic oscillations

The earliest observation of thermoacoustic oscillations, being thermally induced acoustic oscillations of a gas column, probably was made in the Far East, the ancient Japan on the 16th century. The « *Ugetsu Monokatari* » (雨月物語, Tales of moonlight and rain), published in 1776 [1], for the first time, describes the thermoacoustic oscillations by an instrument called "kibitsunokama" (吉備津の釜, Kettle of Kibitsu) for divining the future. The kettle of Kibitsu is illustrated in Figure 1.1 (a), which consists of a long iron bowl partially filled with water and a mesh screen basket loaded with rice grains. When the bowl is put on a fire, the downside of the mesh screen basket is heated by water vapor which passes through narrow flow channels shaped by rice grains. If an ox-bellowing sound is emitted from the kettle of Kibitsu, it means a good omen and that man's wish will come true. In the West of the 19th century, glassblowers occasionally found a phenomenon that a glass vessel radiated pure tones when a cold glass tube was blown on a small hot glass bulb, i.e, a temperature gradient was imposed on the flow channel. This phenomenon was first described in Europe by the German physicist Karl Sondhauss in 1850 [2]. The tube with a heating bulb which generates sound was thus named as the Sondhauss tube, as Figure 1.1 (b). A similar structure of "Rijke tube" [3], an open-end tube having a metallic wire screen inside of it as Figure 1.1 (c), was also discovered in the same period of 1859 by a Dutch physicist Pieter Rijke. By heating the wire screen by flame and removing it from the tube, the Rijke tube spontaneously generates sound waves until the wire mesh cooled down.

The first qualitative description of the thermoacoustic oscillations was given by Lord Rayleigh and noted in his famous textbook « *The theory of sound* » published in 1887 [4]. It is now known as the Rayleigh criterion:

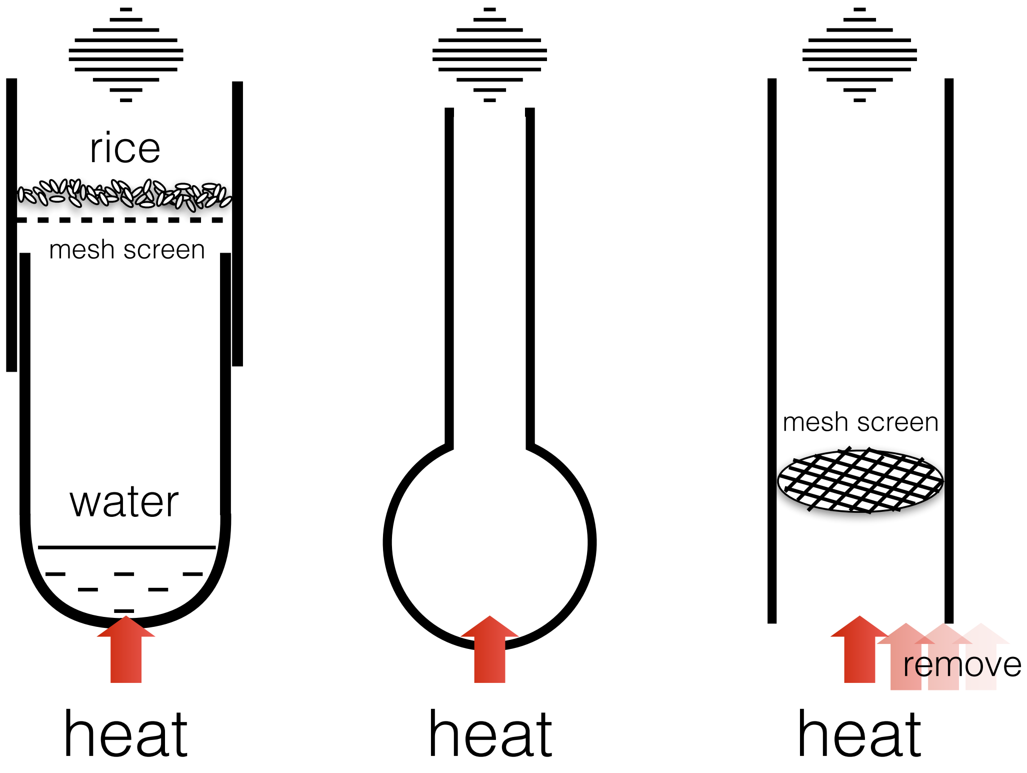

(a) Kettle of Kibitsu. (b) Sondhauss tube. (c) Rijke tube.

Figure 1.1: Examples of thermoacoustic oscillation systems.

> *“If heat be given to the air at the moment of greatest condensation or taken from it at the moment of greatest rarefaction, the vibration is encouraged.”*
>
> — Lord Rayleigh

Although Lord Rayleigh essentially pointed out the importance of the phasing between pressure oscillation and unsteady heat release for realizing the thermoacoustic oscillations, a satisfactory theoretical explanation was not given until 1960 by the efforts of Nikolaus Rott [5–10]. He assumed a small-amplitude longitudinal oscillations of a gas column with a long wavelength, and applied linearized basic equations of hydrodynamics to a gas confined in a tube with a step-function like temperature distribution, in order to study Taconis oscillation occurring in a tube inserted in a liquid Helium vessel [11]. His linear stability analysis predicted the critical temperature ratio between the hot and cold parts of the tube, which was verified by a systematic experiments. This result confirms the validity of Rott’s assumptions to describe thermoacoustic oscillations.

1.1.2 Theoretical studies on thermoacoustic oscillations

After the Rott's successful explanations on the basic mechanism of thermoacoustic oscillations, the thermoacoustic theory was individually proposed by Swift [12] and Tominaga [13, 14] by highlighting thermodynamic aspects of the Rott's theory. Rott assumed a long wavelength much larger than thermal and viscous penetration depths, ideal gas, steady-state sinusoidal oscillations with a single angular frequency ω, and a small oscillation amplitude for neglecting the higher order terms. All the acoustic variables are expressed as a sum of the temporal mean value and the fluctuating part. Also, a complex amplitude was used. So, for example, the pressure $\mathcal{P}\,(x,t)$ is written as $\mathcal{P} = P_{\mathrm{m}} + \mathrm{Re}\Big[P\,(x)\cdot\exp\,(i\omega t)\Big]$, where P_{m} denotes the time-averaged pressure, and the complex amplitude P stands for the pressure amplitude by its magnitude $|P\,(x)|$ and the initial phase by its argument $\arg\,[P\,(x)]$. With these assumptions, the thermoacoustic theory describes the momentum equation and the general equation of heat transfer for the fluid oscillating along a central axis of a regular flow channel as

$$U = \frac{i}{\omega\rho_{\mathrm{m}}}\frac{dP}{dx}\left(1-\chi_{\nu}\right), \tag{1.1}$$

$$T = \frac{1}{\rho_{\mathrm{m}}c_{\mathrm{p}}}\left(1-\chi_{\alpha}\right)P - \frac{1}{i\omega}\frac{dT_{\mathrm{m}}}{dx}\frac{\left(1-\chi_{\alpha}\right)-\sigma\left(1-\chi_{\nu}\right)}{\left(1-\chi_{\nu}\right)\left(1-\sigma\right)}U, \tag{1.2}$$

where U and T, ρ_{m} and T_{m}, and c_{p} and σ respectively stand for radial-averaged oscillation complex amplitudes of velocity and temperature, the time-averaged density and temperature of the working gas, and the isobaric heat capacity per unit mass and Prandtl number. In the equations above, $\chi_{\sharp}$ ($\sharp = \alpha$ or ν) are called thermoacoustic functions and described using the dimensionless parameters

$$\frac{r}{\delta_{\sharp}}, \tag{1.3}$$

where r is a tube radius, and δ_{α} and δ_{ν} are respectively the thermal penetration depth and viscous penetration depth ($\delta_{\alpha} = \sqrt{2\alpha/\omega}$ and $\delta_{\nu} = \sqrt{2\nu/\omega}$, where α is the thermal diffusivity, and ν is the kinematic viscosity). The thermoacoustic function $\chi_{\sharp}$ is shown in Figure 1.2 as a function of $r/\delta_{\sharp}$. The explicit functional form of $\chi_{\sharp}$ for a cylindrical tube with radius r is expressed as

$$\chi_{\sharp} = \frac{2J_1\left[(i-1)\,\frac{r}{\delta_{\sharp}}\right]}{(i-1)\,\frac{r}{\delta_{\sharp}}J_0\left[(i-1)\,\frac{r}{\delta_{\sharp}}\right]}, \tag{1.4}$$

where J_0 is the zero-th order Bessel function of the first kind, and J_0 is the first order Bessel function of the first kind. Equation (1.2) is substituted in the linearized continuity equation

$$i\omega\rho_{\mathrm{m}}\left(\frac{P}{P_{\mathrm{m}}}-\frac{T}{T_{\mathrm{m}}}\right)+\frac{d}{dx}\left(\rho_{\mathrm{m}}U\right)=0 \tag{1.5}$$

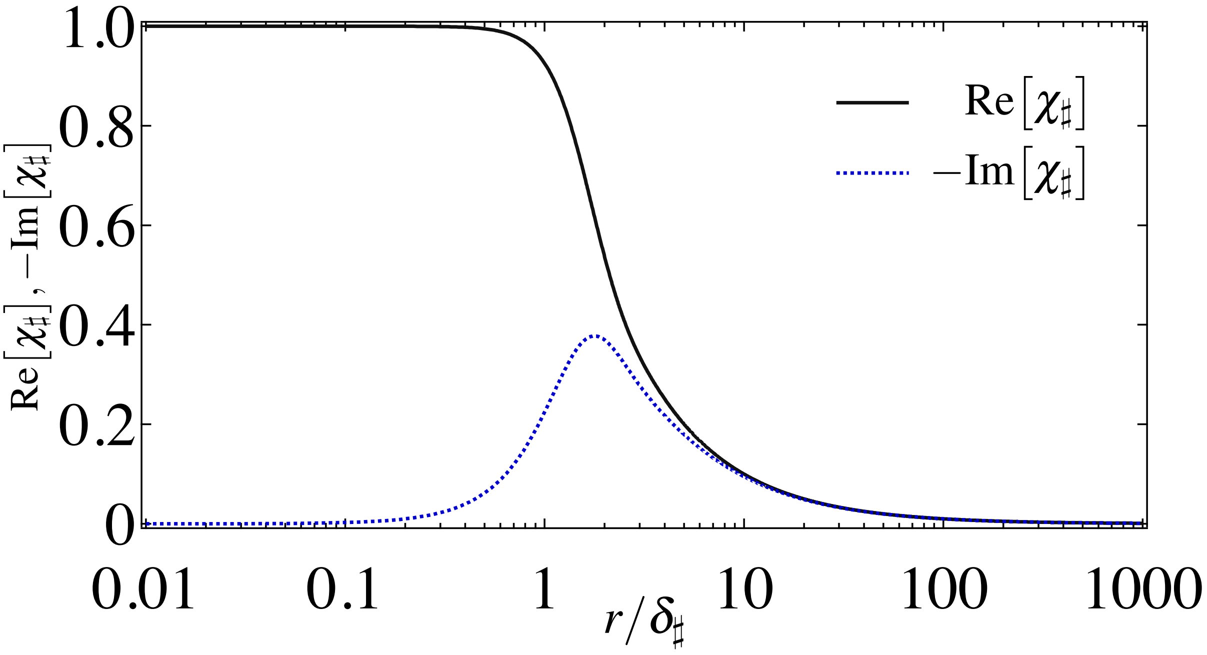

Figure 1.2: Thermoacoustic function versus $r/\delta_\sharp$.

to derive the thermoacoustic continuity equation shown below

$$\frac{dU}{dx} = -i\omega\frac{\left[1+(\gamma-1)\,\chi_\alpha\right]}{\gamma P_\mathrm{m}}P + \frac{\chi_\alpha-\chi_\nu}{(1-\chi_\nu)\,(1-\sigma)}\frac{1}{T_\mathrm{m}}\frac{dT_\mathrm{m}}{dx}U, \tag{1.6}$$

where γ is the ratio of isobaric to isochonic specific heats. Equations (1.1) and (1.6) constitute coupled differential equations of complex amplitudes P and U with respect to x, which can be solved once the boundary conditions are given. By using P and U, other acoustic variables like T can be also determined from Equation (1.2) and thermodynamic relations.

Swift and Tominaga used Equations (1.1) and (1.6) to discuss the mutual energy conversion between the work flow (the acoustic power) W and the heat flow (the heat power) Q. The mutual energy conversion is the central physical concept of the thermoacoustic theory. The work flow W is expressed as

$$W = \frac{1}{2}A\mathrm{Re}\left[P\widetilde{U}\right], \tag{1.7}$$

and the heat flow Q is expressed as

$$Q = \frac{1}{2}\rho_\mathrm{m}T_\mathrm{m}\int \mathrm{Re}\left[s\widetilde{\mathcal{U}}\right]dA, \tag{1.8}$$

where s and $\mathcal{U}$ are respectively complex amplitudes of the entropy and velocity oscillations, A signifies the cross-sectional area of the flow channel, and the tilde $\widetilde{\cdots}$ denotes the operation of the complex conjugate. Also, the surface integration $\int\cdots dA$ is done over the cross-sectional area of the flow channel. In Equation (1.8), it should be noticed that s and $\mathcal{U}$ are functions of r and x with $s = s(r,x)$ and $\mathcal{U} = \mathcal{U}(r,x)$, and their cross-sectional-averaged values are expressed with $\langle s(r,x)\rangle = \langle s\rangle(x)$ and $\langle \mathcal{U}(r,x)\rangle = U(x)$, where $\langle\cdots\rangle$ means taking the cross-sectional average.

As can be seen from Equations (1.7) and (1.8), both W and Q are energy flows in axial direction and maintained by oscillatory motion of the gas. The sum of W and Q is the oscillation-induced enthalpy flow H (= $\frac{1}{2}c_{\mathrm{p}}\rho_{\mathrm{m}}\int \mathrm{Re}\left[\mathcal{T}\widetilde{\mathcal{U}}\right]dA$ for an ideal gas, where $\mathcal{T} = \mathcal{T}(r, x)$ is the complex temperature amplitude) [14].

The energy conservation law is expressed as $\nabla(W + Q) = 0$, which assures the mutual conversion between W and Q. The integral form of the energy conservation law is expressed as:

$$\Delta W = Q_{\mathrm{in}} - Q_{\mathrm{out}}, \tag{1.9}$$

where Δ denotes the axial difference and subscripts of in and out respectively signify a certain physical quantity entering and going out of the engine. When the energy conversion from Q to W takes place, a positive ΔW is obtained. Therefore, ΔW can be seen as the output power resulting from the thermoacoustic energy conversion. In other words, thermoacoustic engines are the heat engines that generates acoustic output power ΔW instead of mechanical power in conventional heat engines. The energy flows W and Q serve as a link between acoustic waves discussed in hydrodynamics and heat engines in thermodynamics.

The thermoacoustic theory has presented that the thermal interaction between the gas and the channel walls is essential to the thermoacoustic energy conversion between W and Q. For air at ambient temperature and pressure, δ_α is about 0.2 mm when the oscillation frequency is 100 Hz. So in the flow channels with 10 mm radius, more than 99 % of the gas adiabatically oscillates, because the gas very close to the wall within the distance of δ_α undergoes the thermal contacts with the wall. In order to enhance the thermal interaction between the gas and the wall, porous materials called a stack or a regenerator is used in thermoacoustic engines. The stack possesses the flow channels of the size $r/\delta_\alpha \approx 1$. The heat exchange process between the gas and the channel wall takes place but with the time delay because of the imperfect thermal contact. The regenerator is characterized by the condition $r/\delta_\alpha \ll 1$. The isothermal heat exchange process is achieved, so the gas oscillates in the channel equilibrating with the wall.

Figures 1.3 and 1.4 illustrate the axial distribution of energy flows in a flow channel with a positive temperature gradient. In both cases, Q decreases as it flows down, while W increases its flow rate. As already explained, the positive ΔW represents the output power. In Figure 1.3, W is amplified as it goes up the temperature gradient imposed on the regenerator. When this type of energy flow pattern is achieved, the engine is called a traveling wave engine. In Figure 1.4, W is emitted from the stack and flows out of both sides. The engines showing this type of energy flow pattern is called a standing wave engine. In the next section, a brief explanation of both types of thermoacoustic engines is given in terms of r/δ_α.

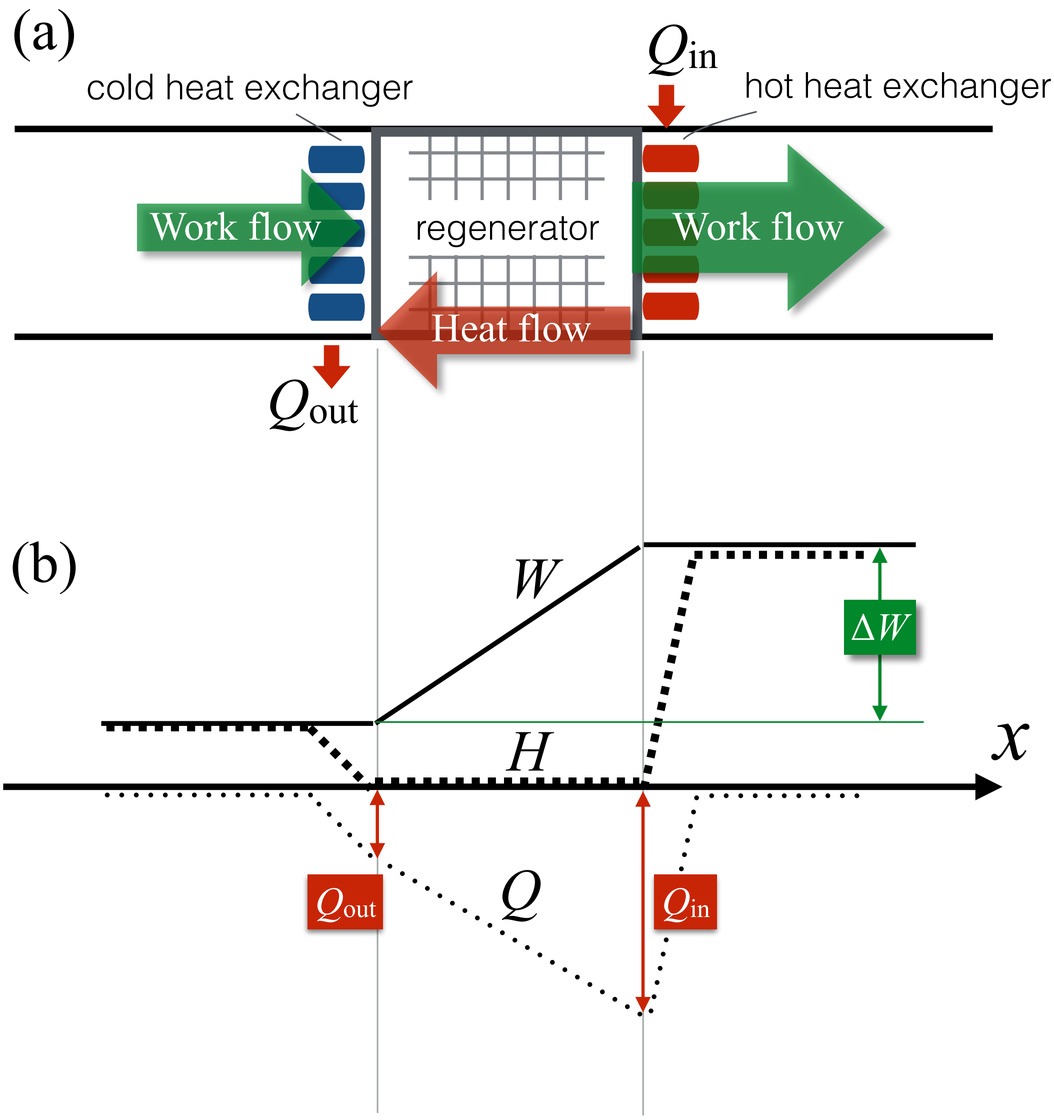
(a)
cold heat exchanger
Q_{in}
hot heat exchanger
Work flow
regenerator
Work flow
Heat flow
Q_{out}
(b)
W
ΔW
H
x
Q_{out}
Q
Q_{in}

Figure 1.3: Energy flow distributions in the traveling wave engine.

1.1.3 Types of thermoacoustic engines

The standing wave engine, developed by a research group of Los Alamos National Laboratory [15, 16], pioneered the modern thermoacoustic technology. An example of the standing wave engine is shown in Figure 1.6. The acoustic standing wave occurs owing to interference between forward and backward traveling waves reflecting at ends. The Sondhauss tube and the Rijke tube fall into this category. In contrast to those thermoacoustic systems in the early days, a porous media named as "stack" having numerous regular small cylindrical flow channels is installed in the cylindrical tube for enhancing the thermoacoustic conversion. A ceramic honeycomb catalyst shown in Figure 1.5 is often used as the stack. The dimensionless parameter r/δ_α is approximately unity in the stack. Thus the thermal contact between the gas and the stack wall is rather irreversible. The thermoacoustic energy conversion is achieved by gas parcels having the standing wave phasing meaning that the pressure and velocity oscillate out of phase by 90°, as

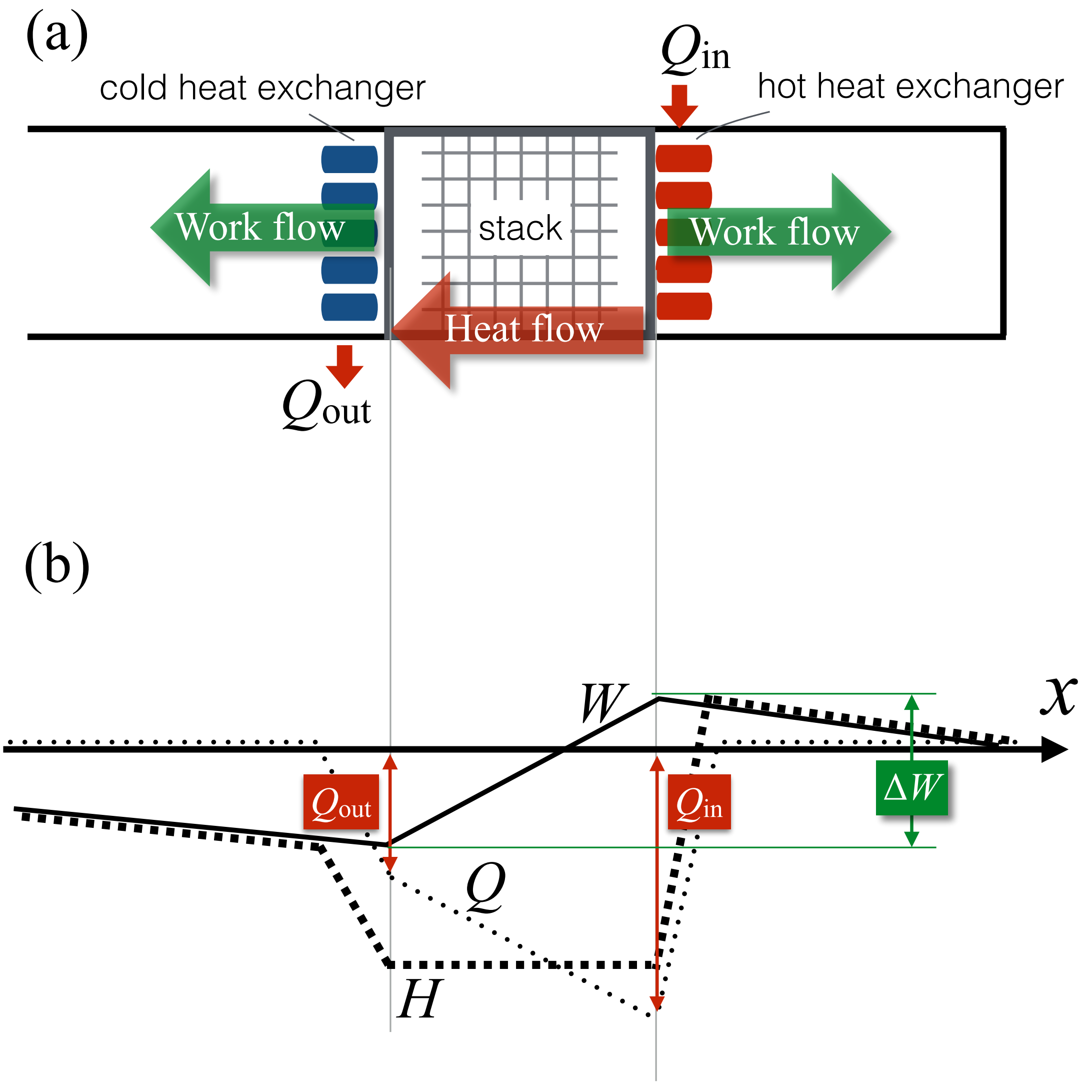

Figure 1.4: Energy flow distributions in the standing wave engine.

in a standing acoustic wave in a lossless resonator. With this phasing, the gas parcel can satisfy the Rayleigh criterion when $r/\delta_\alpha \approx 1$. Thus the thermal efficiency of the standing wave engine is not so high because an intrinsically irreversible thermal contact in the stack.

The standing wave thermoacoustic engine was used to build "a beer cooler" reported in Reference 16, which is illustrated in Figure 1.7. The beer cooler consists of a 37-cm-long tube closed at the top and open to a large spherical bulb at the bottom, and is filled with 0.3 MPa helium gas. A pair of stack of plates are placed with heat exchangers. One of the stack on the top functions as a prime mover producing acoustic power from heat. When the temperature of the hot heat exchanger goes beyond the onset temperature, the helium gas starts to oscillate spontaneously at about 580 Hz and produces intense oscillations with a pressure antinode at the closed top and a velocity antinode at the tube-bulb junction. Another stack placed below the prime-mover stack functions as a heat pump driven by the acoustic power emitted from the

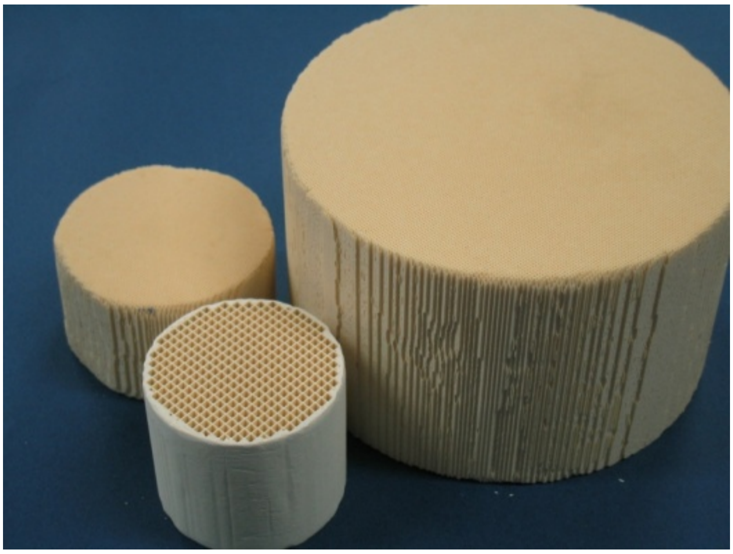

Figure 1.5: Ceramic honeycomb catalysts, made of regular square pores.

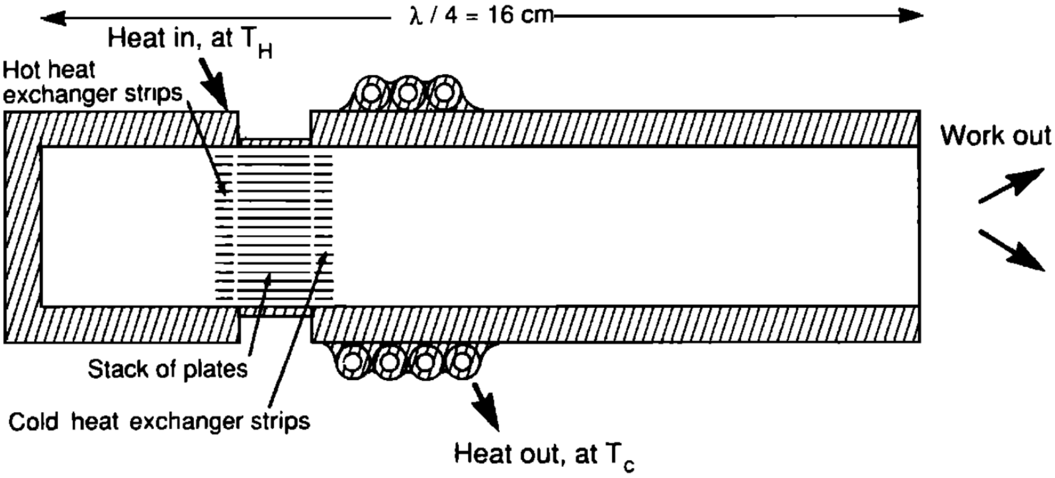

Figure 1.6: The standing wave thermoacoustic engine (reproduced from Reference 16).

prime-mover stack. When the hot heat-exchanger temperature is high enough, oscillating gas of the heat pump stack cools the cold heat exchanger to below 0° C. Therefore, the whole system operates as a refrigerator without any moving parts, energetically sourced by input heat power.

The idea of traveling wave thermoacoustic engine was first proposed by Peter Ceperly in 1979 [17], who recognized that the the Rayleigh criterion is satisfied without introducing the imperfect thermal contact if the pressure and velocity oscillations are temporarily in phase. This phasing is called a traveling wave phasing in accordance with the phase relation between pressure and velocity in a freely traveling acoustic wave. The gas thermodynamic cycle consisting of periodic expansion/compression and heating/cooling processes becomes identical to Stirling thermodynamic cycle. Therefore, the traveling wave engine is often called a thermoacoustic Stirling engine. Differently from the stack, r/δ_α of the regenerator is much smaller than 1, which enables an excellent thermal contact and reversible heat transfer processes during periodic motions of the gas parcel. Therefore, the thermal efficiency of the traveling wave engine essentially achieves the Carnot efficiency.

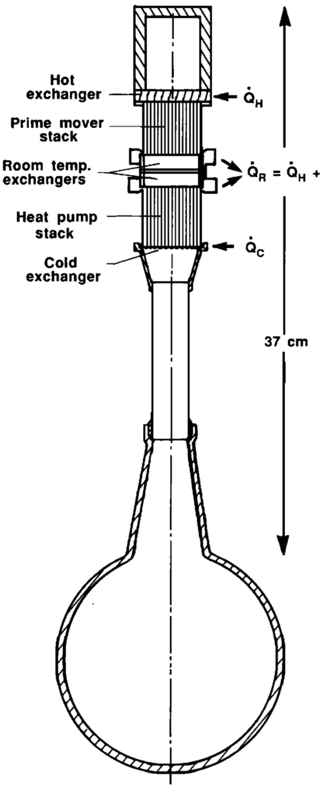

Figure 1.7: The standing wave thermoacoustic refrigerator applied as a beer cooler (reproduced from Reference 16).

The traveling wave thermoacoustic engine was not developed until the first experimental observation in 1998 [18], reported by Japanese physicist Taichi Yazaki and his colleagues. A looped tube for sound wave feedback was used to realize the traveling wave phasing at the regenerator in the engine of Yazaki et al., which is shown in Figure 1.8 (a). In their looped tube engine, a large velocity amplitude induced significant viscous loss in the regenerator region. In the next year of Yazaki's report, a different configuration of the traveling wave engine achieving higher thermal efficiency was proposed by Backhaus and Swift of Los Alamos laboratory [19], as shown in Figure 1.8 (b). The engine was made of a looped tube and a straight resonance tube, and filled with pressurized helium gas at 3 MPa. Owing to this configuration, a high specific acoustic impedance $\approx 30\rho_{\mathrm{m}}a$ was achieved at the position of the regenerator, which suppressed the velocity amplitude in the regenerator region. In a feely traveling wave, the acoustic impedance, the ratio of pressure amplitude to velocity amplitude, is equal to the intrinsic acoustic impedance of the gas, given by $\rho_{\mathrm{m}}a$, where ρ_{m} is the mean density of the gas and a is the sound speed. If a traveling wave passes through tiny pores in the regenerators, the viscous losses would become significant. As a result of the elevated acoustic impedance, their traveling wave engine achieved a high thermal efficiency of 30 % comparable to commercial internal combustion engines.

Although the traveling wave engine designed by Backhaus and Swift have obtained a high thermal efficiency, a high operating temperature of 725° C was far from commercial interest of applications like a waste-heat utilization. Recent developments of the traveling wave engine was intended for utilizing low temperature difference heat sources from solar vacuum tube collectors

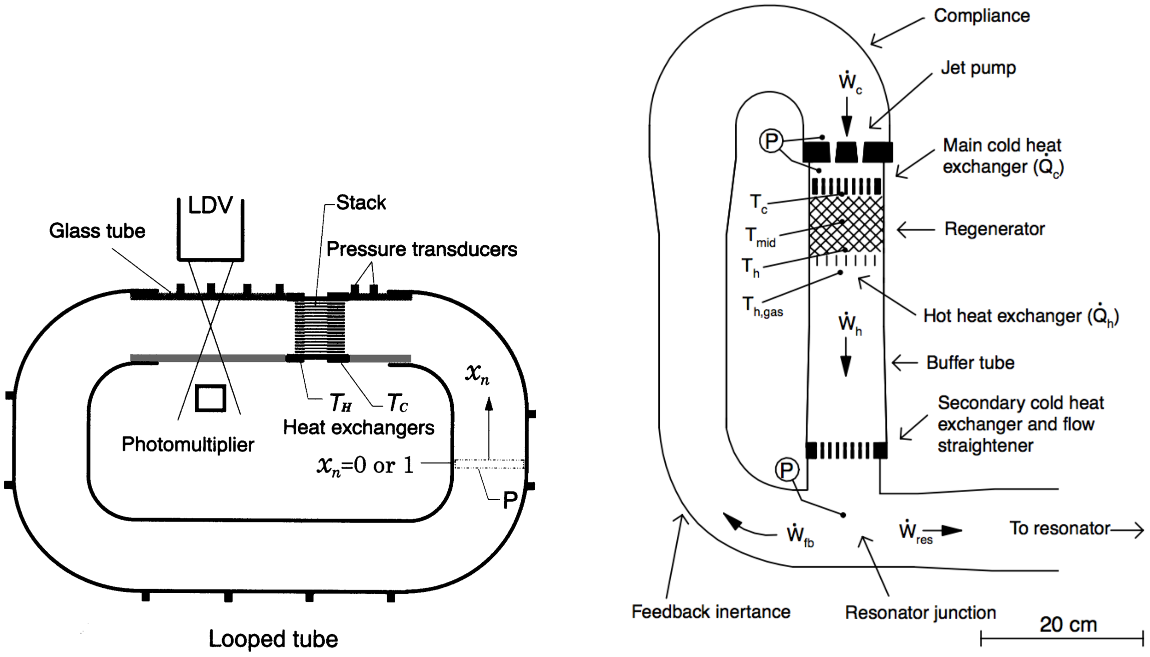
LDV
Glass tube
Stack
Pressure transducers
x_n
T_H
T_C
Heat exchangers
Photomultiplier
x_n=0 or 1
P
Looped tube
Compliance
Jet pump
$\dot{W}_c$
P
Main cold heat exchanger ($\dot{Q}_c$)
T_c
T_{mid}
T_h
$T_{h,gas}$
Regenerator
Hot heat exchanger ($\dot{Q}_h$)
$\dot{W}_h$
Buffer tube
Secondary cold heat exchanger and flow straightener
P
$\dot{W}_{fb}$
$\dot{W}_{res}$
To resonator
Feedback inertance
Resonator junction
20 cm

(a) Traveling wave engine, reported by Yazaki et al., cited from Reference 18.

(b) Traveling wave engine, proposed by Backhauss and Swift, cited from Reference 19.

Figure 1.8: Traveling wave thermoacoustic engine

or waste heat in the range from 70 to 200° C [20–22]. de Blok has developed and tested a 4-stage traveling wave engine, as illustrated in Figure 1.9 [21]. This engine is filled with helium gas at a mean pressure of 750 kPa. All components per stage consisting of a regenerator and tubes sections are identical. Use of multiple regenerators in a thermoacoustic system allows to reduce the onset temperature of the engine [23, 24], while viscous losses due to velocity amplitude is reduced by enlarged regenerator cross-sectional area in this engine. Furthermore, four identical regenerator units are placed on a mutual distance of 1/4 wavelength, which enables sound reflections less. In this way, the traveling wave phase is kept in the location of the regenerator for the energy conversion. This thermoacoustic system have been applied for converting industrial waste heat into electricity in the framework of a Dutch SBIR program[1], and operated as a cooking device for developing countries which generates 50 W electricity beside hot water.

Unlike the mechanical Stirling-cycle engines, the thermoacoustic Stirling engine converts heat power to acoustic power with using sound waves in place of mechanical pistons. Delivering the output power by acoustic waves avoids problems caused by moving parts such as piston sealing and friction losses from mechanical cranks and rockers. The thermoacoustic engine is consequently admitted as a highly reliable and low cost engine. Furthermore, the thermoacoustic engines are free from Freon gases that can lead to environmental problems. Therefore, the further development is highly anticipated for the thermoacosutic Stirling engines.

---

[1] The Small-Business Innovation Research (SBIR) programme is a Dutch government subsidy for businesses proposing innovative solutions to social issues. The detail can be fined in: http://startup.ondernemersplein.nl/growth-and-development/innovation-incentive-schemes/small-business-innovation-research-sbir-programme/.

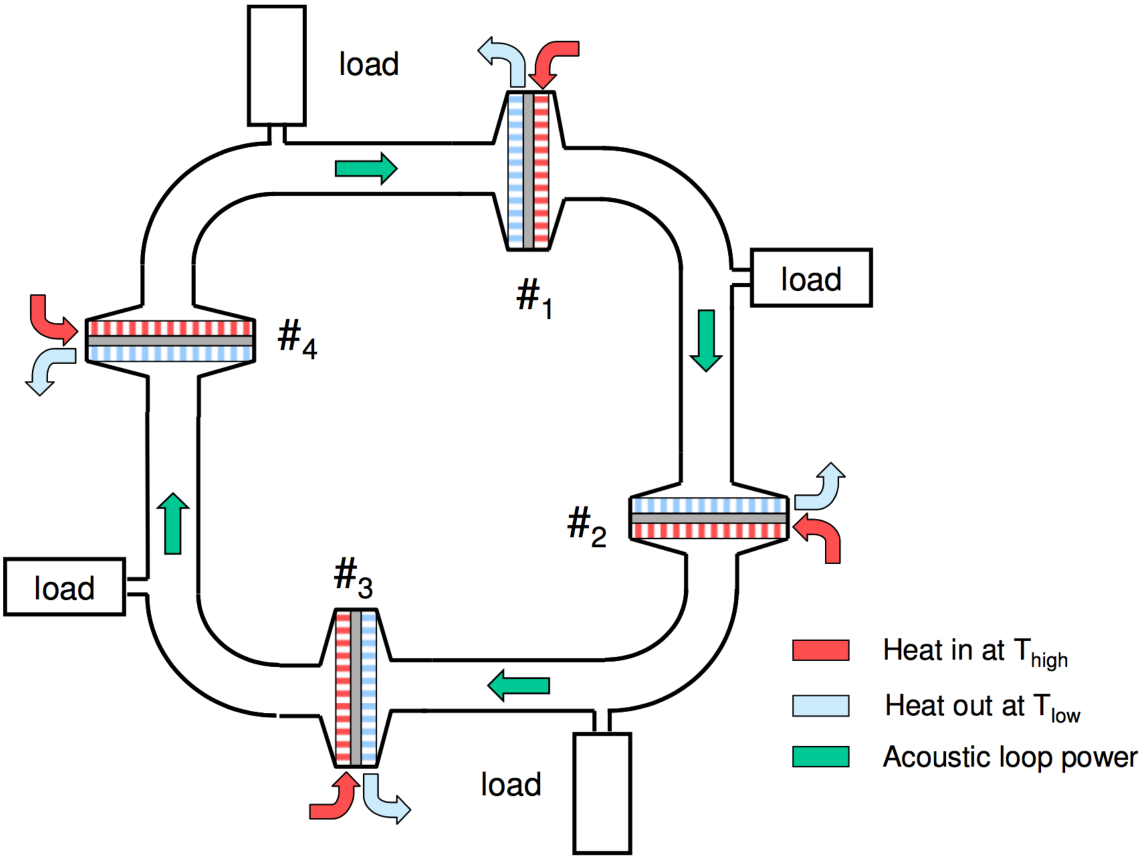

Figure 1.9: The 4-stage traveling wave thermoacoustic engine proposed by de Blok, cited from Reference 21.

1.2 Stacked-screen regenerator

1.2.1 Required flow properties

The regenerator, having numerous flow channels, is a key component for the thermoacoustic Stirling engine to achieve a high thermal efficiency. A *stacked-screen regenerator* having tortuous flow channels as Figure 1.10 (a) is mostly used in practical thermoacoustic Stirling engines, because the regenerator made of a pile of metallic woven mesh screens of Figure 1.10 (b) achieves high surface-area-to-volume ratio and an excellent thermal contact. However, complex flow geometry of flow passages is an obstacle for theoretical understanding of regenerator's fundamental characteristics. Therefore, a lot of efforts has been made to characterize the stacked-screen regenerators, as described below.

1.2.2 Literature review

From Stirling engine studies

Mechanical Stirling engine researchers have long devoted efforts to characterize the stacked screen regenerator. In early days (1957, 1964), the steady flow experimental investigations [25,

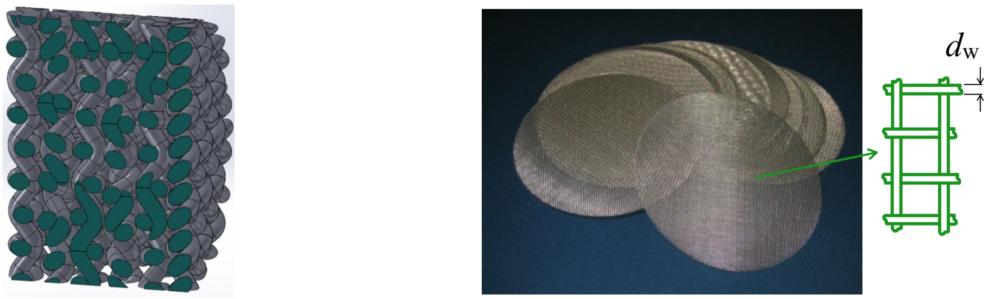

(a) Tortuous flow channels constructed by stacked mesh screens.

(b) Metallic woven mesh screens.

Figure 1.10: Stacked mesh screens used in regenerators.

26] conducted by Tong, Kays, and London quantified viscous effects and heat transfer rates of the regenerator with the friction factor f and the Nusselt number Nu: The former is defined as a non-dimensional pressure gradient derived from the phenomenological equation of Darcy-Weisbach [27]. It is expressed as[2] [27, 28]

$$f = \frac{\Delta\mathcal{P}\dfrac{d}{l}}{\frac{1}{2}\rho_{\mathrm{m}}V_0^2}, \tag{1.10}$$

where $\Delta\mathcal{P}$ signifies pressure difference, V_0 denotes the representative velocity of the steady flow, and d and l respectively stand for the representative transverse length of the flow channel and length of the regenerator. The latter is defined as the ratio of convective to conductive heat transfer rates across (normal to) the boundary between the fluid and solid with [28, 29]

$$Nu = \frac{hd}{k}, \tag{1.11}$$

where h and k respectively signify the convective heat transfer coefficient of the flow and thermal conductivity of the fluid. The steady flow data show that both empirical equations of f and Nu are governed by the Reynolds number $Re = V_0 d/\nu$. Later, f and Nu of the stacked-screen regenerators used in Stirling engines were evaluated in unidirectional steady flow also by Rice et al. [30] and Hamaguchi et al [31]. However, since the Stirling engines employ reciprocating flow, those empirical equations derived from steady flow experiments would not be able to predict the realistic performance of the regenerators in the Stirling engine.

The oscillatory flow based measurements were reported in 1990's. Tanaka et al. (1990) [32] experimented the stacked-screen regenerators of seven kinds of mesh numbers (#50 meshes were tested in three different wire diameters) from #15 to #200 in oscillatory flow driven by reciprocating pistons of maximum of 10 Hz with a fixed flow displacement. Similar to the early studies, the Reynolds number was the only parameter to summarize their experimental friction factor and the Nusselt number, where they used the hydraulic diameter as the characteristic length of the flow channel in the regenerator, and defined the Reynolds number in the oscillatory flow by

---

[2] Here, the friction factor f means the Moody (or Darcy) friction factor. Note that friction factor given by one-fourth of f is called "Fanning friction factor" [28], which is defined as the ratio between the local shear stress and the local flow kinetic energy with density. Throughout this thesis, the Moody friction factor is used.

$$Re_{\mathrm{h}} = \frac{|V|d_{\mathrm{h}}}{\nu}, \tag{1.12}$$

where $|V|$ and d_{h} respectively represent the amplitude of oscillation velocity of the oscillatory flow in the region of the regenerator and the hydraulic diameter, and the subscript h of Re_{h} signifies that the Reynolds number is defined by the hydraulic diameter d_{h}. It should be noted that the Reynolds number Re_{h} in the oscillatory flow is independent of time in periodically steady states. Based on their measurements, Tanaka et al. also suggested that the friction factor and the heat transfer coefficient of the oscillatory flow may be higher than those of the unidirectional flow.

Gedeon and Wood (1996) [33] measured pressure drop and heat transfer rate of stacked-screen regenerators of three mesh numbers of #80, #100, #200 in oscillatory flow with oscillation frequency up to 120 Hz. In contrast to Tanaka's suggestion, Gedeon and Wood found their oscillation flow data hardly differed from the steady flow data obtained by Kays and London, because of no significant frequency dependence in their experimental results. As a result, their empirical equations of the friction factor and the Nusselt number were also only correlated to the Reynolds number.

Issiki et al. (1997) [34] reported experimental results of the flow resistance and heat transfer of stacked-screen regenerators of #20, #42 and #80 meshes tested in the oscillatory flow the maximum frequency of 8.3 Hz. By comparing their data with published empirical equations, they observed that their friction factor data were between the prediction from the steady flow experiments of Hamaguchi et al. and that from the oscillatory flow experiments of Tanaka et al. In addition, significant inconsistencies of non-dimensional heat transfer rates were observed between their experiments and published empirical predictions obtained by steady flow data of Rice and the oscillatory flow data of Tanaka.

Zhao and Cheng (1996) performed experiments for investigating oscillatory pressure drop [35] (tested in mesh numbers of #100, #150 and #200 meshes with maximum 9 Hz) and heat transfer characteristics [36] (tested in mesh number of #200 with maximum 9 Hz) of the stacked screen regenerator. They noticed an importance of the angular frequency ω in the oscillatory flow. For isolating respective effects of the oscillation frequency and the flow displacement, they decomposed the Reynolds number Re_{h} into a product of a kinetic Reynolds number Re_{ω}($= \omega d_{\mathrm{h}}^2/\nu$) and a non-dimensional displacement ξ_0 ($= \xi/d_{\mathrm{h}}$, where ξ is the oscillation displacement amplitude) with $Re_{\mathrm{h}} = \xi_0 Re_{\omega}/2$ through $|V| = \xi\omega/2$.

Swift and Ward (1996) [37] proposed a set of equations of momentum, continuity, and energy with a simple harmonic analysis for thermoacoustic regenerator made of stacked mesh screens. by assuming that the steady flow conditions were instantly achieved during the oscillations, friction factor and Nusselt number correlations were respectively obtained from Kays and London's plots of the friction factor and heat transfer coefficient versus Reynolds number

[26]. They obtained the equations of momentum and temperature from those two correlations. The set of equations proposed by them is incorporated in the well-known thermoacoustic calculation program—Design Environment for Low-amplitude Thermoacoustic Energy Conversion (DeltaEC) [38].

Empirical equations proposed for the mechanical Stirling engine are, no matter whether the experiments are conducted in a steady flow or oscillation flow, generally expressed by using the Reynolds number, although some of the researchers paid their attentions to the oscillation frequency.

From acoustics studies on random porous media

A general derivation of viscous loss and thermal conductivity loss for sound propagation in cylindrical tubes was first theoretically given by Kirchhoff in 1868 [39]. Zwikker and Kosten simplified the Kirchhoff theory by separately treating the thermal and viscous effects in terms of the complex density and compression modulus for the case of circular cross-sections in 1949 [40]. They extended the theory to tortuous flow channels, and discussed the experimental data of porous media like a felt and wood fibers based on the theoretical results of cylindrical tubes. The treatment of porous media by Zwikker and Kosten can be thought of as a "capillary-tube-based" modeling, as it assumes tortuous flow channels by a bundle of cylindrical tubes. This type of modeling has been widely employed to describe sound waves propagation in a random medium [41–43]. The theory of Zwikker and Kosten, however, only considers the wave propagation in a uniform temperature flow channel; thus the thermoacoustic power production was out of the scope of the theory.

For investigating the acoustic waves in porous media, Wilen and Petculescu developed a volume modulation technique (1998, 2001) [44, 45] and a lumped-element technique (2001) [46] to measure the complex compressibility and density of sound transmission through isotropic and anisotropic porous media, including stacked woven screens. Their measurement methods provided a convenient way for the survey a wide range of thermal penetration depths relative to the pore size.

Roh et al. (2007) [47] theoretically extended the thermoacoustic theory for random porous media with the capillary-tube-based modeling. Under the framework of the sound theory of Zwikker and Kosten, they introduced the thermal and dynamic shape factors to the dimensionless viscous wave number (also called as the shear wave number, being equivalent to r/δ_ν) and the thermal wave number (also called as the thermal disturbance number, equivalent to r/δ_α), and also tortuosity of complex porous media, for making the theory applicable to complicated flow channel. For porous media of reticulated vitreous carbon and aluminum foam, a good agreement between their extended theory and the experimental data measured by Wilen and Petculescu was shown by carefully adjusting parameters of shape factors and tortuosity, in the case of uniform temperature. In the next year, they also validated their theory on porous media with nonzero temperature gradients, for the case of a cotton wool stack [48]. They measured specific acoustic impedances ($= P/U$) at cold side of porous media in order to obtain the velocity gain which is formulated in the second term of the right hand side of Equation (1.6).

Ueda et al. (2009) [49] used the transfer function technique [50] to experimentally estimate the characteristic wavenumber and impedance of acoustic propagation in stacked-screen regenerators with uniform temperature and small oscillation amplitudes. Without using two characteristic lengths or shape factors and tortuosity, they could explain the experimental results using a single parameter in the capillary-tube-based modeling. In other words, they modeled the tortuous flow channels as a bundle of cylindrical tubes, and proposed an effective radius r_0 that reproduces the experimental data of the wavenumber and the characteristic impedance.

Obayashi et al. (2012) [51] have experimented the stacked-screen regenerator without the axial temperature gradients, and measured the acoustic power difference between both ends of the regenerator. Obayashi et al. have revealed that the acoustic power loss caused by the regenerator of the uniform temperature is proportional to cubic of the velocity amplitude. Based on experimental results of the uniform temperature regenerator, Obayashi proposed a flow resistance empirical equation parameterized by two non-dimensional quantities of Reynolds number Re_{h} and r_0/δ_ν. Their equation includes both the Tanaka's friction factor and Ueda's effective radius.

Guédra et al. (2015) [52] proposed an inverse method for estimating geometrical and thermal parameters of thermoacoustic stacks and regenerators using random porous media. With the capillary-tube-based modeling for complex pores of the regenerator, the inverse method is based on the transfer matrix characterized by a simplified version of the extension theory of Roh et al. without using shape factors. Because the transfer function technique used by Ueda et al. deals with the symmetry of the two-by-two transfer matrix, the technique is only based on the reciprocal nature of sound transmission through porous media with uniform temperature. The inverse method enables numerical estimations of a differentially heated regenerator from experimental data, which is capable of evaluating the porosity, an average inner radius of the pores, the tortuosity and the heat exchange coefficient with the walls.

A comprehensive literature review of sound propagation in the regenerator indicates the importance of the capillary-tube-based modeling. Also, it was found that systematic studies on heat transfer by oscillatory flow were lacking from acoustical point of view. Thermal effects of sound or oscillatory flow are problems that became to attract the attention only after the invention of thermoacoustic engines.

1.3 Dimensional analysis

Comparing both approaches reviewed in the last section, blind spots of respective aspects are apparent.

- Researchers of the mechanical Stirling engines usually explain the flow properties of the stacked-screen regenerator using the Reynolds number, by adopting the concept of a unidirectional steady flow in oscillation flow studies below 10 Hertz.
- Acousticians who investigate the thermoacoustic regenerator analyze the acoustic wave propagation in random pores with the capillary-tube-based modeling, by using the characteristic pore size and viscous/thermal penetration depths of the small amplitude gas oscillations.

We consider here dimensionless quantities that govern an oscillating pipe flow through a dimensional analysis. Olson and Swift have reported a similitude study for the thermoacoustic engine [53] in order to reveal the influence of different working gases through the specific heat ratio and the Prandtl number. They have pointed out several dimensionless groups that are important in the thermoacoustic engine system. In this section, a dimensional analysis is given for attaining key dimensionless parameters of a fluid element oscillating with angular frequency ω in a flow channel, following their study.

The continuity equation, Navier-Stokes equation, and the general equation of heat transfer are expressed with an ideal gas assumption and ignoring the body force [29] as:

$$\frac{\partial \rho}{\partial t} + \nabla \cdot (\rho \mathbf{v}) = 0, \tag{1.13}$$

$$\rho \left(\frac{\partial \mathbf{v}}{\partial t} + (\mathbf{v} \cdot \nabla)\, \mathbf{v} \right) = -\nabla \mathcal{P} + \mu \nabla^2 \mathbf{v}, \tag{1.14}$$

and

$$\rho c_{\mathrm{p}} \left(\frac{\partial \mathcal{P}}{\partial t} \right) - \left(\frac{\partial \mathcal{P}}{\partial t} \right) + \rho c_{\mathrm{p}} (\mathbf{v} \cdot \nabla)\, \mathcal{T} - (\mathbf{v} \cdot \nabla)\, \mathcal{P} = \nabla \cdot (k \nabla \mathcal{T}) + \Phi, \tag{1.15}$$

where ρ, t, $\mathcal{T}$, and μ respectively denote the density of the gas, time, temperature, and dynamic viscosity of the gas. In Cartesian coordinate system, $\mathbf{x}$ represents the position vector $\mathbf{x} = x_i \mathbf{i} + x_j \mathbf{j} + x_k \mathbf{k}$ and the velocity vector $\mathbf{v}$ is expressed as $\mathbf{v} = v_i \mathbf{i} + v_j \mathbf{j} + v_k \mathbf{k}$. The operator ∇ stands for $\mathbf{i} \left(\partial / \partial x_i \right) + \mathbf{j} \left(\partial / \partial x_j \right) + \mathbf{k} \left(\partial / \partial x_k \right)$, and $\mathbf{v} \cdot \nabla$ is interpreted as $v_i \left(\partial / \partial x_i \right) + v_j \left(\partial / \partial x_j \right) + v_k \left(\partial / \partial x_k \right)$. Also, in Equation (1.15), the term Φ is the rate of work done by the stresses in distorting the fluid, and this work is dissipated within the fluid as friction heat, which reads [29]

$$\begin{aligned} \Phi = \mu \Bigg[& 2 \left(\frac{\partial v_i}{\partial x_i} \right)^2 + 2 \left(\frac{\partial v_j}{\partial x_j} \right)^2 + 2 \left(\frac{\partial v_k}{\partial x_k} \right)^2 \\ & + 2 \left(\frac{\partial v_j}{\partial x_k} + \frac{\partial v_k}{\partial x_j} \right)^2 + 2 \left(\frac{\partial v_k}{\partial x_i} + \frac{\partial v_i}{\partial x_k} \right)^2 - \frac{2}{3} (\nabla \cdot \mathbf{v})^2 \Bigg]. \end{aligned} \tag{1.16}$$

These equations above can be non-dimensionalized in the following way.

A characteristic transverse length of the flow channel d and a reference velocity amplitude of the oscillating velocity V_0 are introduced as the representative length and velocity. It is different from the Olson and Swift's study who selected the total length of the thermoacoustic engine L and the sound speed a_0 at the reference temperature T_0 for the whole thermoacoustic engine system. Because the flow is assumed by a simple harmonic oscillation with ω, a period $1/\omega$ is utilized as a representative time. In view of the pipe flow, it is reasonable to consider a representative temperature difference Θ between the fluid and the solid wall for the normalization of the temperature $\mathcal{T}$. When the mean pressure is given, intrinsic thermal properties of the gas are characterized only by the reference temperature T_0; μ_0, k_0 and $c_{\mathrm{p},0}$ as a representative dynamic viscosity, thermal conductivity, and isobaric specific heat are determined by T_0. Also, a representative density ρ_0 are specified by the mean value of the pressure oscillation P_{m} and T_0 with the ideal gas law. In this way, dimensionless ratios are then introduced as follows:

$$
\begin{aligned}
&x^* = \frac{\mathbf{x}}{d}, \quad t^* = t\omega, \\
&P^* = \frac{\mathcal{P}}{\rho_0 V_0^2}, \quad \mathbf{v}^* = \frac{\mathbf{v}}{V_0}, \quad T^* = \frac{\mathcal{T}}{\Theta}, \quad \rho^* = \frac{\rho}{\rho_0}, \\
&\mu^* = \frac{\mu}{\mu_0}, \quad k^* = \frac{k}{k_0}, \quad {c_{\mathrm{p}}}^* = \frac{c_{\mathrm{p}}}{c_{\mathrm{p},0}},
\end{aligned}
\tag{1.17}
$$

where physical quantities with superscript $*$ denote a dimensionless form of the respective quantities. Also, a dimensionless operator $\nabla^* = \nabla d$ is introduced. By substituting these dimensionless ratios, equations of the continuity, momentum, and the general equation of heat transfer are rewritten as

$$
\frac{\partial \rho^*}{\partial t^*} + \frac{V_0}{d\omega}\nabla^* \cdot (\rho^* \mathbf{v}^*) = 0, \tag{1.18}
$$

$$
\rho^* \left(\frac{d\omega}{V_0} \frac{\partial \mathbf{v}^*}{\partial t^*} + (\mathbf{v}^* \cdot \nabla^*)\,\mathbf{v}^* \right) = -\nabla^* P^* + \frac{\mu_0}{\rho_0 d V_0} \mu^* \nabla^{*2} \mathbf{v}^*, \tag{1.19}
$$

and

$$
\begin{aligned}
\rho^* c_{\mathrm{p}}^* \frac{\partial T^*}{\partial t^*} - \frac{V_0^2}{c_{\mathrm{p},0}\Theta} \frac{\partial P^*}{\partial t^*} + \frac{V_0}{d\omega} \rho^* c_{\mathrm{p}}^* (\mathbf{v}^* \cdot \nabla^*)\, T^* - \frac{V_0^2}{c_{\mathrm{p},0}\Theta} \frac{V_0}{d\omega} (\mathbf{v}^* \cdot \nabla^*)\, P^* \\
= \frac{1}{d^2} \frac{k_0}{\rho_0 \omega c_{\mathrm{p},0}} \nabla^* \cdot (k^* \nabla^* T^*) + \frac{V_0^2}{c_{\mathrm{p},0}\Theta} \frac{1}{d^2} \frac{\mu_0}{\rho_0 \omega} \Phi^*.
\end{aligned}
\tag{1.20}
$$

The right hand side of Equation (1.20) includes $\delta_{\nu,0} = \sqrt{2\mu_0/\left(\rho_0\omega\right)}$ and $\delta_{\alpha,0} = \sqrt{2k_0/\left(\rho_0\omega c_{\mathrm{p},0}\right)}$, which are frequently used in the thermoacoustic theory. Here, $k_0/(\rho_0 c_{\mathrm{p},0})$ means the thermal diffusivity α, and μ_0/ρ_0 means the kinematic viscosity ν. Therefore, non-dimensional parameters are rewritten as $\frac{\mu_0}{\rho_0\omega} \Big/ d^2 = (d/\delta_{\nu,0})^{-2}$ and $\frac{k_0}{\rho_0\omega c_{\mathrm{p},0}} \Big/ d^2 = (d/\delta_{\alpha,0})^{-2}$. The non-dimensional ratio of $V_0^2/\left(c_{\mathrm{p},0}\Theta\right)$ appearing in Equation (1.20) is known as Eckert number Ec, which means kinetic energy of the flow relative to the boundary layer enthalpy difference between the solid wall and fluid [29, 54], and it is negligibly small when a representative velocity is much smaller than the adiabatic sound speed of gas a [54]. The dimensionless ratio of $V_0/(d\omega)$ occurring in the left-hand-side of Equations (1.18), (1.19), and (1.20) is seen as a dimensionless displacement, which can be rewritten as

$$\frac{V_0}{d\omega} = \frac{1}{2}\frac{2\mu_0}{\rho_0\omega}\frac{1}{d^2}\frac{\rho_0 d V_0}{\mu_0} = \frac{1}{2\left(d/\delta_{\nu,0}\right)^2}Re. \tag{1.21}$$

where $Re = \rho_0 d V_0/\mu_0$. Therefore, the non-dimensional governing equations for the oscillation fluid element are now given as:

$$\frac{\partial\rho^*}{\partial t^*} + \frac{Re}{2\left(d/\delta_{\nu,0}\right)^2}\nabla^*\cdot(\rho^*\mathbf{v}^*) = 0, \tag{1.22}$$

$$\rho^*\left(\frac{2\left(d/\delta_{\nu,0}\right)^2}{Re}\frac{\partial\mathbf{v}^*}{\partial t^*} + \left(\mathbf{v}^*\cdot\nabla^*\right)\mathbf{v}^*\right) = -\nabla^*P^* + \frac{1}{Re}\mu^*\nabla^{*2}\mathbf{v}^*, \tag{1.23}$$

and

$$\begin{aligned}\rho^*c_{\mathrm{p}}^*\frac{\partial T^*}{\partial t^*} - Ec\frac{\partial P^*}{\partial t^*} + \frac{Re}{2\left(d/\delta_{\nu,0}\right)^2}\rho^*c_{\mathrm{p}}^*\left(\mathbf{v}^*\cdot\nabla^*\right)T^* - Ec\frac{Re}{2\left(d/\delta_{\nu,0}\right)^2}\left(\mathbf{v}^*\cdot\nabla^*\right)P^* \\ = \frac{1}{2\left(d/\delta_{\alpha,0}\right)^2}\nabla^*\cdot\left(k^*\nabla^*T^*\right) + \frac{Ec}{2\left(d/\delta_{\nu,0}\right)^2}\Phi^*.\end{aligned} \tag{1.24}$$

It is found that Re, $d/\delta_{\nu,0}$, and $d/\delta_{\alpha,0}$ are the key parameters of the thermovicous fluid with nonzero α and ν and oscillating in the flow channel with finite velocity. As mentioned in the literature review of Subsection 1.2.2, studies of complex porous media from acoustical point of view only discuss non-dimensional parameters $r/\delta_\sharp$ ($\sharp = \alpha$ or ν) [41–43, 48, 49, 52], while Stirling engine studies insist to use Re [32–34, 37] by ignoring $r/\delta_\sharp$. Now the need of a more general treatment is clear. For example, as for the pressure loss in the regenerator, at least two parameters Re, $d/\delta_{\nu,0}$ are necessary because the dimensionless equation of motion is expressed using them.

1.4 Objectives of this study

Based upon the background, overall survey and dimensional analysis in previous sections, the primary objective of present research is to improve the empirical knowledges of the stacked-screen regenerator that are used in the thermoacoustic engines. For this purpose, following sub-objectives have been implemented.

1. To investigate the acoustic power variations ΔW in the stacked-screen regenerator by changing the oscillatory flow velocity and the oscillation frequency.

2. To investigate the heat power Q transmitted through the stacked-screen regenerator with changing the oscillatory flow velocity and the oscillation frequency.

3. To validate the empirical knowledges obtained from experiments of W and Q by predicting the thermoacoustic engine performance and comparing with measurements.

1.5 Thesis outline

The current research aims to experimentally study the stacked-screen regenerator for improvement of the thermoacoustic engine design.

In Chapter 2, acoustic power dissipations across the regenerator are measured for investigating the flow resistance of the uniform temperature regenerator with varying the velocity amplitude and the oscillation frequency. Experimentally obtained flow resistance is compared with three empirical equations frequently used in the thermoacoustic and Stirling engine design.

Chapter 3 derives an effective radius r_{eff} from the flow resistance empirical equation, using the capillary-tube-based modeling for tortuous flow channels of the stacked-screen regenerator. The effective radius r_{eff} is further tested by measurements when the regenerator has temperature gradients. The acoustic power difference ΔW across the stacked-screen regenerator with and without temperature gradients is explained by the effective radius of r_{eff}, under the framework of the thermoacoustic theory.

In Chapter 4, the heat flow Q transmitted through the stacked-screen regenerator is measured and compared with four empirical equations. The results indicate that the simplest formulation using the effective radius r_0 explains the measured heat flow Q to a similar degree to other empirical equations parameterized by Reynolds number and Nusselt number.

Chapter 5 proposes a numerical calculation method using two effective radii r_0 and r_{eff} and tests them through measurements of spontaneous gas oscillation induced in the thermoacoustic engine equipped with the stacked-screen regenerator. By doing so, the applicability of two effective radii r_0 and r_{eff} is shown.

Chapter 6 concludes the individual chapters and provide an overlook of the current study, and gives an outlook for the future improvement of this topic.

Chapter 2

Flow resistance of the stacked-screen regenerator

2.1 Introduction

When a gas column oscillates in a pipe, the energy dissipation unavoidably takes place due to the pressure loss, and results in the decrease of the acoustic power

$$W = \frac{1}{2} A \mathrm{Re}\left[P \widetilde{U}\right], \tag{2.1}$$

where A is the cross sectional area of the pipe, P and U denote the complex amplitude of pressure and cross-sectional averaged velocity, $\mathrm{Re}\,[\cdots]$ means taking the real part, and $\widetilde{U}$ stand for the complex conjugate of U. If A is constant, the acoustic power change per unit length is decomposed as

$$\frac{dW}{dx} = \frac{1}{2} A \mathrm{Re}\left[\widetilde{U} \frac{dP}{dx}\right] + \frac{1}{2} A \mathrm{Re}\left[\widetilde{P} \frac{dU}{dx}\right]. \tag{2.2}$$

Substitution of dP/dx of the equation of motion in Equation (1.1) into the first term of the right-hand side of Equation (2.2) gives after some algebraic manipulation

$$\frac{1}{2} A \mathrm{Re}\left[\widetilde{U} \frac{dP}{dx}\right] = \frac{A\omega\rho_{\mathrm{m}}}{2} \mathrm{Im}\left[\frac{1}{1-\chi_\nu}\right] |U|^2 = -\frac{1}{2} R_\nu (A\,|U|)^2, \tag{2.3}$$

where

$$R_\nu = -\frac{\omega\rho_{\mathrm{m}}}{A} \mathrm{Im}\left[\frac{1}{1-\chi_\nu}\right] \tag{2.4}$$

is called the flow resistance caused by the viscous interaction between the gas and the channel walls, ω and ρ_{m} are respectively the angular frequency and the time-averaged density of the working gas, and χ_ν is the thermoacoustic function of the viscous effect. In the equation, $\mathrm{Im}\,[\cdots]$ means taking the imaginary part. Therefore, the associated acoustic power decrease ΔW over length l of the pipe is given by

$$\Delta W = -\frac{l}{2} R_\nu (A\,|U|)^2. \tag{2.5}$$

In the case of the staked screen regenerator, it is often difficult to directly measure the oscillation velocity, but we can readily derive it from the velocity outside of it. Considering the continuity of the volume velocity at the interface between the regenerator and the pipe, the oscillation velocities U in the pipe region and V in the regenerator region are related to each other by $AU = A\phi V$, where ϕ is the volume porosity of the regenerator. With this relationship, R of the regenerator is expressed per unit length as

$$R = -\frac{2\Delta W}{l\big(A\phi|V|\big)^2}, \tag{2.6}$$

For tiny flow channels like in the stacked screen regenerator, the contribution from the second term of Equation (2.2) is negligibly small, and therefore, the acoustic power loss originates from the flow resistance R_ν.

Because the functional form of χ_ν is analytically obtainable for regular flow channels [12–14], it is possible to accurately determine the acoustic power loss once the volume velocity AU is given. For the stacked screen regenerators, however, a full theoretical analysis is difficult because of the complexity of the flow channels. So lots of efforts have been made to experimental derivation of the empirical equation of R_ν. Particularly because of the needs of the heat exchanger and mechanical Stirling engine design [26], many experimental studies have been conducted using the stacked-screen regenerators. In this chapter, representative empirical equations of R_ν are introduced, and the acoustic resistance R_ν of the stacked-screen regenerator is experimentally investigated to verify them.

2.2 Empirical equations of viscous flow resistance

Swift and Ward have provided a flow resistance empirical equation as:

$$R_\mathrm{S} = \frac{\nu\rho_\mathrm{m}}{(d_\mathrm{h}/4)^2 A\phi}\left(\frac{c_1}{3\pi}Re_\mathrm{h} + \frac{c_2}{8}\right), \tag{2.7}$$

where Re_h is defined as $Re_\mathrm{h} = |V|d_\mathrm{h}/\nu$ by using the oscillation amplitude of the velocity $|V|$ and the hydraulic diameter d_h of flow channels in the regenerator, and the kinematic viscosity ν of the working gas. In this equation, $c_1 = -2.82 + 10.7\phi - 8.6\phi^2$ and $c_2 = 1268 - 3545\phi + 2544\phi^2$. Equation (2.7) was deduced by assuming that the instantaneous pressure loss is represented by the steady flow friction factor of Kays and London and by taking time average for a period of harmonic oscillation flow. Although Equation (2.7) is incorporated into the well-known thermoacoustic calculation program—Design Environment for Low-amplitude Thermoacoustic

Energy Conversion (DeltaEC) [38], the applicability should be further confirmed in oscillatory flow experiments.

For improvement of mechanical Striling engine design, Gedeon and Wood obtained the empirical equation of the friction factor, which can be written in the form of flow resistance as

$$R_{\mathrm{G}} = \frac{\rho_{\mathrm{m}} |V|}{2A\phi l d_{\mathrm{h}}} \left(\frac{129}{Re_{\mathrm{h}}} + 2.91 {Re_{\mathrm{h}}}^{-0.103} \right). \tag{2.8}$$

Their friction factor was obtained from the experiments with rather fine mesh screens (#80, #100 and #200 meshes). In the case of coarse mesh screens suitable for thermoacoustic and mechanical Stirling engine regenerators, the applicability has not yet been verified.

Recently, Obayashi et al. have given an flow resistance empirical equation of

$$R_{\mathrm{O}} = R_{\nu} + \frac{0.8\rho_{\mathrm{m}}\nu}{A\phi d_{\mathrm{h}}^2} Re_{\mathrm{h}}, \tag{2.9}$$

where R_{ν} is determined by considering the volume porosity ϕ of the stacked-screen regenerator and replacing r of Equation (2.4) with the effective radius r_0 of Ueda et al. given as

$$r_0 = \frac{\sqrt{d_{\mathrm{h}} d_{\mathrm{w}}}}{2}, \tag{2.10}$$

where d_{w} is the wire diameter of the wire woven mesh screen. Equation (2.9) of Obayashi et al. consists of the flow resistance R_{ν} obtained from the thermoacoustic theory of the small oscillation amplitude assumption and the Reynolds-number-dependent term adopted from the friction factor of Tanaka et al. Because Equation (2.9) was proposed from experiments with air at atmospheric pressure as the working gas, it should be tested in pressurized gases of low Prandtl number for practical thermoacoustic engine design.

2.3 Experimental setup

2.3.1 Configuration of loudspeaker for experiment

In the studies of Stirling engine or pulse tube cryocoolers, solid pistons linked with mechanical cranks [32, 55] or Scotch yokes [35, 36] driven with an electric motor are usually used to generate the reciprocating flow in a cylindrical tube. Such mechanical drivers can operate only at a rather low frequency range below 100 Hz, because of friction and vibration problems. Also, because the piston displacement is often mechanically fixed, the oscillation velocity changes only in proportional to the oscillation frequency. Therefore, changing arbitralily the velocity amplitude is difficult. In this study, the loudspeaker is employed to excite the oscillatory flow in place of pistons, in order to attain the acoustic fields with frequencies up to audio frequency range. However, commercially available loudspeakers are incapable of creating sufficiently large velocity when pressurized gases are used as the working gas, as they are designed to operate in air at atmospheric pressure. Therefore, multiple loudspeakers shown in Figures 2.1 (a) and 2.1 (b) are used to produce acoustic fields with large velocity amplitude.

Figure 2.1 (a) presents a loudspeaker pair in parallel configuration, whereas Figure 2.1 (b) is in series. An analogous circuit diagram of series configurations is drawn in Figure 2.1 (c). In the figure, P is oscillation pressure produced by the electrodynamic force generating from the moving-coil and the magnet of the loudspeaker, and U is the resulting oscillation velocity flowing in the resonance tube, Z_{me} and Z_{a} respectively represent impedances of the mechanical system of the loudspeaker and the acoustical system which will be connected with other acoustic components. In Figure 2.1 (c), two oscillation pressure sources are arranged in series, so the pressures are added up, resulting in an enlarged oscillation velocity U. This configuration is particularly useful when the loudspeaker positions are close to the pressure maximum, where the higher oscillating force is critically important. On the other hand, when the loudspeaker position is close to the velocity maximum, the parallel configuration is adopted because the larger volume velocity is more important than the large oscillation force.

Figure 2.2 shows the experimental configuration used in this study. It consists of a 40-mm inner diameter cylindrical tube containing a 35-mm long regenerator holder in the middle, and acoustic driver pairs (FW168N; Fostex Co., Tokyo, Japan) at the ends. The past acoustical experimental studies for investigating porous media used one acoustic driver at one end, while the other end closed by a rigid plate [44–46, 49, 56]. In such a experimental setup, the length of the cylindrical tube or the position of the regenerator in the tube are the only parameters to adjust the acoustic fields. In the experimental configuration, various acoustic fields can be created through the amplitude ratio and the temporal phase difference between the two loudspeaker pairs. The experimental setup illustrated in Figure 2.2 enables convenient adjustments of the acoustic field at the position of the regenerator holder, without changing the length of the tube. Figure 2.3 shows the photo of the experimental setup example, where totally eight loudspeakers were used. When the stacked-screen regenerator with mesh number of #30 is tested in this experimental configuration filled with pressurized helium at 0.45 MPa, the highest velocity amplitude attainable is about 6 m/s at location of the regenerator holder, while the highest frequency tested is 200 Hz. Both conditions are sufficiently high to discuss the velocity and frequency dependences of oscillatory flow properties of the stacked screen regenerators.

2.3.2 Experimental procedure

In the experimental setup shown in Figure 2.2, the coordinate x was set from left to right of the tube. Either He or Ar gas fills the cylindrical tube, with a mean pressure of 0.45 MPa at ambient temperature. 35-mm long randomly stacked woven wire mesh screens were installed in the regenerator holder which was set in the area from x_1 =0.720 m to x_2 =0.755 m in the tube. Also, a 35-mm long cylindrical ceramic honeycomb catalyst having square pores was used as a reference of a regular flow channel regenerator. Table 2.1 presents parameters of the

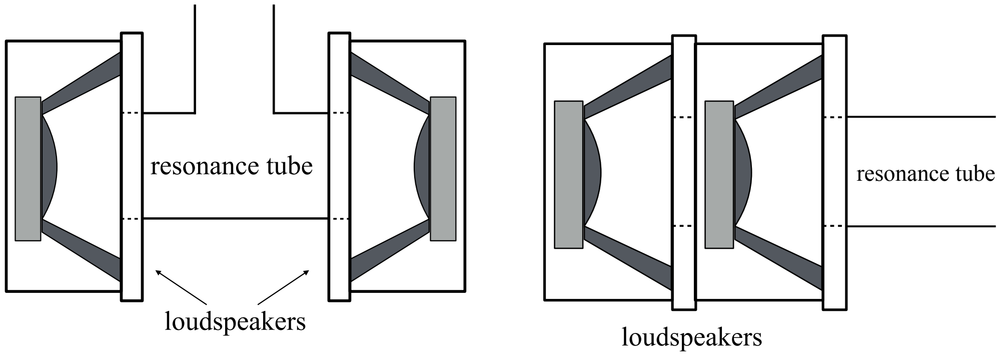
resonance tube
loudspeakers
resonance tube
loudspeakers

(a) loudspeakers in parallel configuration. (b) loudspeakers in series configuration.

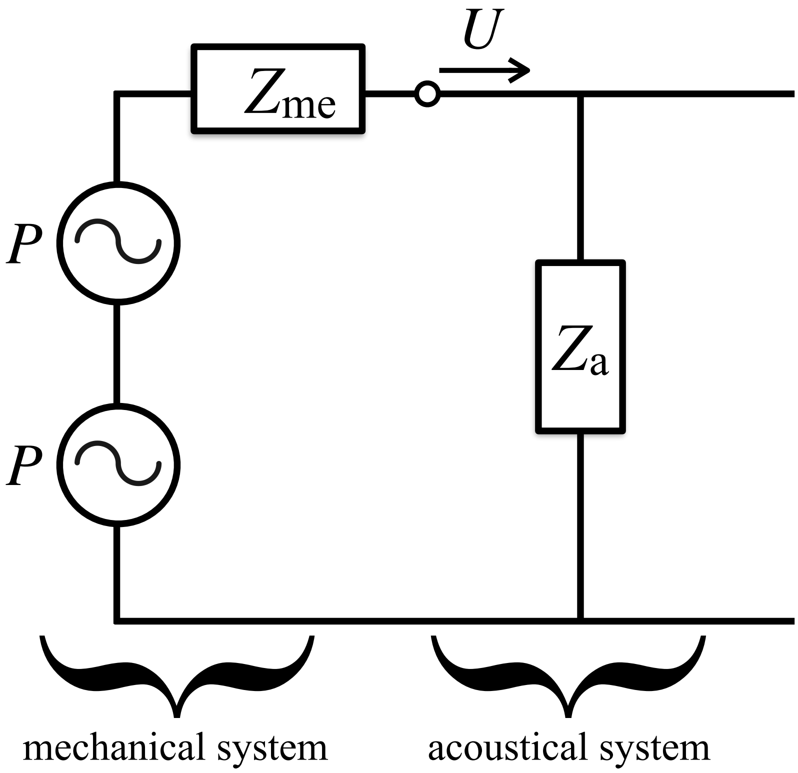
U
Zme
P
P
Za
mechanical system
acoustical system

(c) Impedance-type analogus circuit.

Figure 2.1: Loudspeaker configuration.

wire meshes and ceramic honeycomb used for this study. The mesh number of woven screens means the number of openings per inch, while the cell number of ceramic honeycomb gives the number of openings per square inch. The volume porosity ϕ of regenerator was defined as a fraction of the void space volume over the total volume of the regenerator holder filled with regenerator materials, which was determined from the measured weight and the density of steel and ceramic. For regular flow channel regenerator of ceramic honeycomb, the hydraulic diameter d_h was calculated as four times the cross sectional area divided by the perimeter. In the case of stacked-screen regenerator, the hydraulic diameter is defined as $d_\mathrm{h} = \phi d_\mathrm{w}/\left(1 - \phi\right)$.

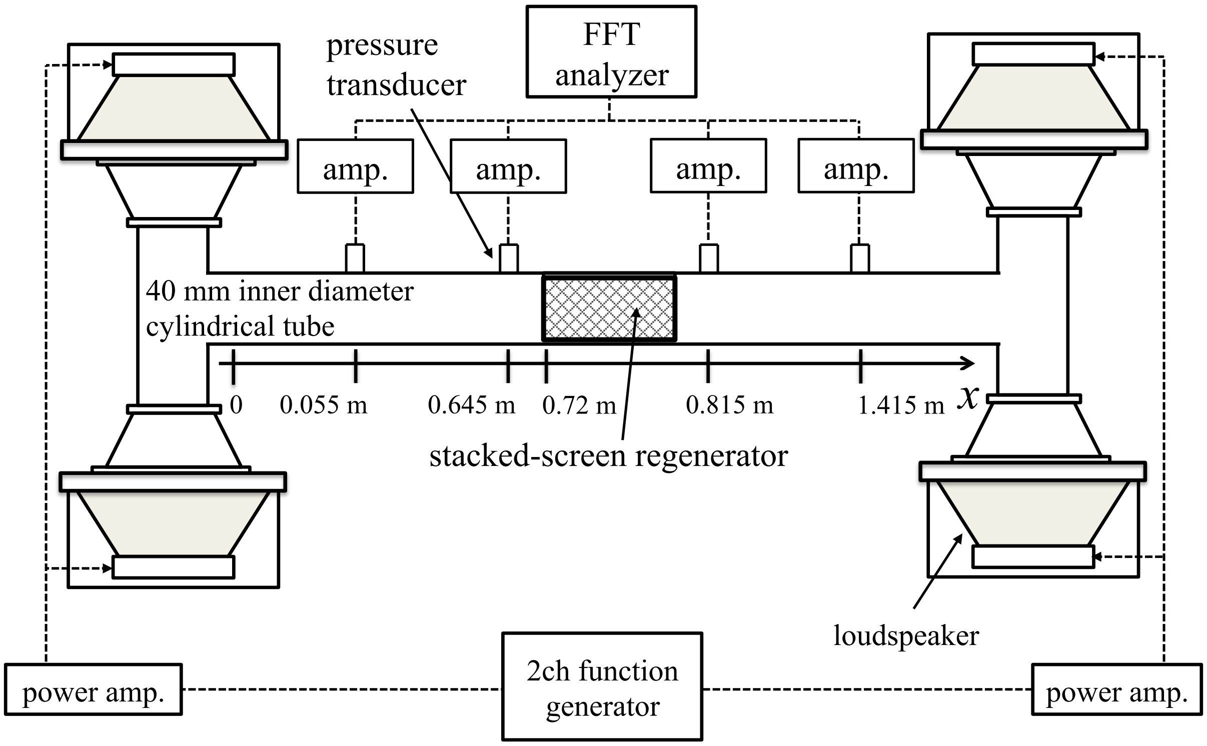
pressure transducer
FFT analyzer
amp.
amp.
amp.
amp.
40 mm inner diameter cylindrical tube
0
0.055 m
0.645 m
0.72 m
0.815 m
1.415 m
x
stacked-screen regenerator
loudspeaker
power amp.
2ch function generator
power amp.

Figure 2.2: Schematic diagram of the experimental setup. (Figure adapted from Reference 57 and modified by author.)

Two pairs of pressure transducers (PD104; JTEKT Corp., Osaka, Japan) were mounted on the cylindrical tube sidewalls for acoustic field measurements. The acoustic pressure amplitude and phase at the transducer positions were determined using a 24-bit fast Fourier transform analyzer (DS-3100; Ono Sokki Co. Ltd., Yokohama, Japan). By using the two-sensor method [58, 59], the acoustic pressure $p(x,t) = \mathrm{Re}\left[P(x)\exp(i\omega t)\right]$ and the radial average of the axial acoustic particle velocity $u(x,t) = \mathrm{Re}\left[U(x)\exp(i\omega t)\right]$ in the regions of $x \leq x_1$ and $x \geq x_2$ were experimentally determined, where $\natural = 1$ and 2 respectively denote the inlet-side and the outlet-side of regenerator at $x = 0.720$ m, and at x =0.755 m.

In order to test the regenerator in the traveling-wave field, the specific acoustic impedance $Z(x) = P(x)/U(x)$ in the region with $x \geq x_2$ was tuned to become equal to the characteristic specific acoustic impedance $\rho_\mathrm{m}a$ of the working gas, where a is the adiabatic sound speed of the gas. An example of the experimental acoustic field was shown in Figure 2.4.

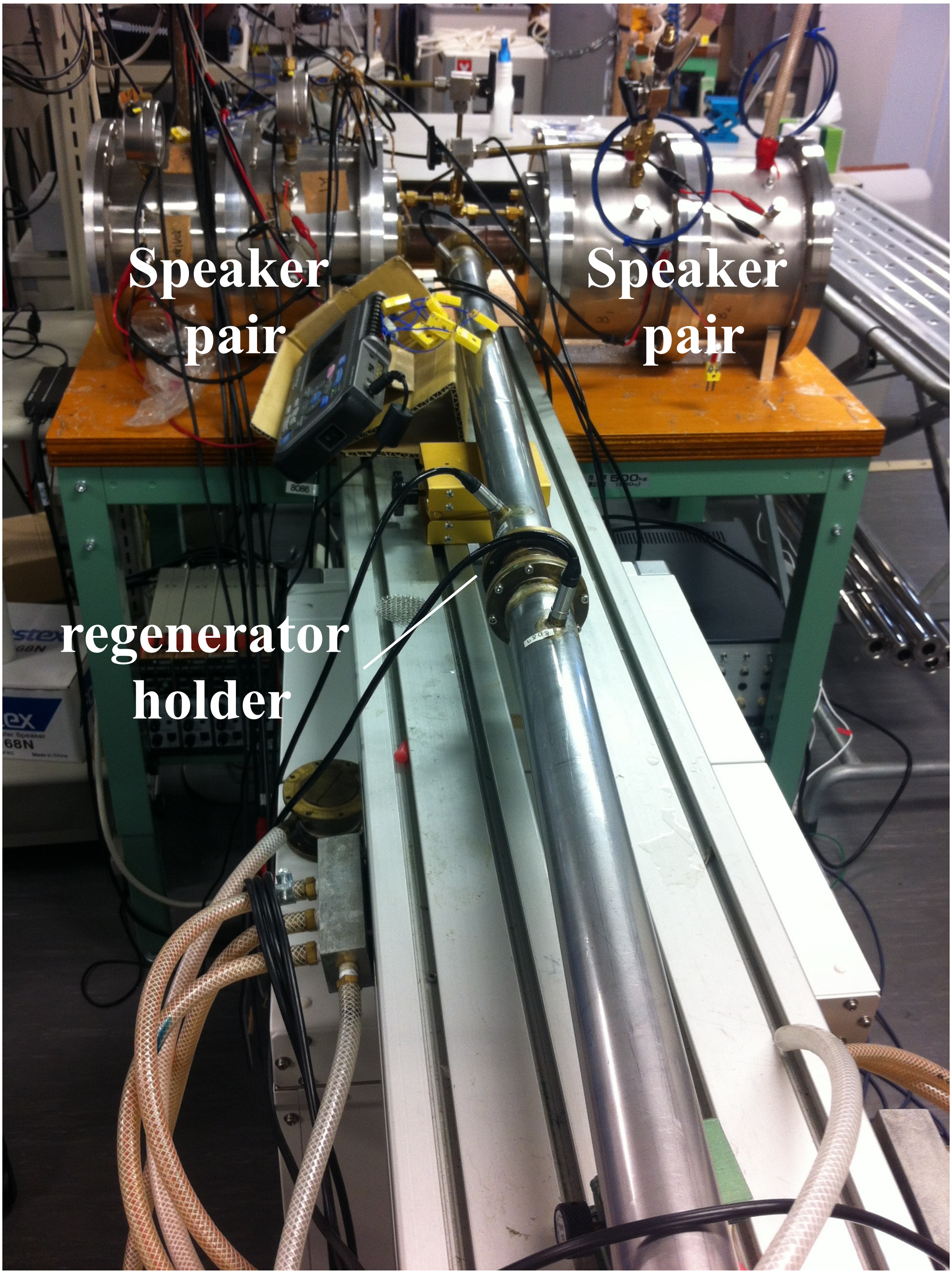
Speaker pair
Speaker pair
regenerator holder

Figure 2.3: Photo of experimental configuration, which shows one end of the 40-mm-inner-diameter cylindrical tube and the regenerator holder. Two series speaker pairs arranged in opposite are harnessed in the one end of the cylindrical tube, where total eight loudspeakers were used in this experimental setup.

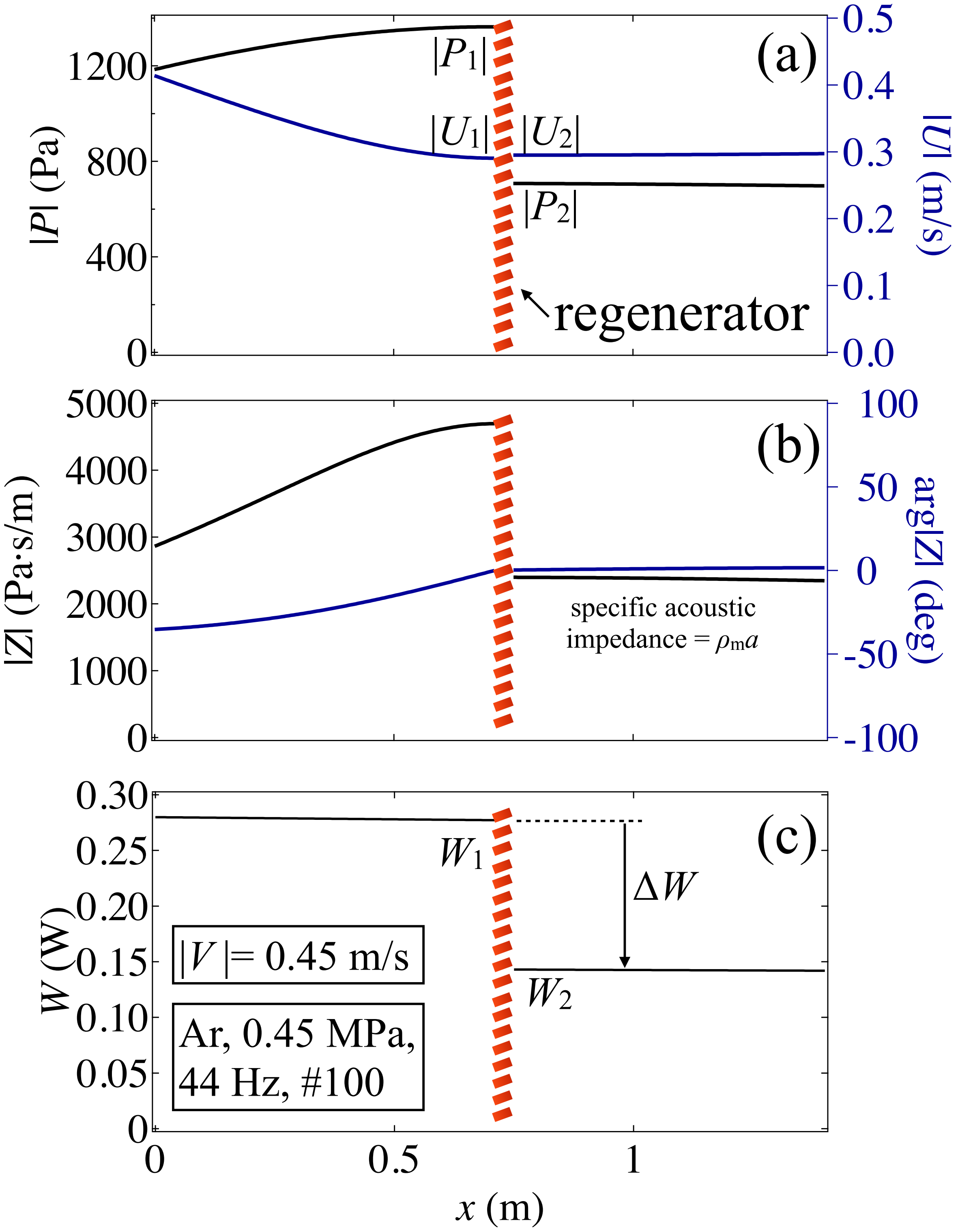

Figure 2.4: Measured acoustic field with #100 mesh, $|V| = 0.45$ m/s, 44 Hz, and argon gas. The black and blue curves in (a) represent the pressure amplitude $|P|$ and the amplitude $|U|$ of the cross-sectional averaged velocity, respectively. The black and blue curves in (b) represent the magnitude of acoustic impedance $|Z|$ and its phase $\arg[Z]$, respectively. Also, black lines shown in (c) represent acoustic power distributions in the upstream and downstream of the regenerator, and the acoustic power difference ΔW between the both ends of the regenerator is determined with $\Delta W = W_1 - W_2$.

Table 2.1: Geometrical properties of regenerators.

Stacked-screen regenerator			
Mesh number	Wire diameter (mm) d_{w}	Hydraulic diameter (mm) d_{h}	Volume porosity ϕ
30	0.22	0.8	0.78
50	0.14	0.47	0.77
60	0.12	0.40	0.77
100	0.1	0.22	0.69

Ceramic honeycomb catalyst			
Cell number		Hydraulic diameter (mm) d_{h}	Volume porosity ϕ
1200		0.68	0.89

The acoustic power $W_\natural$ at both ends of the regenerator were evaluated from the pressure $p_\natural = p(x_\natural, t)$ and the velocity $u_\natural = u(x_\natural, t)$ as

$$W_\natural = \frac{1}{2} A \left|P_\natural\right| \left|U_\natural\right| \cos\theta_\natural, \tag{2.11}$$

where $P_\natural$ and $U_\natural$ are the complex amplitudes of $p_\natural$ and $u_\natural$, whereas $\theta_\natural$ denotes the phase lead of $P_\natural$ relative to $U_\natural$. The acoustic power differences ΔW was derived as $\Delta W = W_2 - W_1$, which is shown in Figure 2.4. Although the acoustic power change can include the acoustic power dissipation due to the velocity gradient caused by the thermal conductivity of the gas in Equation (2.2), its contribution is negligibly small in the present experiments because of the tiny pores in the regenerator and also because of the specific acoustic impedance close to $\rho_{\mathrm{m}} a$. Therefore, the measured ΔW can be seen as the power loss due to the gas oscillations with velocity amplitude V in the regenerator with flow resistance R.

The velocity amplitude V in the regenerator region is obtained from $U_\natural$ as follows. From the continuity of the volume velocity, the velocity on each side of the regenerator is given by $V_\natural = U_\natural/\phi$ ($\natural = 1, 2$). Figure 2.5 illustrates the relation of velocity V in the regenerator and the velocity U in the pipe. The velocity amplitude V in the regenerator is then determined by the average of $V_1 (= U_1/\phi)$ and $V_2 (= U_2/\phi)$ as $V = (V_1 + V_2)/2$. By using the measured ΔW and $|V|$, the experimental flow resistance R of the regenerator was derived from Equation. (2.6).

2.4 Experimental results

Measurements were repeated four times for each of the regenerators in Table 2.1 under the same driver settings. Acoustic power decreases ΔW through the regenerators versus the velocity amplitude $|V|$ are plotted in Figure 2.6, where panels (a) and (b) are respectively for Ar and He. In the figures, the symbols with the error bars are plotted from the mean values and their standard

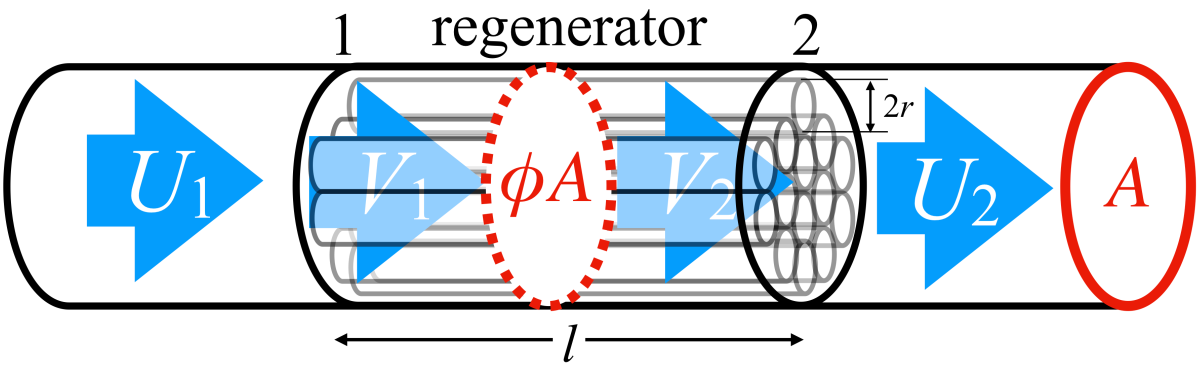

Figure 2.5: Schematic diagram of the relation of velocity V in the regenerator and the velocity U in the pipe. The volume porosity is expressed by ϕ.

deviations of experiments. The acoustic power decrease ΔW becomes significant with velocity amplitude $|V|$ and with increasing the mesh number. The regular pore regenerator of the ceramic honeycomb of 1200 cell presents the lower acoustic power decreases than the stacked-screen regenerator of #30, although the hydraulic diameter of the ceramic honeycomb is smaller than that of #30 regenerator, as listed in Table 2.1. Also, $A\phi$ of #30 regenerator and the ceramic honeycomb respectively give 3.9×10^{-7} m^2 and 3.2×10^{-7} m^2, which means that the the regenerator presents the larger acoustic power loss than the regular pore regenerator in spite of almost the same gas-occupied area. Therefore, the tortuous flow channel brings about the larger dissipations than the regular flow channel.

From the measured acoustic power change ΔW and the spatial mean velocity amplitude $|V|$ in the regenerator region, the flow resistance R was determined. Figures 2.7 (a) and 2.7 (b) are the relations between the flow resistance R and the velocity amplitude $|V|$ for argon and helium gases, respectively, at a fixed oscillation frequency of 44.0 Hz, which gives the viscous penetration depth $\delta_\nu = 0.15$ mm for Ar and 0.45 mm for He. In the case of the ceramic honeycomb, the experimental resistance R was found to be independent of $|V|$. Experimental results of the ceramic honeycomb agree with the theoretical prediction R_ν obtained using Equation (2.4) by inserting one-half of the hydraulic diameter ($d_\mathrm{h}/2 = 340\ \mu$m) into r and considering the gas-occupied area ϕA. Predictions are shown by the thin lines in Figures 2.7 (a) and 2.7 (b), which also show the experimental R for all the stacked-screen regenerators. The resistance R increases linearly with $|V|$. For verification, the empirical resistances R_S, R_G and R_O obtained from Equations (2.7), (2.8) and (2.9) are respectively presented by dashed, doted, and solid lines in Figures 2.7 (a) and 2.7 (b).

Experimental results indicate that R_S based on steady flow data goes below the experimental values of R in Ar for #50 and #60 meshes, and R_G underestimates the R in the case of #50 and #60 meshes of Ar and He. Except for those meshes, R_S, R_G, and R_O show good agreement with R. As a result, experiments in this chapter lend support to the empirical resistances R_S, R_G, and R_O for oscillatory flows of pressurized He and Ar gases. Among them, empirical flow resistance of Obayashi et al. R_O demonstrated the best accuracy for all tested mesh screens. The maximum deviations between experimental R and empirical equation of R_O for Ar and He

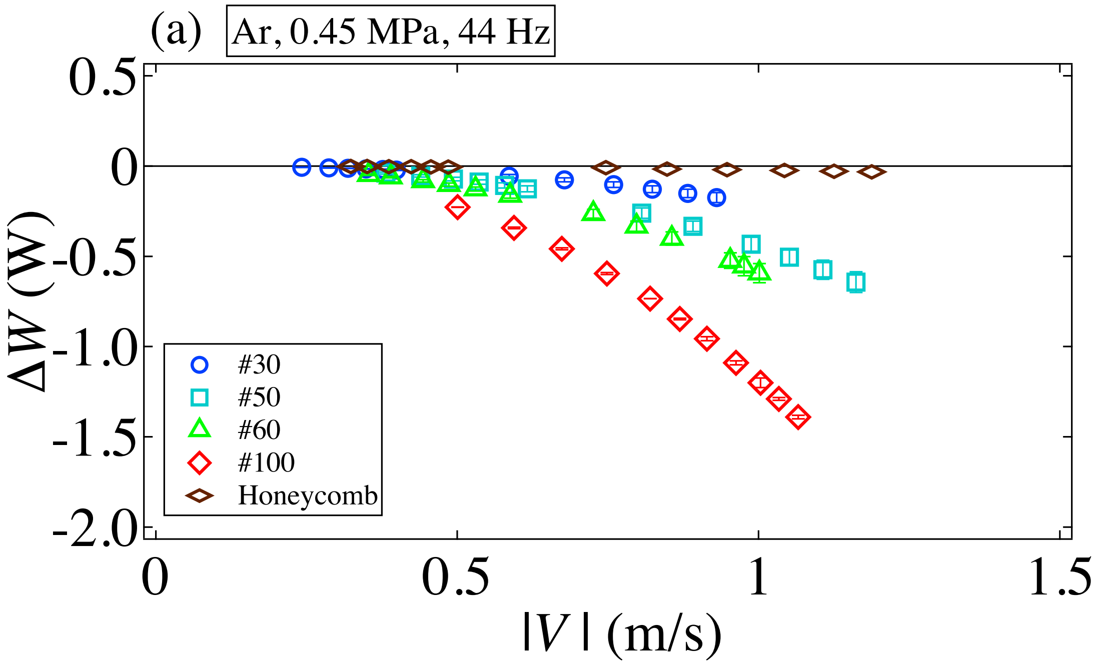

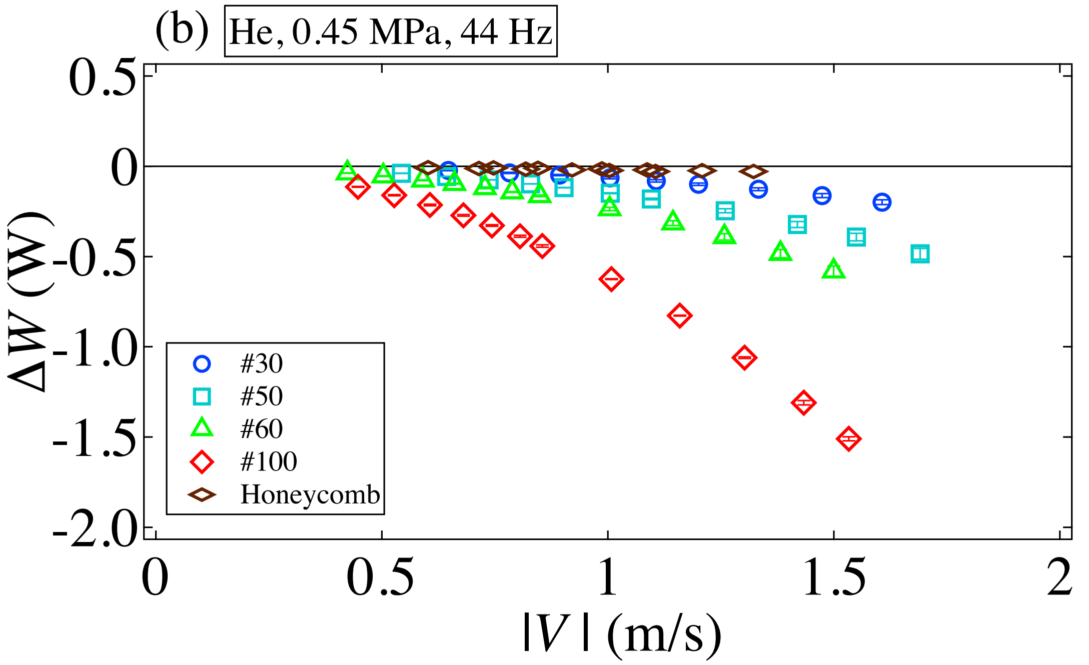

Figure 2.6: Acoustic power decrease ΔW versus the velocity amplitude $|V|$ of regenerators.

gases are, respectively, 11 and 9% in the case of #30 mesh; 14 and 5% in the case of #50 mesh; 4 and 7% in the case of #60 mesh; and 5 and 5% in the case of #100 mesh. Agreement of R_O in the small velocity region indicates that the stacked screen regenerator can be modeled with the bundle of cylindrical tubes with the effective radius r_0 as proposed by Ueda.

It should be noted that only Equation (2.9) of R_O shows the oscillation frequency dependence among three empirical equations listed in this chapter. It is because the term of R_ν in Equation (2.9) of R_O comes from the framework of the thermoacoustic theory. To test the oscillation frequency dependence, R_O and measured R of #100 mesh (symbols) with various oscillation frequencies of 20, 44, and 100 Hz are shown in Figures 2.8 (a) and 2.8 (b) for Ar and He gases, respectively. Both the empirical equation of Obayashi et al. and experimental resistance are hardly influenced by the frequency, although the term of R_ν in the right hand side of the Equation (2.9) should cause changes with frequency. It may be explained by the fact that the flow channel radius of the stacked-screen regenerator is much smaller than the penetration depth in cases of tested oscillation frequencies. In such cases, the thermoacoustic theory gives the flow resistance independent of the the frequency. The maximum deviations between the empirical equation and experimental values are 9 and 11%, respectively, for Ar and He. These results demonstrate the validity of the empirical equation of Obayashi et al. for air, He, and Ar as working gases, and for oscillation frequencies from 20 to 100 Hz.

2.5 Conclusions

For the regenerator located in acoustic fileds with the specific acoustic impedance close to $\rho_\mathrm{m}a$, the flow resistances were experimentally obtained from measurements of the acoustic powers at both sides of the regenerator. The results were compared with three empirical equations respectively proposed by Swift & Ward, Gedeon & Wood, and Obayashi et al. Experimental results lent support to empirical formulation of Obayashi et al. for all mesh screens tested in this study, and also presented the applicability of the steady-flow-based empirical equation of Swift & Ward on oscillatory flow. The friction factor of Gedeon & Wood was verified in the limited cases of fine mesh screens of #100 mesh and coarse mesh screens of #30 mesh. Furthermore, experiments conducted with various frequencies assured a wide applicability of the formulation of Obayashi et al.

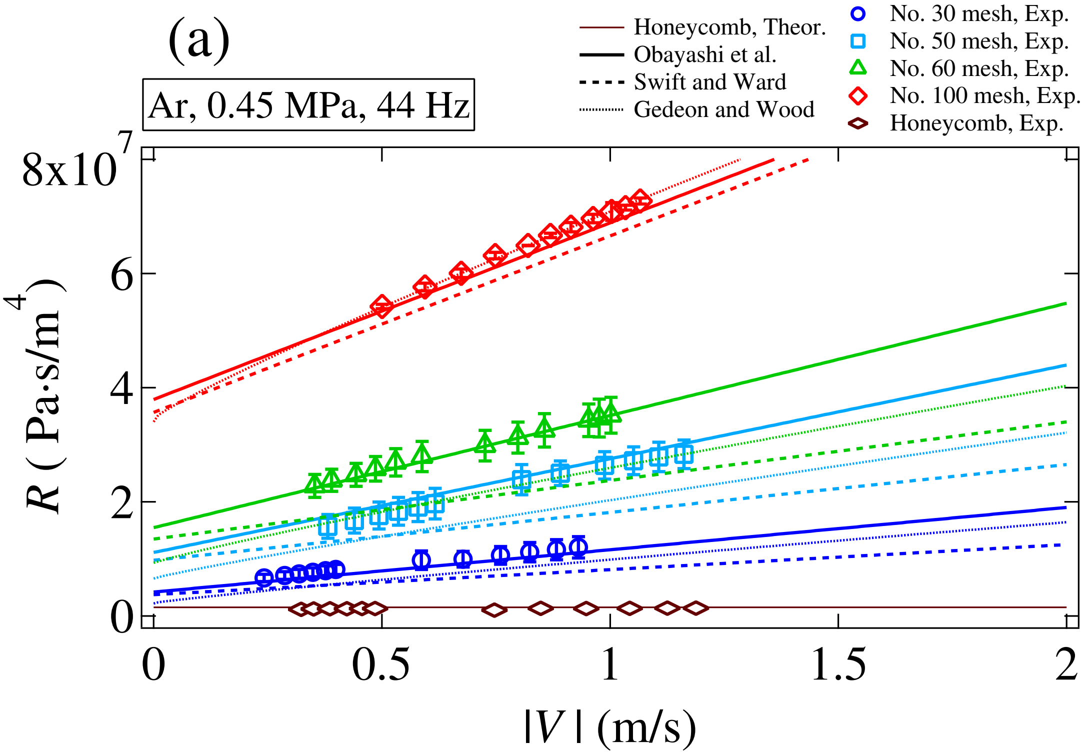

(a) Experimental results for 44 Hz and pressurized argon gas having mean pressure of 0.45 MPa.

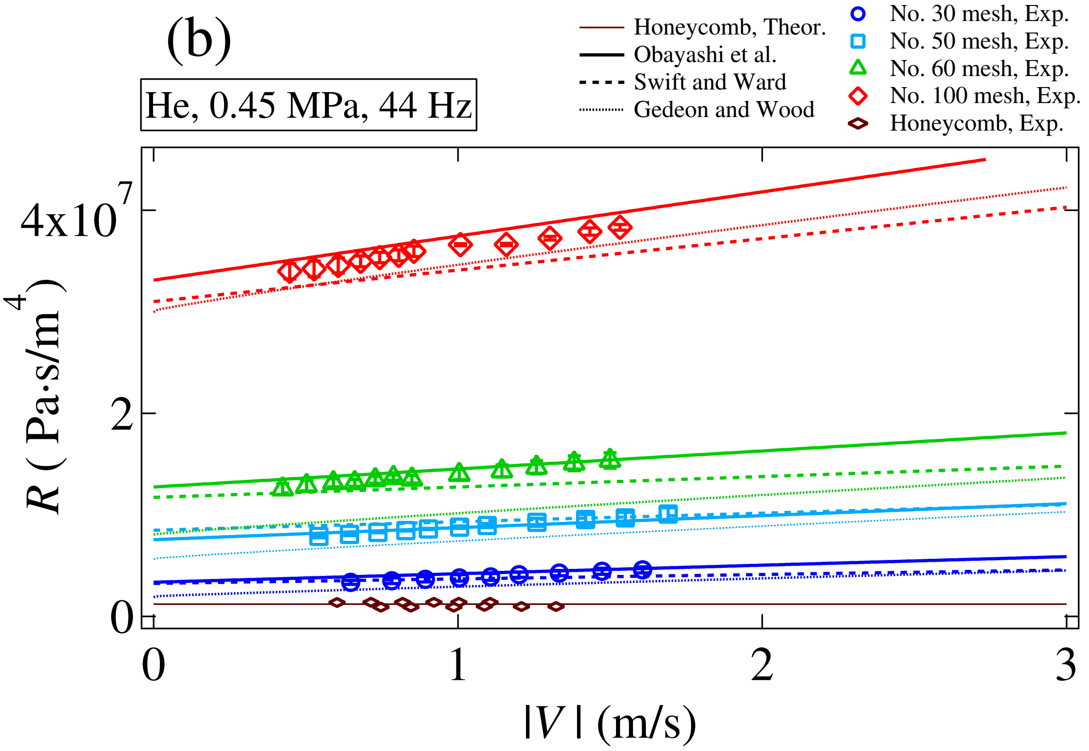

(b) Experimental results for 44 Hz and pressurized helium gas having mean pressure of 0.45 MPa.

Figure 2.7: Comparisons among the experimental flow resistance R, empirical Equations (2.7), (2.8) and (2.9) for the stacked-screen regenerator, and the theoretical calculation for the ceramic honeycomb. Experimental results are shown by symbols with error bars, resistances given by Equations (2.7), (2.8) and (2.9) are shown by dashed, doted and solid lines, respectively; the theoretical resistances for the ceramic honeycomb are shown by thin lines. (Figures adapted from Reference 57 and modified by author.)

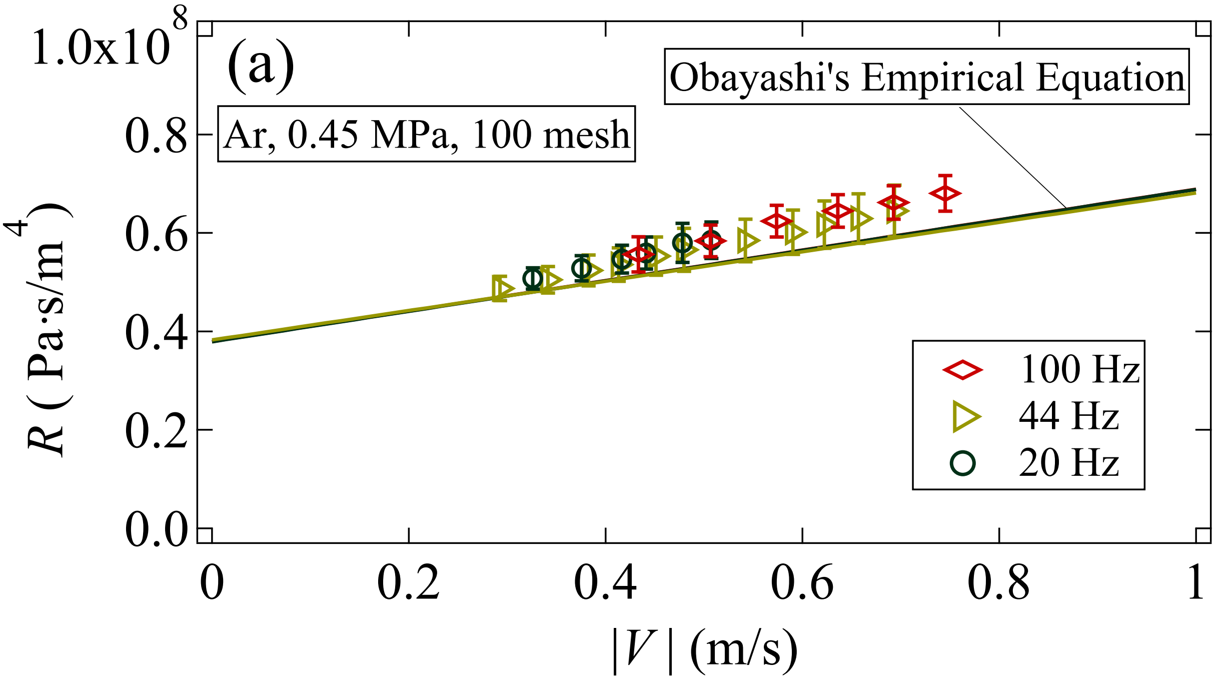

(a) Experimental results for pressurized argon gas having mean pressure of 0.45 MPa.

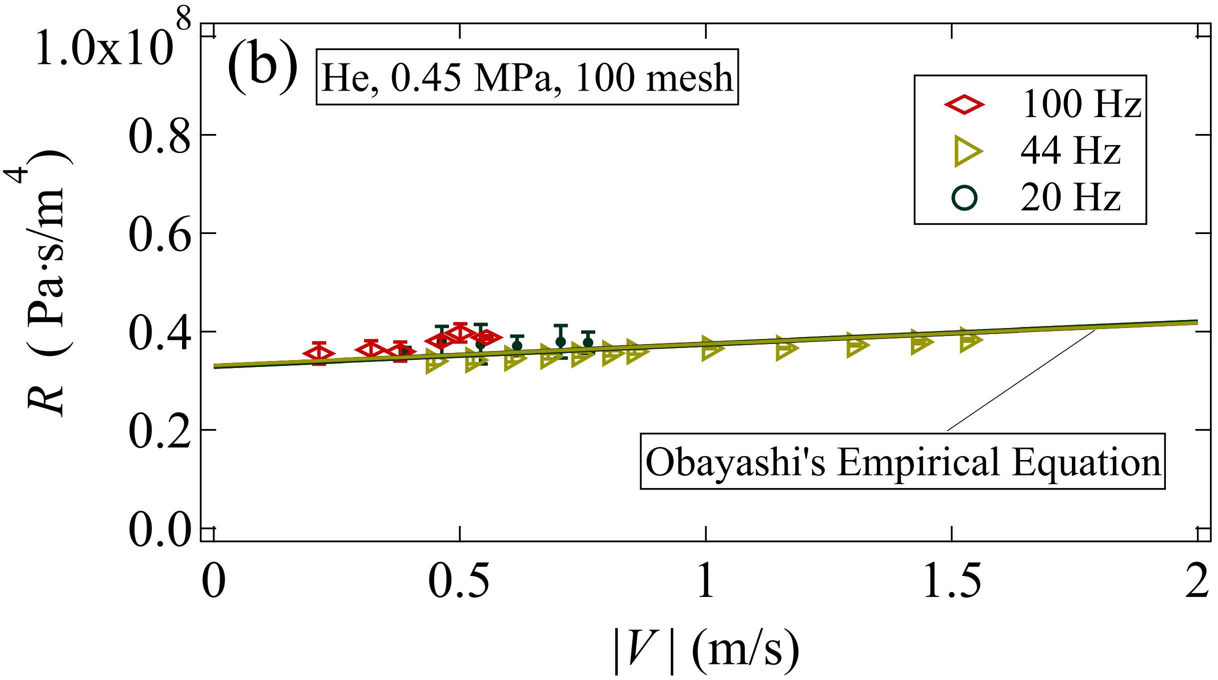

(b) Experimental results for pressurized helium gas having mean pressure of 0.45 MPa.

Figure 2.8: Comparisons between experimental flow resistance R and R_O for the stacked-screen regenerator using No. 100 mesh at various oscillation frequencies of 20, 44 and 100 Hz. Experimental results are presented by symbols with error bars. Predicted R_O values are shown by lines. (Figures adapted from Reference 57 and modified by author.)

Chapter 3

Cylindrical modeling of a stacked-screen regenerator

3.1 Introduction

The geometry of the pores in the stacked-screen regenerator is tortuous. A direct theoretical formulation of sound propagations through the regenerator is generally impossible. Modeling tortuous flow channels with simple regular geometry is an alternative approach from a phenomenological point of view. The effective cylindrical radius of Ueda et al. of Equation (2.10) has well characterized the flow resistance when the oscillation velocity is extremely small in the stacked-screen regenerator, as shown in Chapter 2. The formulation of Obayashi et al.

$$R_{\mathrm{O}} = R_{\nu} + \frac{0.8\rho_{\mathrm{m}}\nu}{A\phi d_{\mathrm{h}}^{2}} Re_{\mathrm{h}} \tag{3.1}$$

is an extension of the capillary-tube model of the empirical equation of Ueda et al. to the case with finite oscillation velocity, where ρ_{m} and ν are respectively the time-averaged density and kinematic viscosity of the working gas, ϕ and d_{h} respectively signify the volume porosity and hydraulic diameter of the stacked-screen regenerator. Also, R_{ν} is determined by considering ϕ and using the effective radius $r_0 = \sqrt{d_{\mathrm{h}} d_{\mathrm{w}}}/2$ of Ueda et al. with Equation (2.4), and the Reynolds number Re_{h} is defined as $Re_{\mathrm{h}} = |V| d_{\mathrm{h}}/\nu$, where d_{w} stands for the wire diameter of woven mesh screens, and $|V|$ denotes the spatial mean velocity amplitude in the region of the stacked-screen regenerator. In consistent with the dimensional analysis in Section 1.3, R_{O} is parametrized with two dimensionless quantities Re_{h} and r_0/δ_{ν}. However, from Equation (3.1) of Obayashi et al., only the flow resistance is estimated. To fully characterizing the thermoacoustic behavior of the stacked-screen regenerator, in this chapter, the capillary-tube model is modified to have an effective radius r_{eff} that changes with the velocity.

The capillary-tube-based modeling is assumed to have the same length l as the stacked screen regenerator and to consist of parallely-aligned N identical cylindrical pores with the effective radius r_{eff}, as shown in Figure 2.5. We define r_{eff} as that at which the flow resistance R_ν summed over the pores becomes the same as the flow resistance given by the empirical equation of Obayashi et al. (3.1). The number N of the pores is determined by r_{eff}, in such a way that the gas-occupied volume $N\pi r_{\mathrm{eff}}^2 l$ becomes equal to that (= ϕAl) in the regenerator. The derivation of the effective radius is given below in more detail. Also, to verify the effective radius r_{eff} thus obtained, this chapter experimentally tests the stacked-screen regenerator that has axial temperature difference, and compares the results with the effective radius r_{eff}.

3.1.1 Derivation of effective radius

The effective radii r_0 of Ueda et al. are evaluated as 0.21, 0.13, 0.11, and 0.07 mm for the test mesh screens with No. 30, 50, 60, and 100 meshes, respectively. These radii are rather small compared to the viscous penetration depth $\delta_\nu = \sqrt{2\nu/\omega}$ (ω stands for the oscillation angular frequency), as it is 0.15 mm for Ar and 0.45 mm for He when the oscillation frequency is 44 Hz. Furthermore, if the increase of the flow resistance associated with the velocity increase is attributed to the decrease of the regenerator channel size, the effective radius should satisfy the condition $r/\delta_\nu < \pi$. With this condition, $1/(1-\chi_\nu)$ in the flow resistance R_ν of the cylindrical pore is approximately written by using r/δ_ν as [13]

$$\frac{1}{1-\chi_\nu} = \frac{4}{3} - i\frac{4}{(r/\delta_\nu)^2}, \tag{3.2}$$

where χ_ν is the thermoacoustic function of the viscous effect, defined by Equation (1.4). Assuming the flow resistance of Equation (2.4) for the stacked screen regenerator with the porosity ϕ, we have

$$R_\nu = -\frac{\omega\rho_{\mathrm{m}}}{A\phi}\mathrm{Im}\left[\frac{1}{1-\chi_\nu}\right], \tag{3.3}$$

where $\mathrm{Im}[\cdots]$ means taking the imaginary part. By inserting Equation (3.2) into the equation above, we obtain the relation between R_ν and the characteristic radius r as

$$\left(\frac{r}{\delta_\nu}\right)^2 = \frac{4\omega\rho_{\mathrm{m}}}{A\phi R_\nu}, \tag{3.4}$$

and therefore,

$$r = 2\delta_\nu\sqrt{\frac{\omega\rho_{\mathrm{m}}}{A\phi R_\nu}}. \tag{3.5}$$

Since the empirical equation of Obayashi et al. reproduces the flow resistance of the stacked-screen regenerator in Chapter 2, the velocity-dependent effective radius r_{eff} can be obtained from Equation (3.5) by replacing R_ν with R_{O}. Namely,

$$r_{\mathrm{eff}} = 2\delta_\nu\left(\frac{0.8\nu}{\omega d_{\mathrm{h}}^2}Re_{\mathrm{h}} + \frac{16\delta_\nu^2}{d_{\mathrm{h}}d_{\mathrm{w}}}\right)^{-\frac{1}{2}}, \tag{3.6}$$

where Equation (3.2) is also used in Equation (3.1). It should be noted that the effective radius r_{eff} of Equation (3.6) changes with Reynolds number $Re_{\mathrm{h}} = |V|\,d_{\mathrm{h}}/\nu$ through the velocity amplitude $|V|$; r_{eff} is a function of Re_{h}. When Re_{h} is negligibly small, r_{eff} reduces to the effective radius of Ueda et al. $r_0 = \sqrt{d_{\mathrm{h}} d_{\mathrm{w}}}/2$ [49], whereas the finite Re_{h} values decrease r_{eff}. Because r_{eff} is derived from the flow resistance of regular cylindrical pores, Equation (3.6) can be seen as an extension of the capacity of the capillary-tube-based modeling. It is valid at least when the regenerator temperature is uniform. Following sections will test the applicability of Equation (3.6) when temperature gradients are imposed on the regenerator.

3.1.2 Use of effective radius

Once the effective radius is established by the capillary-tube-based modeling, a variety of important quantities such as the flow resistance and the thermoacoustic power production, can be predicted using the basic equations of the thermoacoustic theory [72, 60–62]. The equations of momentum and continuity shown in Section 1.1.2 is rewritten for a single cylindrical pore with the cross-sectional area A as [12, 13]

$$\frac{dP}{dx} = -\mathbb{Z}\left(AU\right), \tag{3.7}$$

$$\frac{d\left(AU\right)}{dx} = -\mathbb{Y}P + \mathbb{G}\left(AU\right). \tag{3.8}$$

In Equations (3.7) and (3.8), $\mathbb{Z}$, $\mathbb{Y}$, and $\mathbb{G}$ are respectively given by

$$\mathbb{Z} = i\omega\frac{\rho_{\mathrm{m}}}{A}\frac{1}{1-\chi_\nu}, \tag{3.9}$$

$$\mathbb{Y} = i\omega\frac{A\left[1+(\gamma-1)\,\chi_\alpha\right]}{\gamma P_{\mathrm{m}}}, \text{ and} \tag{3.10}$$

$$\mathbb{G} = \frac{\chi_\alpha - \chi_\nu}{(1-\chi_\nu)\,(1-\sigma)}\frac{1}{T_{\mathrm{m}}}\frac{dT_{\mathrm{m}}}{dx}, \tag{3.11}$$

where P_{m}, T_{m}, γ, and σ respectively denote the mean pressure, the mean temperature, the ratio of specific heats, and the Prandtl number of the working gas. In equations above, χ_α is the thermoacoustic function of the thermal effect. Coefficients $\mathbb{Z}$, $\mathbb{Y}$, and $\mathbb{G}$ are in general dependent on the mean temperature through temperature-dependent gas thermal properties, but it can be seen as constants for a short segment of length Δx. In such a case, the governing equations of Equations (3.7) and (3.8) become coupled ordinary differential equations of P and U with respect to x and can be solved as [62]

$$\begin{pmatrix} P(x+\Delta x) \\ AU(x+\Delta x) \end{pmatrix} = M_{\mathrm{REG}} \begin{pmatrix} P(x) \\ AU(x) \end{pmatrix}, \tag{3.12}$$

where the transfer matrix M_{REG} is presented as

$$M_{\mathrm{REG}} = \exp\left(\frac{\mathbb{G}\Delta x}{2}\right)\begin{bmatrix} -\frac{\mathbb{G}}{\tau}\sinh(\lambda) + \cosh(\lambda) & \frac{2\mathbb{Z}}{\tau}\sinh(\lambda) \\ \frac{2\mathbb{Y}}{\tau}\sinh(\lambda) & \frac{\mathbb{G}}{\tau}\sinh(\lambda) + \cosh(\lambda) \end{bmatrix}, \tag{3.13}$$

with $\tau = \sqrt{\mathbb{G}^2 + 4\mathbb{Y}\mathbb{Z}}$ and $\lambda = \dfrac{\tau\Delta x}{2}$.

When the flow channel is made of a bundle of cylindrical pores with the radius r_{eff} as in the capillary-tube-based modeling, one can rewrite Equations (3.12) and (3.13) by replacing A and U with $A_r = N\pi r_{\mathrm{eff}}^2$, and $V = U/\phi$, respectively, where N denotes the number of tubes. Also, the thermoacoustic functions $\chi_\sharp$ ($\sharp = \alpha, \nu$) should be evaluated by replacing r with the effective radius r_{eff}. By Equation (3.13), the axial evolution of the amplitude and temporal phase of P and U, and therefore the acoustic power, are analytically determined. In the next section, r_{eff} will be compared with the experiments of the stacked-screen regenerators with temperature gradients in order to ascertain the applicability of Equation (3.6).

3.2 Experimental procedure

Experiments in this chapter is based on the experimental apparatus used in Chapter 2. To provide an axial temperature difference on the regenerator, an ambient heat exchanger and a hot heat exchanger were installed on the sides of the regenerator holder, as shown in Figure 3.1. Heat exchangers were fin-and-tube type, and internal fins were made of parallel plates 20 mm in length and 0.5 mm in thickness with the plate spacing $2r_{\mathrm{d}}$ of 1.0 mm. $x = 0.720$ m indicated the place of left side of the ambient heat exchanger, as x_1. Also, the right end of the hot heat exchanger was placed at $x = 0.795$ m, as x_2. The electrical cartridge heater and cooling water pipes were respectively inserted into fins of the hot and ambient heat exchangers. A 50-mm long thermal buffer tube was placed next to the hot heat exchanger. The the ambient heat exchanger and one end of the thermal buffer tube were maintained at room temperature of 293 K. Temperature at both ends of the regenerator were measured by Type-K thermocouples which were located at the circumference and the center of the heat exchangers. Furthermore, temperature discrepancies between the the internal wall and the center of the heat exchanger was less than 20 K when the temperature of center of the hot heat exchanger was increased to 573 K. T_{R} and T_{H} respectively represent as the center temperatures of the ambient heat and hot heat exchangers. Temperature difference ($\Delta T = T_{\mathrm{H}} - T_{\mathrm{R}}$) between the ends of the regenerator was varied from 0 to 250 K on the central axis of the regenerator.

A traveling-wave field with a specific acoustic impedance close to $\rho_m a$ was modulated in the downstream area of the regenerator of $x \geq 0.795$ m, as in the Chapter 2. Two-sensor method was employed to determine the acoustic filed of oscillation pressure $P_\natural = P(x_\natural)$ and the axial acoustic particle velocity $U_\natural = U(x_\natural)$ at $x = x_\natural$ ($\natural = 1, 2$).

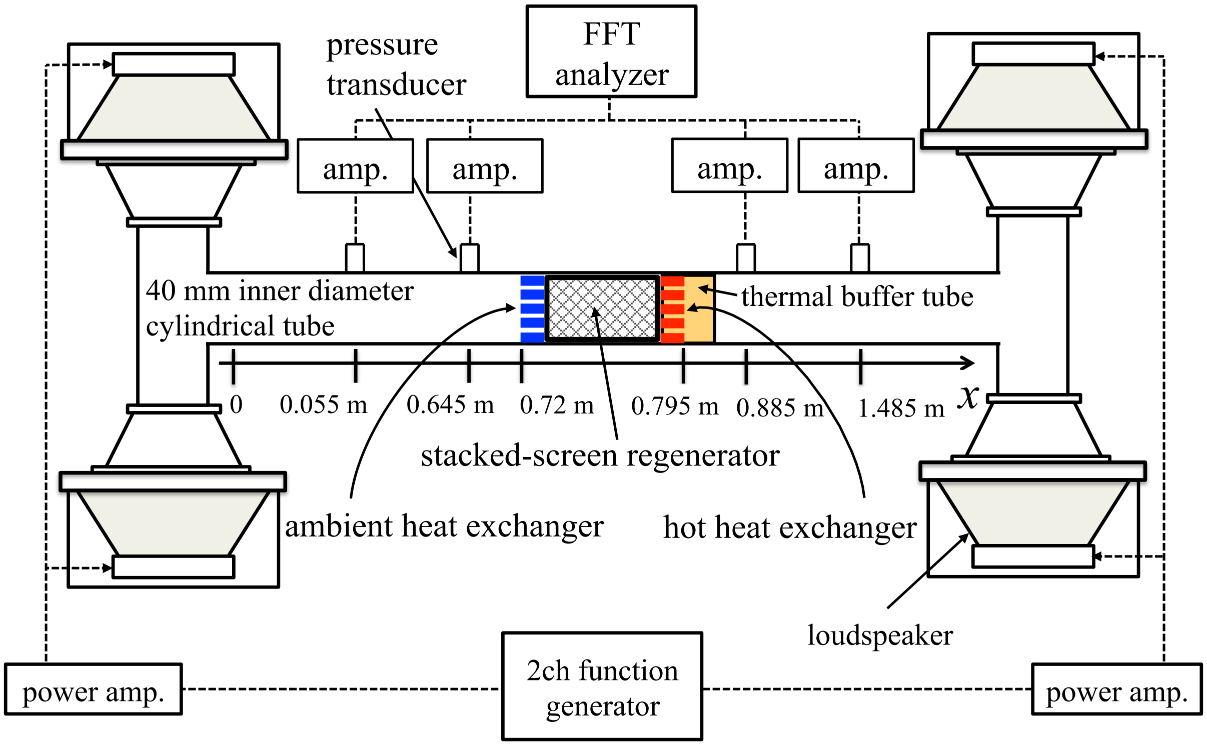
FFT analyzer
pressure transducer
amp.
amp.
amp.
amp.
40 mm inner diameter cylindrical tube
thermal buffer tube
0
0.055 m
0.645 m
0.72 m
0.795 m
0.885 m
1.485 m
x
stacked-screen regenerator
ambient heat exchanger
hot heat exchanger
loudspeaker
power amp.
2ch function generator
power amp.

Figure 3.1: Schematic diagram of the experimental setup. (Figure adapted from Reference 57 and modified by author.)

A typical example of the acoustic field is shown in Figure 3.2, which was obtained with temperature difference $\Delta T = 250$ K. Because of the temperature difference, the acoustic power W increases as it flows down the regenerator. This result is clearly different from Figure 2.6 of Chapter 2, where W is decreased in the regenerator region. The acoustic power difference $\Delta W = W_1 - W_2$ between the regenerator ends was measured with varying the velocity amplitude $|V|$. The results are summarized in Figure 3.3 for the the stacked-screen regenerator of #30 mesh. As can be seen, ΔW is negative when the axial temperature differences ΔT are 0 K and 50 K, but ΔW becomes positive when the axial temperature differences ΔT >100 K. The positive ΔT represents the acoustic power production in the stacked-screen regenerator because of the thermoacoustic energy conversion. In the following sections, the discussion is made on how to predict the acoustic power production in the stacked screen regenerator by using r_{eff}.

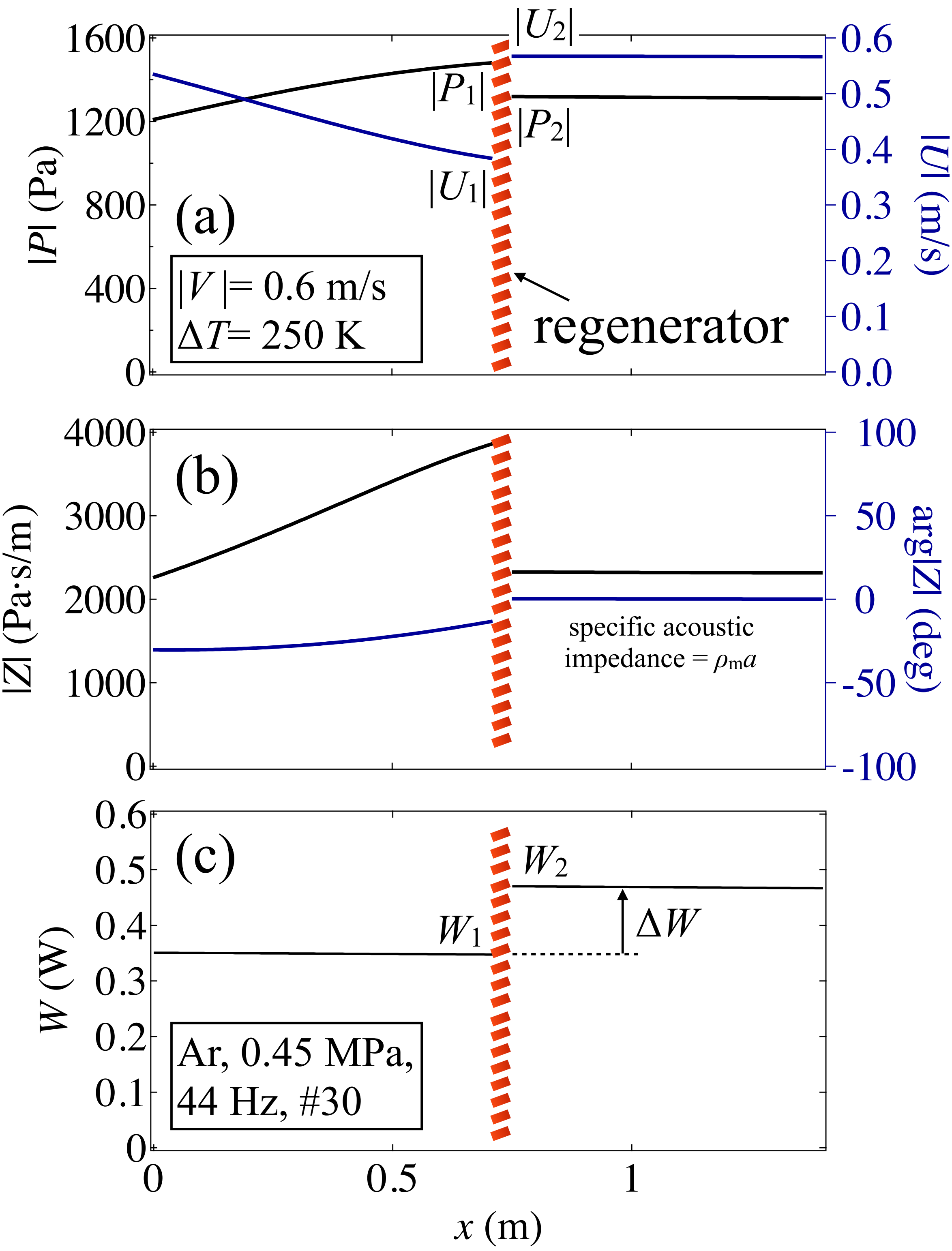

Figure 3.2: Acoustic field obtained with $|V|$ = 0.6 m/s, ΔT = 250 K and oscillation frequency = 44 Hz for Ar with mean pressure of 0.45 MPa. The black and blue curves in (a) represent the pressure amplitude $|P|$ and the amplitude $|U|$ of the cross-sectional averaged velocity, respectively. The black and blue curves in (b) represent the magnitude of acoustic impedance $|Z|$ and its phase $\arg[Z]$, respectively. Also, black lines shown in (c) represent acoustic power distributions in the upstream and downstream of the regenerator, and the thermoacoustic power production is observed between the both ends of the regenerator.

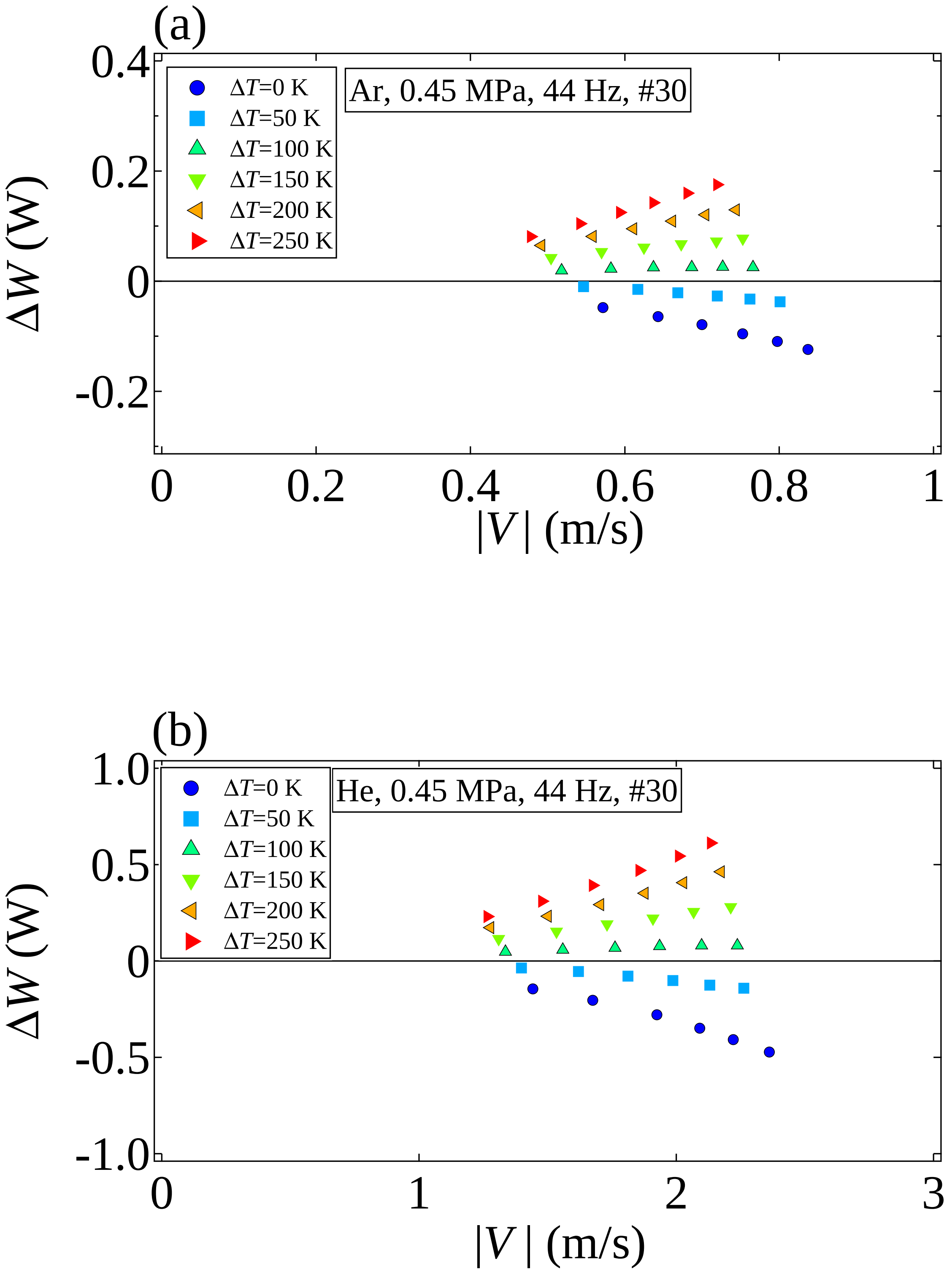

Figure 3.3: Examples of experiments of acoustic power conducting through the regenerator.

3.3 Derivation of experimental effective radius

The effective radius of the stacked-screen regenerator can be determined from the measured P and U, independently of Equation (3.6). Therefore, the effective radius thus determined can be used to judge the applicability of Equation (3.6) in the cases with temperature gradients. The hot heat exchanger, regenerator, and ambient heat exchanger are considered as the regenerator unit as following discussion. The derivation of experimental effective radius is given as follows.

The stacked-screen regenerator is assumed as a bundle of cylindrical tubes with an unknown radius r. So, acoustic fields of oscillation pressure and volume velocity at both sides of the regenerator unit is related as

$$\begin{pmatrix} P_2 \\ AU_2 \end{pmatrix} = M_\mathrm{H} M_\mathrm{REG} M_\mathrm{R} \begin{pmatrix} P_1 \\ AU_1 \end{pmatrix}, \tag{3.14}$$

where M_R, M_REG, and M_H respectively represent the transfer matrices of the ambient heat exchanger, regenerator, and hot heat exchanger. the interface losses, caused by the abrupt change in the cross section, at the boundary between the regenerator and heat exchangers are ignored. M_R, M_REG, and M_H are formulated by the thermoacoustic governing equations, as described in Section 3.1.2. The transfer matrix of the regenerator was divided into 100 segments for taking into account the temperature dependence of the thermal properties of the gas with a linear temperature distribution in the regenerator region. Therefore, the transfer matrix of the regenerator M_REG was represented by a product of the matrices $M_{\mathrm{REG},\dagger}$ ($\dagger = 1, 2, ..., 100$), where $M_{\mathrm{REG},\dagger}$ stands for the transfer matrix of the $\dagger$-th segment determined by the thermal properties of the gas with the local temperature. Preliminary calculation confirmed that the results were unchanged when the number of divisions were increased more than 100. Also, Uniform temperatures (T_R or T_H) were assumed in heat exchangers. As a result of $\mathbb{G} = 0$ in Equation (3.13), $M_{\mathrm{R\,or\,H}}$ is expressed as

$$M_{\mathrm{R\,or\,H}} = \begin{bmatrix} \cosh\left(\grave{\lambda}\right) & \sqrt{\dfrac{\mathbb{Z}}{\mathbb{Y}}}\sinh\left(\grave{\lambda}\right) \\ \sqrt{\dfrac{\mathbb{Y}}{\mathbb{Z}}}\sinh\left(\grave{\lambda}\right) & \cosh\left(\grave{\lambda}\right) \end{bmatrix}, \tag{3.15}$$

where $\grave{\lambda} = l_\mathrm{HE}\sqrt{\mathbb{YZ}}$, and l_HE is the length of the heat exchanger. Due to the heat exchangers consist of parallel plates, the thermoacoustic function $\chi_\sharp$ ($\sharp = \nu, \alpha$) is evaluated using the plate distance $2r_\mathrm{d}$ as [12, 13]

$$\chi_\sharp = \frac{\tanh\left[(1+i)\dfrac{r_\mathrm{d}}{\delta_\sharp}\right]}{(1+i)\dfrac{r_\mathrm{d}}{\delta_\sharp}}. \tag{3.16}$$

By substituting experimental values of P_1 and U_1 into the left side of the Equation (3.14), P_2 and U_2 can be analytically obtained as

$$\begin{pmatrix} P_{2,\mathrm{cal}} \\ AU_{2,\mathrm{cal}} \end{pmatrix} = M_{\mathrm{H}} M_{\mathrm{REG}}(r) M_{\mathrm{R}} \begin{pmatrix} P_{1,\mathrm{exp}} \\ AU_{1,\mathrm{exp}} \end{pmatrix}, \tag{3.17}$$

where the subscripts cal and exp respectively stand for the calculated and experimental values. In the equation, the transfer matrix M_{REG} is represented as $M_{\mathrm{REG}}(r)$ to emphasize that M_{REG} is a function of radius r of the regenerator. When the characteristic pore radius r of a regular flow channel regenerator is known for determining $M_{\mathrm{REG}}(r)$, measured acoustic field of $P_{2,\mathrm{exp}}$ and $U_{2,\mathrm{exp}}$ must be agreed with calculation of $P_{2,\mathrm{cal}}$ and $U_{2,\mathrm{cal}}$. If a stacked-screen regenerator indeed has a characteristic pore size r_{eff}, the acoustic field difference between calculation and experiment would be minimized when $r = r_{\mathrm{eff}}$. Likewise, the inverse of the transfer matrices of Equation (3.14) also yields $P_{1,\mathrm{cal}}$ and $U_{1,\mathrm{cal}}$ from experimental values of $P_{2,\mathrm{exp}}$ and $U_{2,\mathrm{exp}}$, as shown below.

$$\begin{pmatrix} P_{1,\mathrm{cal}} \\ AU_{1,\mathrm{cal}} \end{pmatrix} = \left[M_{\mathrm{H}} M_{\mathrm{REG}}(r) M_{\mathrm{R}} \right]^{-1} \begin{pmatrix} P_{2,\mathrm{exp}} \\ AU_{2,\mathrm{exp}} \end{pmatrix} \tag{3.18}$$

Obtained $P_{1,\mathrm{cal}}$ and $U_{1,\mathrm{cal}}$ are also compared with $P_{1,\mathrm{exp}}$ and $U_{1,\mathrm{exp}}$ for verification. If a stacked-screen regenerator is indeed characterized with the effective radius r_{eff} obtained by the cylindrical tube modeling of Equation (3.6), the difference between calculation and experiment would become zero or minimized when the value of r is set to the effective radius r_{eff}.

The acoustic powers between calculations of $W_{\natural,\mathrm{cal}}$ and experiments of $W_{\natural,\mathrm{exp}}$ ($\natural = 1, 2$) at both sides of the regenerator unit are employed to determine the value of r that minimizes the difference between the calculation and experiments; $W_{\natural,\mathrm{exp}}$ is the acoustic power obtained by $P_{\natural,\mathrm{exp}}$ and $U_{\natural,\mathrm{exp}}$, whereas $W_{\natural,\mathrm{cal}}$ denotes that derived using $P_{\natural,\mathrm{cal}}$ and $U_{\natural,\mathrm{cal}}$ in Equations (3.17) and (3.18). The relative error $\varepsilon_\natural$ between $W_{\natural,\mathrm{exp}}$ and $W_{\natural,\mathrm{cal}}$ is given as

$$\varepsilon_\natural = \frac{W_{\natural,\mathrm{cal}} - W_{\natural,\mathrm{exp}}}{W_{\natural,\mathrm{exp}}}. \tag{3.19}$$

The average error ε is thus calculated as

$$\varepsilon = \frac{|\varepsilon_1| + |\varepsilon_2|}{2}. \tag{3.20}$$

Various values of r are calculated for plotting ε vs r, as shown in Figure 3.4. As can be seen, Figure 3.4 presents a minimum ε. The corresponding radius was thus selected as the experimental effective radius $r_{\mathrm{eff,exp}}$. In this case, the effective radius is obtained as $r_{\mathrm{eff,exp}} = 167$ μm, which gives a minimum ε of 0.1%. Throughout this chapter, the minimum ε, though it tended to increase with ΔT, was always determined less than 6%.

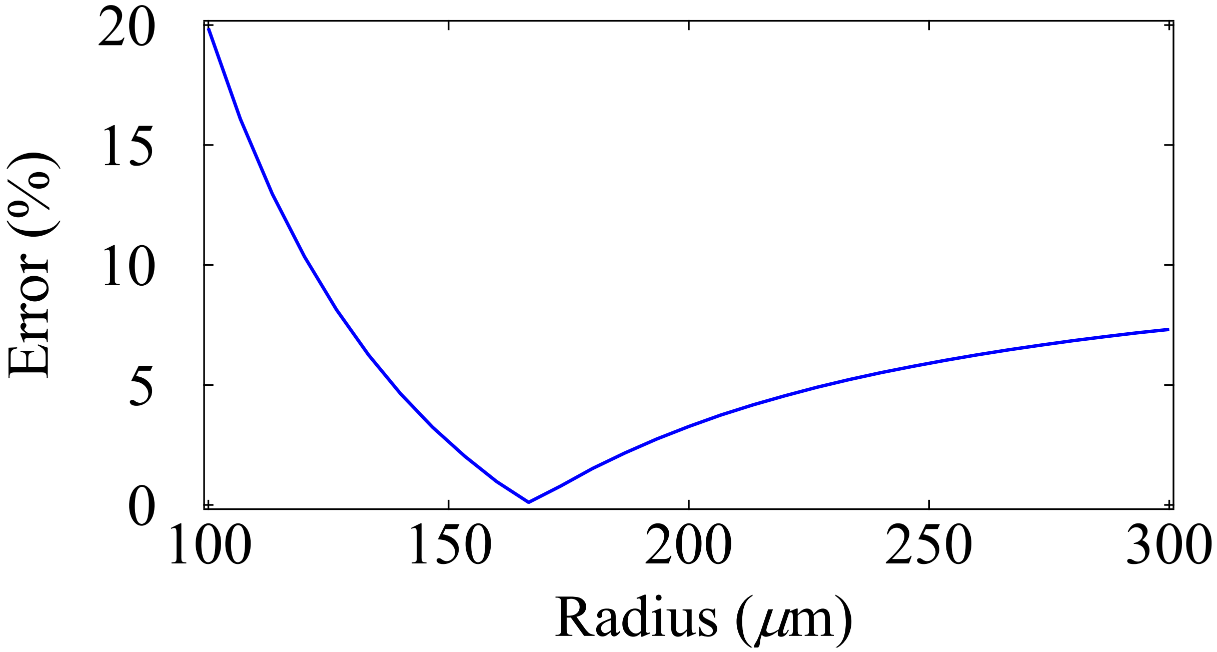

Figure 3.4: Error ε vs the radius r for the stacked-screen regenerator when the working gas is Ar. The oscillating frequency is 44.0 Hz. The mesh number is 30. The temperature difference is 100 K and $|V| = 0.427$ m/s. (Figure adapted from Reference 57 and modified by author.)

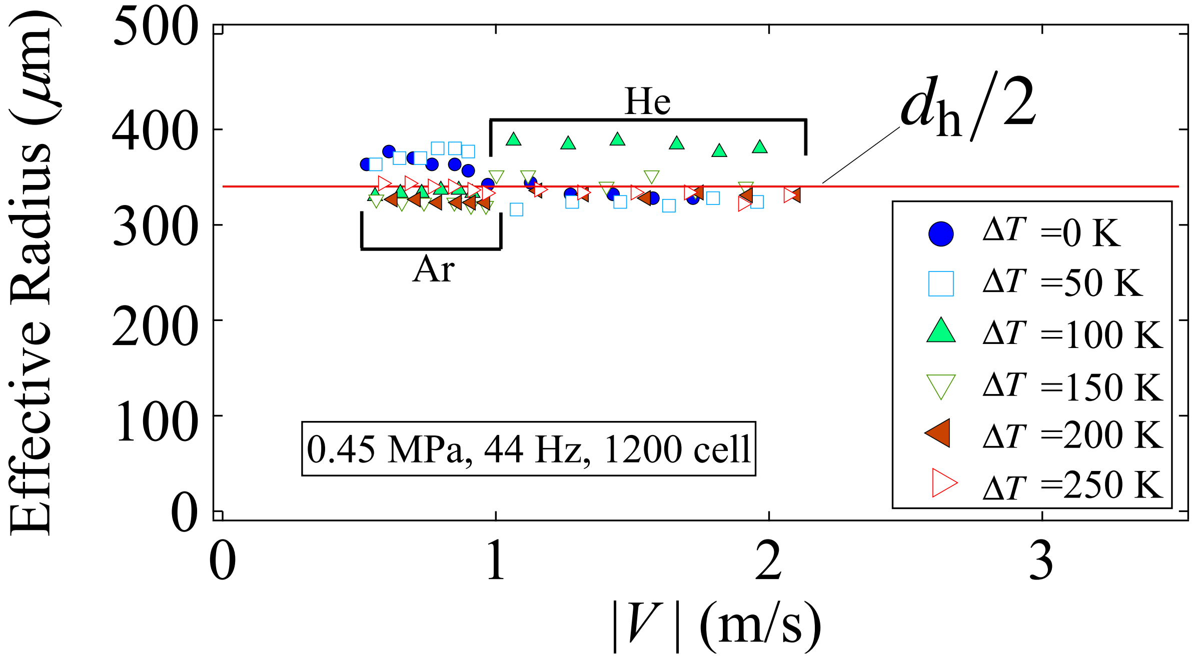

Figure 3.5: Comparison of the experimental effective radius $r_{\mathrm{eff,exp}}$ and the actual flow channel size of the ceramic honeycomb. Experimental results are shown by symbols. The horizontal line represents one-half of the hydraulic diameter (= 340 μm). (Figure adapted from Reference 57 and modified by author.)

In the case of regular pore regenerator of the ceramic honeycomb, Figure 3.5 shows the effective radius $r_{\mathrm{eff,exp}}$ vs $|V|$. The temperature difference ΔT was changed from 0 to 250 K with every 50 K, and the working gases were either He or Ar. In Figure 3.5, the horizontal line represents one-half of the actual hydraulic diameter ($d_{\mathrm{h}}/2 = 340\ \mu\mathrm{m}$). Comparisons between $r_{\mathrm{eff,exp}}$ and the line shows the maximum deviation of 18%, which guarantees the validity of the method. The following section will discuss the case of stacked-screen regenerator and the proposed effective radius r_{eff} of Equation (3.6) by comparisons between experiments and predictions using various mesh numbers of woven screens.

3.4 Comparisons of effective radii

Figures 3.6(a)-3.6(d) and Figures 3.7(a)-3.7(d) summarize the experimental effective radii $r_{\mathrm{eff,exp}}$ respectively for Ar and He tested with the oscillation frequency of 44.0 Hz. The temperature difference ΔT across the stacked-screen regenerator was varied from 0 to 250 K with every 50 K. The average of four measurements is expressed by the symbol, while the size of the error bar denotes standard deviations of $r_{\mathrm{eff,exp}}$. Curves shown in Figures 3.6 and 3.7 are predictions of effective radius r_{eff} obtained using Equation (3.6), which were determined with the physical properties of the working gas at the average temperature between T_{H} and T_{R}. Figures 3.6 and 3.7 express that both effective radii of experiments and predictions decrease with $|V|$ and ΔT. The maximum discrepancies between experiments $r_{\mathrm{eff,exp}}$ and predictions of r_{eff}, in Figures 3.6 and 3.7, are respectively 13% and 7% for Ar and He. Maximum deviations of respective mesh numbers are summarized in Table 3.1. Thus, experimental results prove that r_{eff} of Equation (3.6) based on the empirical equation of Obayashi et al. proposed from uniform temperature experiments is able to predict the acoustic fields when the temperature difference existed in the stacked-screen regenerator.

Table 3.1: Maximum deviations between predictions and experiments of r_{eff} in the case of 44 Hz.

working gas	oscillation frequency	#30	#50	#60	#100
		error ε (%)			
Ar	44 Hz	7	12	13	3
He		5	9	7	5

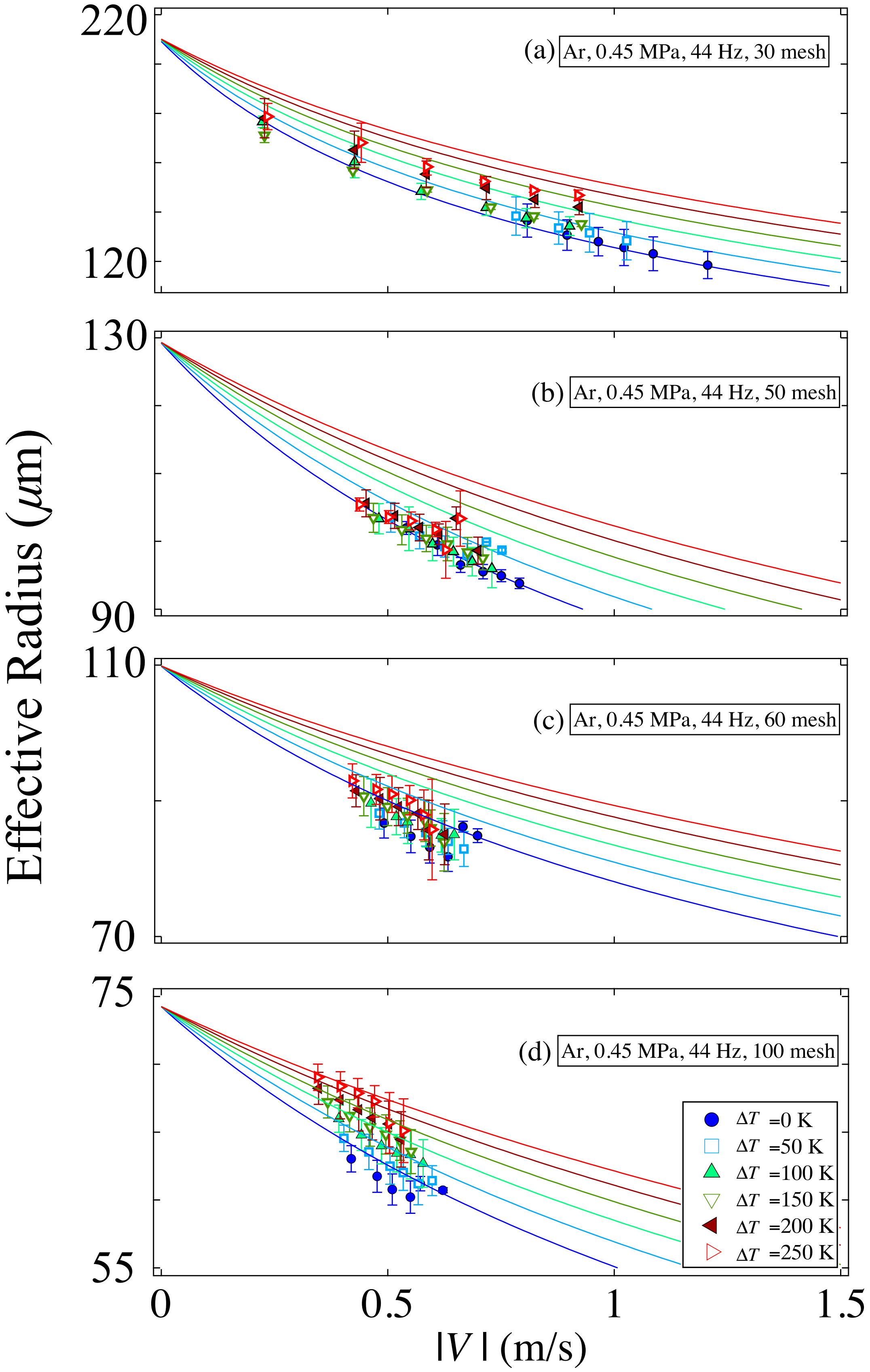

Figure 3.6: Comparison between the experimental effective radius $r_{\mathrm{eff,exp}}$ with error bars and the predicted r_{eff} obtained using the empirical equation of Obayashi et al. for stacked-screen regenerators, where (a)–(d) show the results for Ar. Experimental results are shown by symbols with error bars; predicted values are shown by curves. (Figures adapted from Reference 57 and modified by author.)

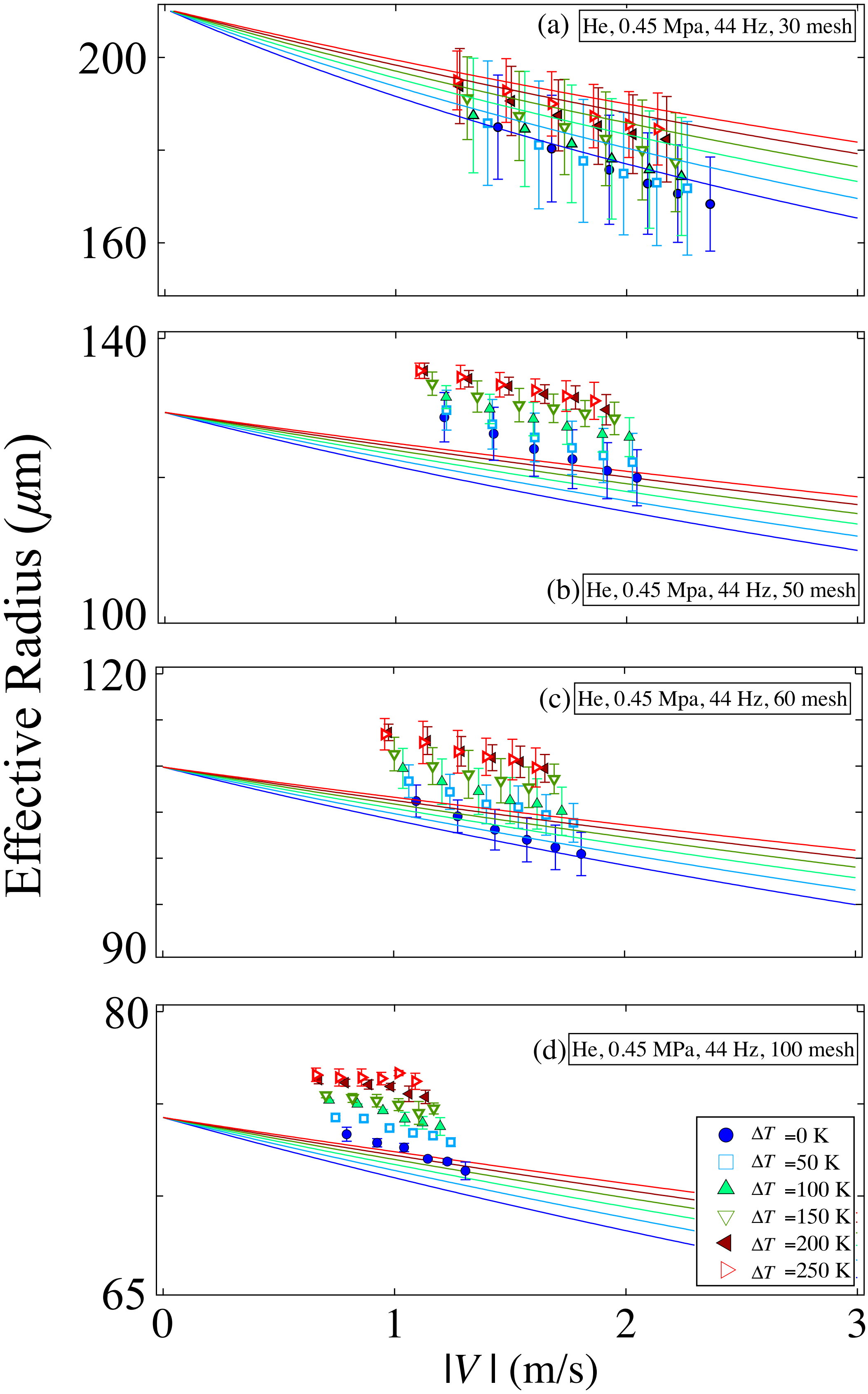

Figure 3.7: Comparison between the experimental effective radius $r_{\mathrm{eff,exp}}$ with error bars and the predicted r_{eff} obtained using the empirical equation of Obayashi et al. for stacked-screen regenerators, where (a)–(d) show the results for He. Experimental results are shown by symbols with error bars; predicted values are shown by curves. (Figures adapted from Reference 57 and modified by author.)

Table 3.2: Maximum deviations between predictions and experiments of r_{eff} in cases of 20.0 and 100 Hz.

#100		
oscillation frequency	Ar	He
	error ε (%)	
20 Hz	7	6
100 Hz	5	5

The applicability of r_{eff} of Equation (3.6) is further tested in oscillation frequencies of 20.0 and 100 Hz using #100 mesh screens. Figures 3.8 and 3.9 compare the effective radius r_{eff} with experimental value $r_{\mathrm{eff,exp}}$ respectively for Ar and He. Also, panels (a) and (b) respectively show cases of frequencies of 20.0 and 100 Hz. From the experimental results of 20-100 Hz, it is found that frequency dependence is not significant in the case #100 mesh screens. For instance, focusing on $|V| = 0.5$ m/s in Ar gas, the range of the effective radii in the case of 44.0 Hz is over $62 < r_{\mathrm{eff,exp}}$ (μm) < 68, which is similar to $62 < r_{\mathrm{eff,exp}}$ (μm) < 68 at 20.0 Hz, and over $68 < r_{\mathrm{eff,exp}}$ (μm) < 72 at 100 Hz. Absence of the frequency dependence in both cases of experiments and predictions using #100 mesh screens is already described in Chapter 2. The effective radius obtained using the empirical equation of Obayashi et al., also presents the same tendency. Consequently, the maximum discrepancies shown in Figures 3.8 and 3.9 are respectively 7 and 5% for Ar and He. The detail deviations are listed in Table 3.2. Based upon experimental evidences, r_{eff} of Equation (3.6) is applicable for the frequency range from 20.0 to 100 Hz.

As can be seen in Figures 3.6–3.9, the velocity-independent part of the effective radius r_{eff} of Equation (3.6) diminishes when $|V| \to 0$. The extrapolation of the experimental radius plotted by symbols coincide with r_{eff} of Equation (3.6) in the limit of zero velocity, which verifies the applicability of the effective radius r_0 of Ueda et al. for the stacked-screen regenerator with temperature gradients as long as the velocity is small. On the other hand, use of r_{eff} would be more suited for the prediction of thermoacoustic Stirling engine performance with nonzero velocity amplitude. Therefore, the design methods based on r_0 [72, 60–62] would be improved by replacing r_0 with r_{eff}.

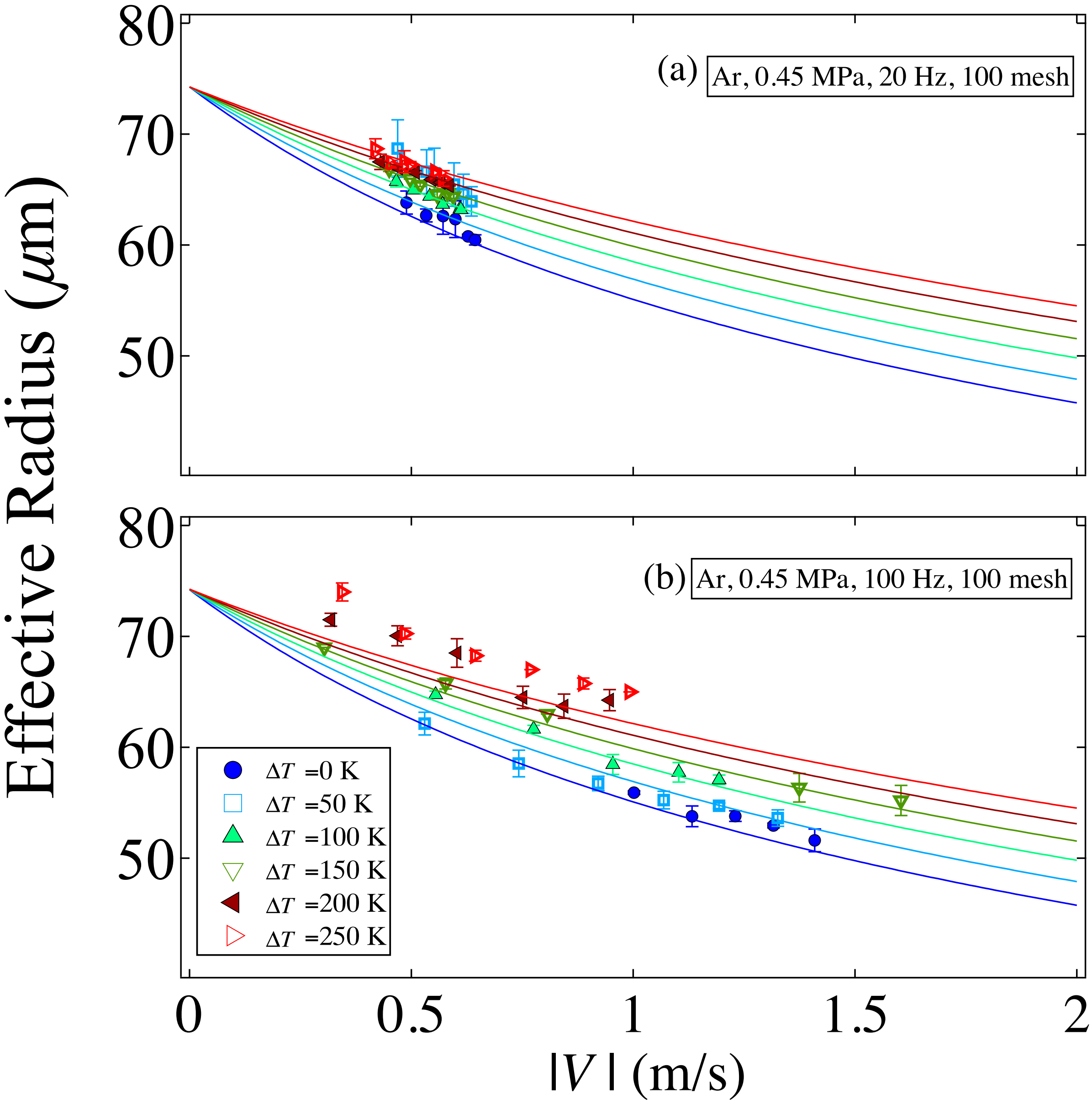

Figure 3.8: Comparison between the experimental effective radius $r_{\text{eff, exp}}$ of #100 mesh screens with error bars and predicted r_{eff} obtained using the empirical equation of Obayashi et al. at oscillation frequencies of 20 and 100 Hz, in (a) and (b), respectively, for Ar. Experimental results are shown by symbols with error bars. Predictions are shown by the curves. (Figures adapted from Reference 57 and modified by author.)

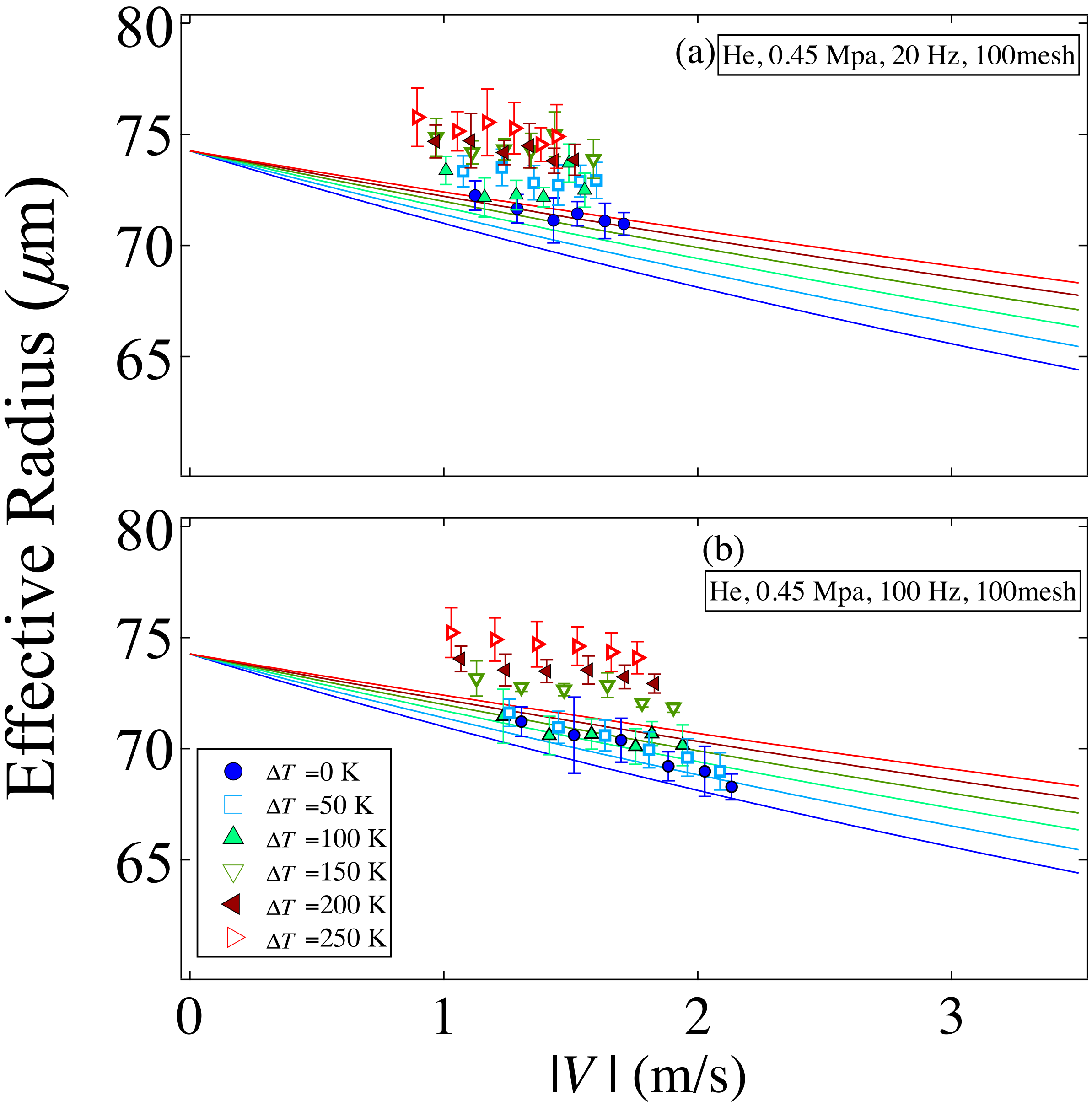

Figure 3.9: Comparison between the experimental effective radius $r_{\text{eff, exp}}$ of #100 mesh screens with error bars and predicted r_{eff} obtained using the empirical equation of Obayashi et al. at oscillation frequencies of 20 and 100 Hz, in (a) and (b), respectively, for He. Experimental results are shown by symbols with error bars. Predictions are shown by curves. (Figures adapted from Reference 57 and modified by author.)

3.5 Conclusions

Based on the cylindrical-tube-modeling, the flow resistance empirical equation of Obyayashi et al. of Equation (3.1) was converted to a form of the effective radius r_{eff} of Equation (3.6) which was parameterized with Re_{h} and r_0/δ_ν. To ascertain the applicability of the effective radius r_{eff}, the stacked-screen regenerators were tested in the presence of the axial temperature differences from 0 K to 250 K. The results demonstrated good agreements between predictions and experiments of r_{eff}, which means that the effective radius r_{eff} is capable of estimating the thermoacoustic engine performance such as the acoustic power production, even the stacked-screen regenerator is employed.

Chapter 4

Measurement of heat flow transmitted through regenerators

4.1 Introduction

When the gas oscillates in a channel with maintaining thermal contacts with the channel wall, the gas entropy oscillates with time through the heat exchange with the wall. When the entropy oscillations of the gas are combined with the displacement oscillations of the gas, it becomes possible that the entropy goes up at the maximum displacement, while the entropy goes down at the minimum displacement. The resulting bucket brigade of entropy causes the macroscopic heat transport along the channel. In a regenerator of mechanical Stirling engines and thermoacoustic engines, the acoustically induced heat flow Q is generated in such a way, and it goes from hot to cold. The heat flow Q is responsible for the thermal loss, and hence it should be minimized for a better engine performance. Although the thermoacoustic theory explains the mechanism of the heat flow Q in a regular flow channel, it is not directly applicable to the stacked-screen regenerators. Therefore, the researchers have challenged the problems of the heat flow in the regenerators of Stirling engines and thermoacoustic engines from the experimental point of view.

Recently, the cylindrical tube modeling with the effective radius r_0 of Ueda et al. was applied for characterizing the acoustic heat flow Q. Hasegawa et al. [63] measured experimentally Q with different frequencies but with a fixed oscillatory velocity amplitude (= 2 m/s) in the air at atmospheric pressure. The agreements between the estimation based on the model and the experimental results were satisfactory, but the further applicability of r_0 is should be tested with varying the velocity amplitude. By assuming that the friction factor and heat transfer coefficient obtained from the steady-flow plots of Kays and London [26] are applicable to the gas harmonically oscillating with time, Swift and Ward [37] provided a set of equations for characterizing the stacked-screen regenerator. The equation of the temperature oscillation were applied to estimate the heat transfer properties of the regenerator. Although these equations are already used in the thermoacoustic calculation code—Design Environment for Low-amplitude Thermoacoustic Energy Conversion (DeltaEC) [38], they are based on steady-flow data. So the applicability is questionable in the real thermoacoustic engines oscillating with a few hundred hertz at the most. In a practical Stirling engine design, several empirical equations have been used for heat transfer processes between the flowing gas and solid wall of the stacked-screen regenerator, which are only parameterized by non-dimensional Nusselt number Nu. The effect of the oscillation frequency must be taken into consideration.

This chapter attempts to experimentally clarify the velocity and frequency dependences of the axial heat flow introduced by gas oscillations in the stacked-screen regenerator, which is compared with the representative empirical equations, to ascertain their applicability.

4.2 Axial heat flow estimated by empirical equations

Consider axial gas oscillations with angular frequency ω in a flow channel. The thermoacoustic theory [12–14] gives the time-averaged heat flow as a result of hydrodynamic transport of entropy by

$$Q = \frac{1}{2}\rho_{\mathrm{m}} T_{\mathrm{m}} \int \mathrm{Re}\left[s\widetilde{\mathcal{U}}\right] dA, \tag{4.1}$$

where s and $\mathcal{U}$ denote complex amplitudes of entropy and velocity oscillations, and ρ_{m} and T_{m}, respectively, represent the temporal mean density and temperature. In the equation, $\mathrm{Re}\,[\cdots]$ and $\widetilde{\cdots}$, respectively, stand for the real part and conjugate of a complex number. Also, the surface integration $\int \cdots dA$ is done over the cross-sectional area of the flow channel. It should be noticed that, in the equation above, the axial velocity oscillations $\mathcal{U}$ of the gas in pipe is functions of r and x with $\mathcal{U} = \mathcal{U}\,(r, x)$ whose cross-sectional average is as $\langle \mathcal{U}(r, x)\rangle = U(x)$, where $\langle \cdots \rangle$ denotes the cross-sectional average. The complex amplitude s in Equation (4.1) is represented by complex amplitudes P and $\mathcal{T}$ of the gas pressure and temperature as

$$s = -\frac{\beta}{\rho_{\mathrm{m}}} P + \frac{c_{\mathrm{p}}}{T_{\mathrm{m}}} \mathcal{T}, \tag{4.2}$$

where β stands for the coefficient of thermal expansion and c_{p} signifies the isobaric heat capacity per unit mass. The complex amplitude $\mathcal{T}$ of temperature oscillations is also functions of r and x with $\mathcal{T} = \mathcal{T}\,(r, x)$. As like velocity oscillations, the cross-sectional average of temperature oscillations is expressed as $\langle \mathcal{T}\,(r, x)\rangle = T(x)$. By carefully taking the cross-sectional average of the right-hand side of Equation (4.1), the heat flow is obtained with an ideal gas assumption as

$$Q = Q_{\mathrm{A}} + Q_{\mathrm{D}}, \tag{4.3}$$

where Q_{A} and Q_{D} are respectively the compression- and advection-driven heat flows [65]. Here, we aim to estimate the het flow transmitting through a regenerator having numerous tiny flow channels. For such a regenerator installed in a wide pipe as illustrated in Figure 2.5, cross-sectional-averaged oscillation velocities U and V respectively in the pipe and regenerator regions are related to each other by $AU = A\phi V$, where ϕ is the volume porosity of the regenerator and A is the cross-sectional area of the wide pipe. For the heat flow transmitting through the regenerator, Q_{A} is given as

$$Q_{\mathrm{A}} = -\frac{1}{2} A \mathrm{Re}\left[g P \widetilde{V}\right] \quad \text{with} \quad g = \frac{\chi_\alpha - \widetilde{\chi_\nu}}{(1+\sigma)\left(1-\widetilde{\chi_\nu}\right)}, \tag{4.4}$$

and Q_{D} is expressed as

$$Q_{\mathrm{D}} = \frac{1}{2} A \frac{\rho_{\mathrm{m}} c_{\mathrm{p}}}{\omega} \mathrm{Im}\left[g_{\mathrm{D}}\right] \frac{dT_{\mathrm{m}}}{dx} |V|^2 \quad \text{with} \quad g_{\mathrm{D}} = \frac{\chi_\alpha + \sigma \widetilde{\chi_\nu}}{\left(1-\sigma^2\right)\left|1-\chi_\nu\right|^2}, \tag{4.5}$$

where σ represents the Prandtl number of the gas. Also, $|\cdots|$ and $\mathrm{Im}\,[\cdots]$ signify taking the absolute value and imaginary part of a complex number. The heat flow is therefore obtainable if P and V are determined by experiments, because other quantities are specified by the experimental conditions.

In the following section, the applicability of effective radius of Ueda et al. $r_0 = \sqrt{d_{\mathrm{h}} d_{\mathrm{w}}}/2$ will be tested using the equation above by comparing with the measured value.

By the simple harmonic analysis using the heat transfer coefficient of the steady flow, Swift and Ward [37] derived their cross-sectional-averaged oscillation complex amplitude T_{S} of temperature in the stacked-screen regenerator, which is given as

$$T_{\mathrm{S}} = \frac{\beta T_{\mathrm{m}}}{\rho_{\mathrm{m}} c_{\mathrm{p}}} Y_{\mathrm{S}} P - \frac{1}{i\omega} \frac{dT_{\mathrm{m}}}{dx} G_{\mathrm{S}} V, \tag{4.6}$$

with

$$\begin{aligned} & Y_{\mathrm{S}} = \frac{\varepsilon_{\mathrm{s}} + (g_c + e^{2i\theta_P} g_v)\varepsilon_{\mathrm{h}}}{1 + \varepsilon_{\mathrm{s}} + (g_c + e^{2i\theta_T} g_v)\varepsilon_{\mathrm{h}}}, \; G_{\mathrm{S}} = \frac{\varepsilon_{\mathrm{s}} + (g_c - g_v)\varepsilon_{\mathrm{h}}}{1 + \varepsilon_{\mathrm{s}} + (g_c + e^{2i\theta_T} g_v)\varepsilon_{\mathrm{h}}}, \\ & \varepsilon_{\mathrm{s}} = \frac{\phi \rho_{\mathrm{m}} c_{\mathrm{p}}}{(1-\phi)\rho_{\mathrm{s}} c_{\mathrm{s}}}, \; \varepsilon_{\mathrm{h}} = \frac{i}{2b\sigma^{1/3}} \left(\frac{d_{\mathrm{h}}}{\delta_\alpha}\right)^2, \\ & b = 3.81 - 11.29\phi + 9.47\phi^2, \\ & \theta_P = \mathrm{phase}\,[V] - \mathrm{phase}\,[P], \; \theta_T = \mathrm{phase}\,[V] - \mathrm{phase}\,[T], \\ & g_c = \frac{2}{\pi} \int_0^{\pi/2} \frac{dz}{1 + Re_{\mathrm{h}}^{3/5} \cos^{3/5}(z)}, \text{ and } g_v = -\frac{2}{\pi} \int_0^{\pi/2} \frac{\cos 2z dz}{1 + Re_{\mathrm{h}}^{3/5} \cos^{3/5}(z)}, \end{aligned} \tag{4.7}$$

where both the density ρ_{s} and heat capacity c_{s} of the channel walls are assumed to be much larger than those of the gas; Re_{h} stands for the Reynolds number given as $Re_{\mathrm{h}} = |V|\, d_{\mathrm{h}}/\nu$ ($|V|$ represents the magnitude of the complex velocity V). The equation above is based on an assumption of

$$\langle \text{temperature oscillation} \rangle = \frac{\langle \text{velocity oscillation} \times \text{temperature oscillation} \rangle}{\langle \text{velocity oscillation} \rangle}. \tag{4.8}$$

Under the same assumption, the heat flow in Equation (4.1) for the case of the stacked-screen regenerator is given for an ideal gas as

$$Q \approx \frac{1}{2} A \rho_\mathrm{m} T_\mathrm{m} \mathrm{Re}\left[\langle s \rangle \widetilde{V}\right], \tag{4.9}$$

with

$$\langle s \rangle = -\frac{1}{\rho_\mathrm{m} T_\mathrm{m}} P + \frac{c_\mathrm{p}}{T_\mathrm{m}} T_\mathrm{S}. \tag{4.10}$$

The heat flow Q given by Equation (4.9) will also be compared with the value obtained from experimentation.

Tanaka et al. and Gedeon & Wood proposed the Nusselt number Nu from experiments in oscillatory flows of the frequency range of the mechanical Stirling engine. Tanaka et al. determined the Nusselt number from measurements conducted with a maximum oscillation frequency of 10 Hz [32], which is written as

$$Nu_\mathrm{T} = 0.33 {Re_\mathrm{h}}^{0.67}. \tag{4.11}$$

Gedeon and Wood also obtained their Nu-Re_h correlation equation [33] from measurements with oscillation frequency up to 120 Hz. Stirling machine design software code—Sage [65] incorporated the empirical correlation. It is expressed as

$$Nu_\mathrm{G} = \left(1 + 0.99 \left(Re_\mathrm{h} \sigma\right)^{0.66}\right) \phi^{1.79}. \tag{4.12}$$

The applicability of these empirical equations for the Stirling engines should be tested. However, incorporating them into the thermoacoustic theory is a difficult problem for several reasons [37]. Therefore, as a tentative method, the complex oscillation temperature T using the Nusselt number is determined by

$$T_{Nu} = \left(\rho_\mathrm{m} c_\mathrm{p} + \frac{16}{i\omega} \frac{kNu}{d_\mathrm{h}^2}\right)^{-1} P - \left(i\omega + \frac{16}{\rho_\mathrm{m} c_\mathrm{p}} \frac{kNu}{d_\mathrm{h}^2}\right)^{-1} \frac{dT_\mathrm{m}}{dx} V, \tag{4.13}$$

which was obtained by introducing complex notation for T and by replacing the heat transfer coefficient h with $h = 4kNu/d_\mathrm{h}$ while using thermal conductivity k of the gas into Equation (27) of Reference 37. Substituting T_{Nu} into Equation (4.10) and then using Equation (4.9) yield the heat flow based on Nusselt number correlations.

4.3 Experimental procedure

A stainless steel cylindrical tube with a radius of 20 mm was installed with a 35-mm-long regenerator and two 20-mm-long heat exchangers. Two acoustic driver pairs made of four loudspeakers was connected to the tube ends, as schematically illustrated in Figure 4.1. The working gas used in this chapter was argon gas with the mean pressure of 0.45 MPa. Two regenerator types were tested: randomly stacked stainless-steel woven wire mesh screens (with mesh number of #20, #30, #50, #60, and #80) and a cylindrical ceramic honeycomb catalyst of 1200 cell. The detailed geometrical parameters of regenerators used in this chapter are presented in Table 4.1. Three electrical heater rods were used to heat the hot heat exchanger, and the cooling water at 293 K were circulated to maintain the ambient heat exchanger temperature T_R. Type-K thermocouples were placed on the central axis and at the regenerator ends for measuring temperatures T_H of the hot heat exchanger and T_R of the ambient heat exchanger, from which the axial temperature difference $\Delta T = T_\mathrm{H} - T_\mathrm{R}$ across the regenerator was determined. Also, one end of a 50-mm-long thermal buffer tube on the side of the hot heat exchanger was maintained at room temperature by cooling water.

Table 4.1: Geometrical properties of regenerators.

Stacked-screen regenerator

Mesh number	Wire diameter (mm) d_w	Hydraulic diameter (mm) d_h	Volume porosity ϕ
#20	0.2	1.30	0.87
#30	0.22	0.80	0.78
#50	0.14	0.47	0.77
#60	0.12	0.40	0.77
#80	0.12	0.28	0.70

Ceramic honeycomb catalyst

Cell number		Hydraulic diameter (mm) d_h	Volume porosity ϕ
1200		0.68	0.89

In order to measure the oscillation-induced heat flow, the experiment was performed as follows. First, the necessary heat power for establishing a steady non-oscillating state with ΔT=250 K was recorded, in the absence of acoustic oscillations, as Q_OFF. The amount of heat power Q_OFF was turned out to be 75 ± 4 W, for a variety of the mesh numbers and the surrounding temperatures. Secondly, in the presence of acoustic oscillations excited by two acoustic drivers at ends, the heat power Q_ON was carefully adjusted by voltage and current of the cartridge electrical heater, so that the same ΔT=250 K was maintained. Finally, the rate of heat flow passing through the regenerator was determined as

$$|Q| = Q_\mathrm{ON} - Q_\mathrm{OFF}. \tag{4.14}$$

Experiments were repeated four times for each of experimental conditions, and the mean value and the standard deviation of $|Q|$ were employed as the experimental results of this chapter. It should be noted that the absolute value of the heat flow rate $|Q|$ was intentionally used in

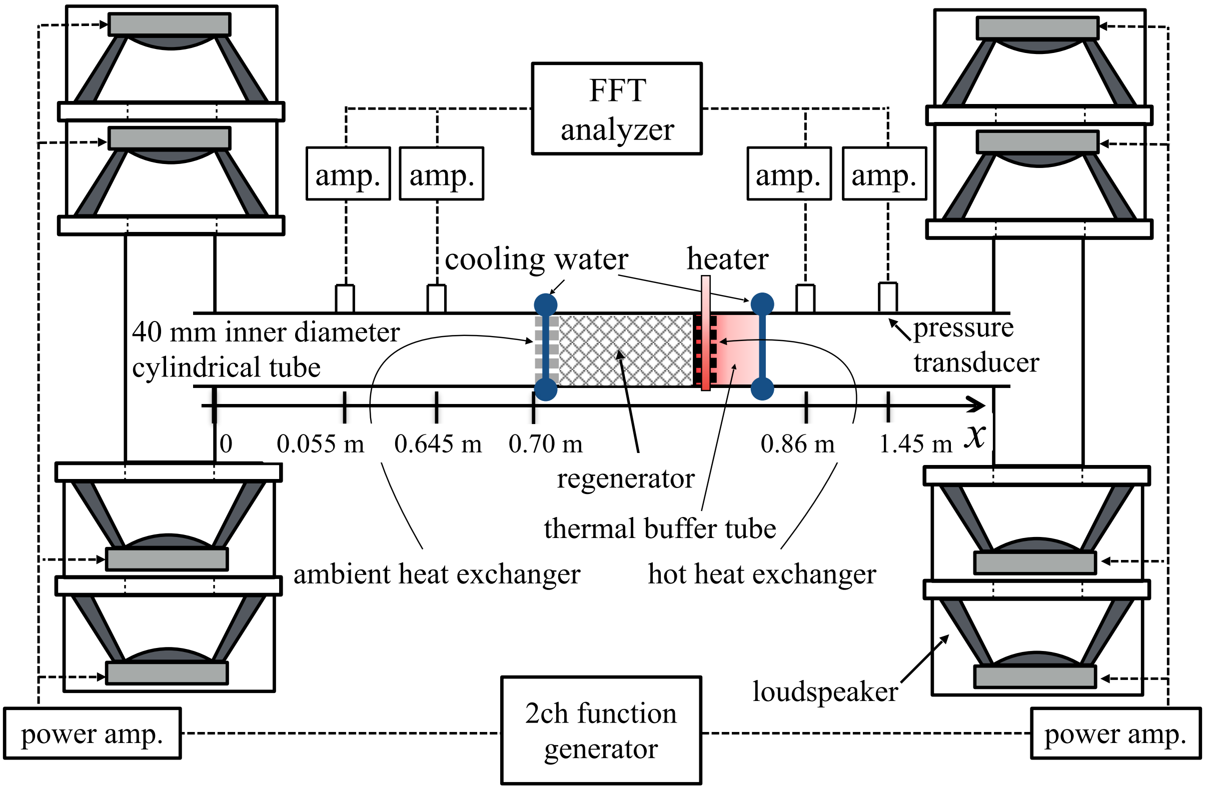
FFT
analyzer
amp.
amp.
amp.
amp.
cooling water
heater
40 mm inner diameter
cylindrical tube
pressure
transducer
0
0.055 m
0.645 m
0.70 m
0.86 m
1.45 m
x
regenerator
thermal buffer tube
ambient heat exchanger
hot heat exchanger
loudspeaker
power amp.
2ch function
generator
power amp.

Figure 4.1: Schematic diagram of the experimental setup. (Figure adapted from Reference 64 and modified by author.)

Equation (4.14), because the heat flow Q goes in the negative x direction and hence it is expressed by a negative value. To avoid confusion, the heat flow was expressed by its flow rate.

Pressure oscillations were monitored using two pairs of pressure transducers (PD104; JTEKT Corp., Osaka, Japan) mounted on the sidewall of the cylindrical tube at the positions presented in Figure 4.1. Based on the pressure amplitudes and phases obtained with a 24 bit fast Fourier transform analyzer (DS-3100; Ono Sokki Co. Ltd.), the acoustic pressure field $p(x,t) = \mathrm{Re}\left[P(x)\exp(i\omega t)\right]$ and the radial average of the axial acoustic particle velocity $u(x,t) = \mathrm{Re}\left[U(x)\exp(i\omega t)\right]$ were determined in the 40-mm tube region by the two-sensor method [58, 59]. From the continuity of volume velocity at the interface between diameter 40 mm tube and the regenerator unit, The complex amplitude V of the cross-sectional average velocity in the hot end of the regenerator was derived as $V_{\mathrm{H}} = U_{\mathrm{H}}/\phi$, where subscript H denotes the location at the hot end of the tube.

Throughout the experiments in this chapter, the specific acoustic impedance at the hot end of the regenerator $Z_{\mathrm{H}} = P_{\mathrm{H}}/U_{\mathrm{H}}$ was adjusted to have the magnitude of $0.3\rho_{\mathrm{m}}a \pm 20\%$ and phase angle of $0^\circ \pm 30^\circ$. $\left|Z_{\mathrm{H}}\right| = 0.3\rho_{\mathrm{m}}a$ enables us to simplify the first term of the right-hand side of Equation (4.3). Namely, when Equation (4.3) is as $Q = Q_{\mathrm{A}} + Q_{\mathrm{D}}$, the ratio of $Q_{\mathrm{A}}/Q_{\mathrm{D}}$ is given as

$$\frac{Q_{\mathrm{A}}}{Q_{\mathrm{D}}} = \frac{\mathrm{Re}\left[g\right]}{\mathrm{Im}\left[g_{\mathrm{D}}\right]} \frac{0.3a\omega}{c_{\mathrm{p}}\left(dT_{\mathrm{m}}/dx\right)}, \tag{4.15}$$

which can be evaluated if the experimental conditions such as dT_{m}/dx, ω, gas type, and the flow channel geometry. In the case of the present ceramic honeycomb catalyst, the ratio $Q_{\mathrm{A}}/Q_{\mathrm{D}}$ was always less than 0.09. Thus, the heat flow Q can be safely approximated by Q_{D}. Therefore, one can expect that $|Q|$ becomes a quadratic function of $|V|$ by Equation (4.3). When the effective radius r_0 of Ueda et al. is used to evaluate the ratio $Q_{\mathrm{A}}/Q_{\mathrm{D}}$ in Equation (4.3), it was found to satisfy $Q_{\mathrm{A}}/Q_{\mathrm{D}} < 0.1$ for all of mesh numbers of screens tested in this chapter. The ratio is expected to further decrease as the effective radius decreases with increasing the velocity amplitude. Therefore, the experimental Q would be approximated by Q_{D} if the thermoacoustic theory for the regular pores is valid in the case of the stacked-screen regenerator.

4.4 Results and Discussion

4.4.1 Regular flow channel regenerator

For the regular pore regenerator made of the ceramic honeycomb catalyst, the relations between the heat flow rate $|Q|$ and the oscillation velocity amplitude $\left|V_{\mathrm{H}}\right|$ are illustrated in Figure 4.2, when the oscillation frequencies are 5 Hz and 200 Hz. As expected in the previous section, the measured $|Q|$ shows a quadratic growth with $\left|V_{\mathrm{H}}\right|$. For comparison, the heat flow rate $|Q|$ and $|Q_{\mathrm{D}}|$ were evaluated by inserting into Equation (4.3) the present experimental conditions and the half of the hydrodynamic diameter $d_{\mathrm{h}}/2 = 0.34$ mm of the regular pore regenerator. Good agreements of heat flow between the theoretical predictions and measurements are observed.

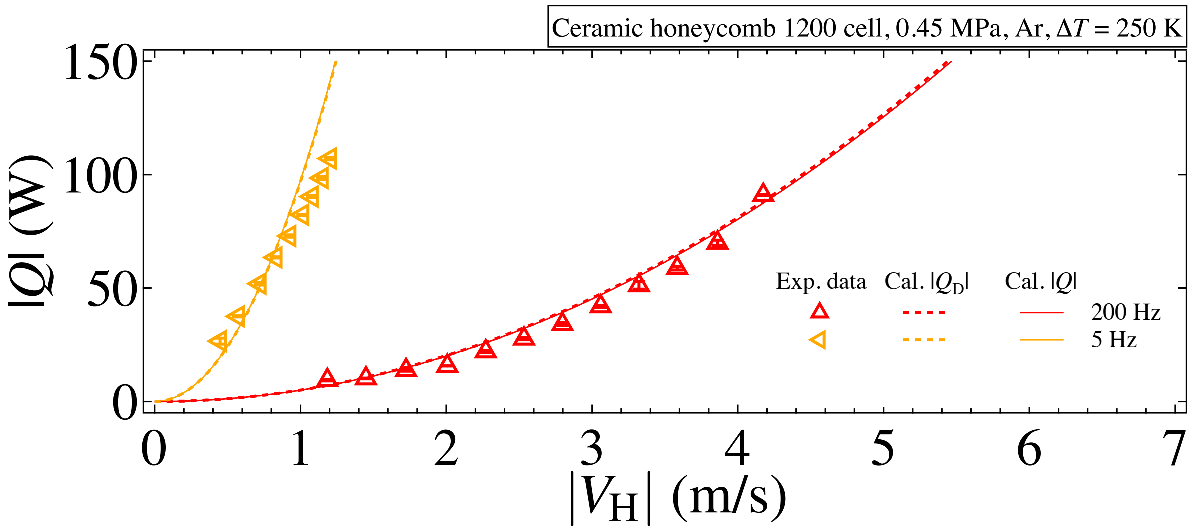

Figure 4.2: Comparison between the experimental heat flow rate $|Q|$ and theoretical calculations is given by Equation (4.3) for the ceramic honeycomb catalyst, where experimentally obtained results are shown as symbols with error bars. The theoretical calculations of $|Q|$ and $|Q_{\mathrm{D}}|$ are shown respectively as solid and dashed curves. (Figure adapted from Reference 64 and modified by author.)

The thermoacoustic theory for estimating the heat flow is thus confirmed by these results. The heat flow rate $|Q|$ of theoretical prediction agrees with experimental value when $\left|V_{\mathrm{H}}\right| \approx 1$ m/s with 5 Hz. The displacement of the gas parcel ($|V_{\mathrm{H}}|/\omega$) is as large as the regenerator length (= 35 mm). The thermoacoustic theory assumes a small amplitude oscillations in principle, but this result indicates that it is applicable even when the displacement amplitude is not so small, relatively to the regenerator size.

4.4.2 Stacked-screen regenerator

For stacked-screen regenerator listed in Table 4.1, the experimental relation between the heat flow rate $|Q|$ and the velocity amplitude $\left|V_{\mathrm{H}}\right|$ for 200 Hz frequency of the oscillatory flow are presented in Figure 4.3. Four panels (a)–(d) of Figure 4.3 compare the measured $|Q|$ and each of the empirical equations listed in this chapter. A quadratic increase with $\left|V_{\mathrm{H}}\right|$ is observed for the measured $|Q|$ as in the case of the regular pore regenerator.

The measured $|Q|$ compared with that obtained using the effective radius of Ueda et al. r_0 to Equation (4.3) are plotted in Figure 4.3 (a). Predictions resulted from r_0 well agree with experimental $|Q|$ of cases of #50, #60, and #80 meshes, and slight deviations are also visible for #20 and #30 meshes. Even though the effective radius r_0 was proposed from experiments with uniform temperature, the present measurements support the usefulness for estimating the heat flow rate $|Q|$ when Ar is the working gas.

Figure 4.3(b) presents the comparison with estimated results from the simple harmonic analysis derived by Swift and Ward, where predictions are show by curves using Equations (4.6),

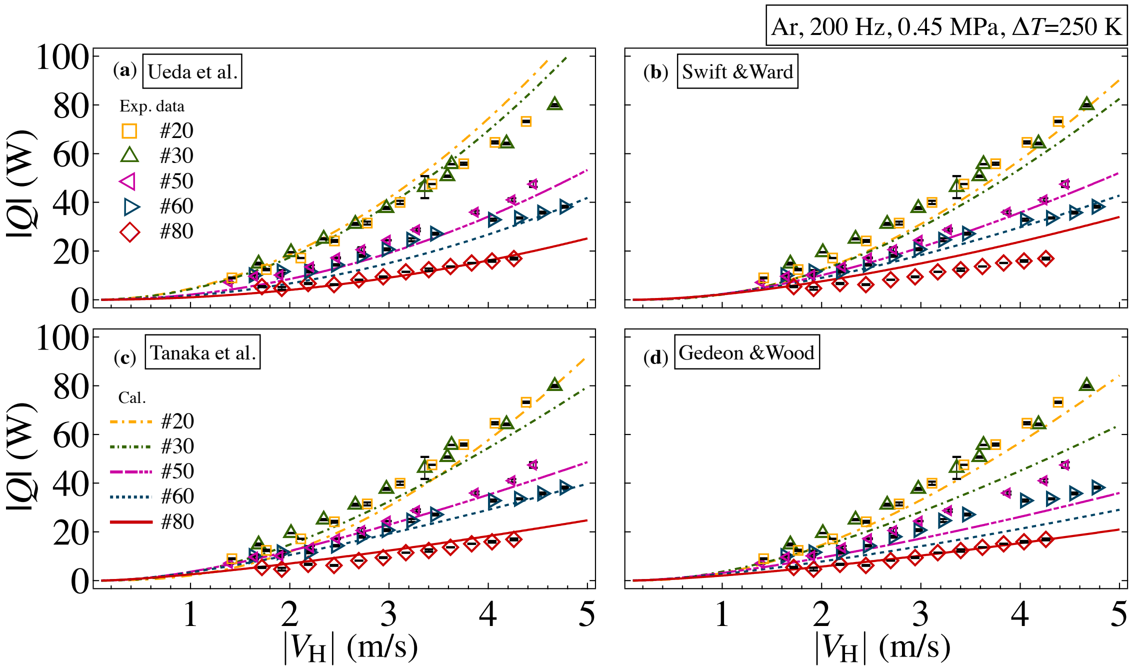

Figure 4.3: Experimental heat flow rate $|Q|$ and predictions given by respective empirical equations cited in this study for stacked-screen regenerators tested in pressurized helium gas with 0.45 MPa and with oscillation frequency of 200 Hz. Each panel presents identical experimentally obtained results by symbols with error bars. The empirical predictions are given respectively as (a) for Ueda et al.; (b) for Swift and Ward; (c) for Tanaka et al.; (d) for Gedeon and Wood. (Figures adapted from Reference 64 and modified by author.)

(4.7), (4.9), and (4.10). Note that θ_T in Equations (4.7) was determined from Equation (4.68) of Reference 12 using $d_{\mathrm{h}}/2$. Except for the #80 mesh, good agreement is obtained in Figure 4.3 (b), although Swift and Ward assumed a good thermal contact between the oscillation gas and the solid wall of the flow channel [38] for the derivation of Equation (4.6). The thermal penetration depth $\delta_\alpha = \sqrt{2\alpha/\omega}$ is 0.15 mm when the frequency is 200 Hz for Ar gas with the mean pressure of 0.45 MPa. Therefore, the present results demonstrates the applicability of the empirical expression of Swift and Ward, when $d_{\mathrm{h}}/(2\delta_\alpha)$ is in the range of $d_{\mathrm{h}}/(2\delta_\alpha) > 1$, rather than $d_{\mathrm{h}}/(2\delta_\alpha) \ll 1$.

Comparisons of the empirical equations of Tanaka et al. and Gedeon & Wood are respectively presented in Figures 4.3 (c) and (d), where Equations (4.11) and (4.12) are used to derive the temperature T_{Nu} in Equation (4.13). Then Equations (4.9) and (4.10) are used to estimate $|Q|$. All predictions presented by curves in Figure 4.3(c) show good agreement with the measured $|Q|$, to a similar degree to those plotted in Figures 4.3 (a) and 4.3 (b). Consequently, for thermoacoustic Stirling engines operating at higher oscillation frequencies than the mechanical Stirling engines [32, 33], their empirical equations are still applicable.

The heat flow rate Q transmitted through the regenerator stacked with #30 mesh screens was further measured with frequencies of 140 Hz and 180 Hz in the same experimental conditions above to check the frequency dependence.

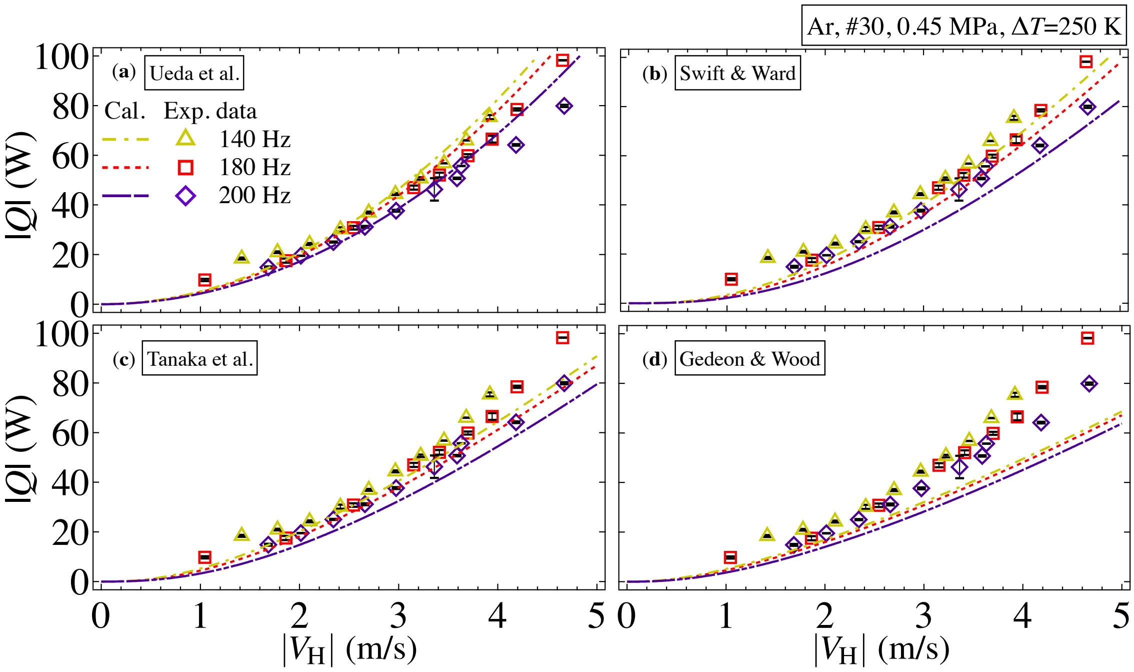

Figure 4.4: Comparisons between the experimental heat flow $|Q|$ and predictions given by the empirical equations. The mesh number of the stacked screens is #30. The working gas is Ar gas with 0.45 MPa. The test frequencies are 140, 180, and 200 Hz. Every panel presents the same experimentally obtained results by symbols with error bars, and empirical predictions are given respectively as the following: (a) for Ueda et al.; (b) for Swift and Ward; (c) for Tanaka et al.; (d) for Gedeon and Wood. (Figures adapted from Reference 64 and modified by author.)

Results are portrayed in Figures 4.4 (a)–4.4 (d), where the experimental heat flow $|Q|$ increases with the decrease of the frequency. Figures. 4.4 (a) and (b) present satisfactory agreements respectively for the effective radius of Ueda et al. and the Swift–Ward formulation. The empirical equation of Tanaka et al. compared with the measured $|Q|$ in (c) also works well. In the case of the empirical equation of Gedeon & Wood as shown in (d), however, it seems that only the tendency of $|Q|$ for the frequency change is reproduced.

4.4.3 Discussion

Through comparisons with measured heat flow rate $|Q|$, the empirical formulations have been found to be useful as a a first approximation of $|Q|$ in the stacked-screen regenerators. The simplest formulation among them is the effective radius of Ueda et al., because it is independent of the Nusselt number Nu, which changes with the Reynolds number Re_h through the velocity amplitude $\left|V_H\right|$. So, we focus on r_0 and test the further applicability. For this purpose, the term of $\mathrm{Im}\left[g_D\right]$ in Equation (4.3) is analyzed by using the experimental $|Q|$.

As described in the last paragraph of Section 4.3, the heat flow component Q_A is negligibly small compared to Q_D. Therefore, $\mathrm{Im}\left[g_D\right]$ can be experimentally determined by approximating

Q with Q_D as

$$\mathrm{Im}\left[g_D\right] = \frac{2}{A}\frac{\omega}{\rho_m c_p}\frac{Q}{(dT_m/dx)\left|V_H\right|^2}. \tag{4.16}$$

The measured values and the thermal properties of the gas at the hot end of the regenerator (T_H=543 K) are used to evaluate all the quantities in Equation (4.16). Figure 4.5 presents the estimated $\mathrm{Im}\left[g_D\right]$, where r/δ_α values in the horizontal axis of experimental results were determined from r_0 and the thermal properties with hot end temperature of the regenerator of T_H=543 K, and the curve shows the theoretical $\mathrm{Im}\left[g_D\right]$ when $\sigma = 0.66$. In the figure, symbols show the mean values over different $\left|V_H\right|$, while the error bars attached on the symbols signify the standard deviations for showing the degree of the influence of $\left|V_H\right|$. Results show that $\mathrm{Im}\left[g_D\right]$ in Equation (4.16) determined from measured heat flow rate $|Q|$ approximates the theoretical value predicted from the cylindrical flow channel. This results demonstrates that the mechanism of oscillation-induced heat flow in the stacked-screen regenerator is mainly governed by the non-dimensional quantity r_0/δ_α through the thermoacoustic theory. This observation agrees with previous report of Hasegawa et al. [63] using air at atmospheric pressure as the working gas. Consequently, r_0/δ_α would be the key parameter for the local heat transfer between the screen meshes and the oscillatory flow.

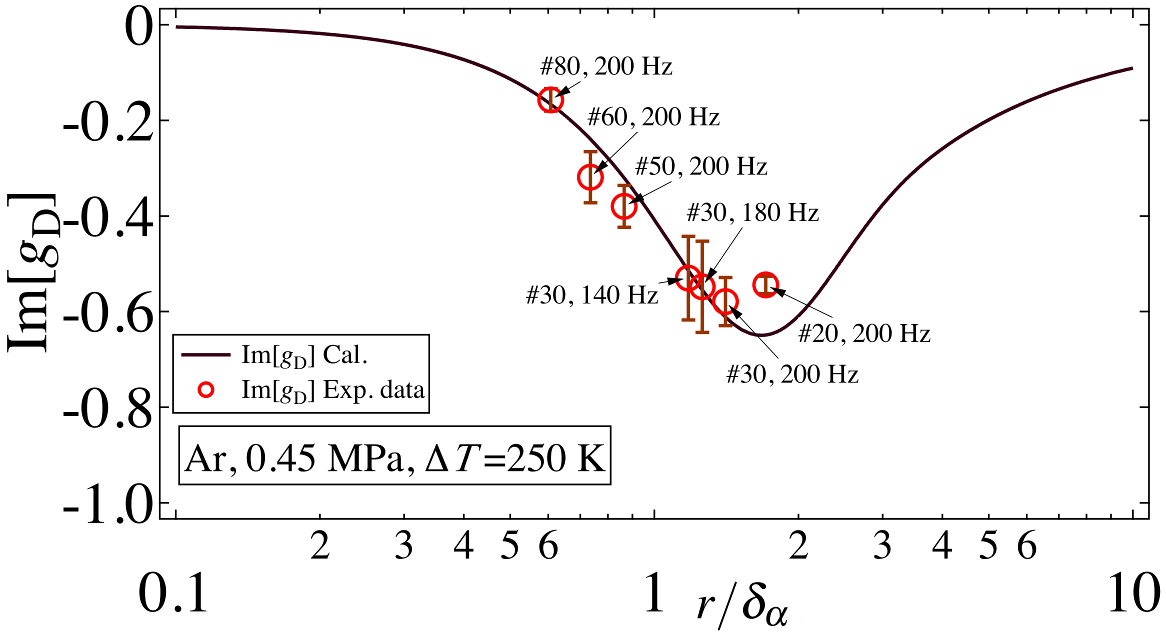

Figure 4.5: Relation between $\mathrm{Im}\left[g_D\right]$ and r/δ_α. The curve of $\mathrm{Im}\left[g_D\right]$ was calculated from the thermoacoustic theory. The symbols represent the experimental values evaluated from Equation (4.16) with measured data and the thermal properties of the gas at the hot end of the regenerator (T_H=543 K). (Figure adapted from Reference 64 and modified by author.)

In Chapter 2, the flow resistance of the stacked-screen regenerator was found to have a velocity dependence, which was consistent with the earlier experiments of acoustic propagations through porous media with tortuous flow channels [66–68] and the friction factor of stacked screen meshes [25, 32–34, 69]. In Chapter 3, from comparison with the measured acoustic fields, the effective radius r_{eff} was proposed as

$$r_{\mathrm{eff}} = \left(\frac{0.8\nu}{4\delta_\nu^2 \omega d_{\mathrm{h}}^2} Re_{\mathrm{h}} + {r_0}^{-2} \right)^{-\frac{1}{2}}. \tag{4.17}$$

In the equation, r_{eff} reduces to r_0 when the velocity goes to zero, and decreases with increasing the velocity amplitude. We present here the applicability of r_{eff} using the experimental results of this chapter.

The experimental effective radius $r_{\mathrm{eff,exp}}$ was obtained from the measured acoustic fields of #30 and #80 in the same way as with in Chapter 3. Figure 4.6 presents $r_{\mathrm{eff,exp}}$ thus obtained and the effective radii in Equation (4.17), where the horizontal axis represents the average velocity amplitude over the regenerator. The experimental effective radius $r_{\mathrm{eff,exp}}$, estimated from error $< 8\%$ between the measured and calculated acoustic powers, is not constant against the velocity, but decreases with it. As a result, we see that the acoustic field at both sides of the regenerator unit is better estimated by using the effective radius r_{eff} than r_0.

The heat flow rates $|Q|$ estimated from using r_0 and r_{eff} in Equation (4.3) are compared in Figure 4.7. Because of the decrease due to the increase of $|V_{\mathrm{H}}|$, r_{eff} gives the smaller $|Q|$ than r_0. As r_0 reproduces well the heat flow rates $|Q|$, it is concluded that r_0 should be employed instead of r_{eff} for better estimation of heat flow, while the acoustic field is better described by r_{eff}.

The necessity of two effective radii for explaining sound propagation behaviors due to thermal conductivity and viscosity in tortuous porous media has been also pointed out in other studies [67, 47] made in the uniform temperature condition. They attributed the narrower regions of the channel to the viscous effects and the wider regions to the thermal effects [40, 46]. The result of this chapter indicates the need of the effective thermal radius to explain the axial heat transport, in addition to the effective viscous radius revealed in Chapters 2 and 3.

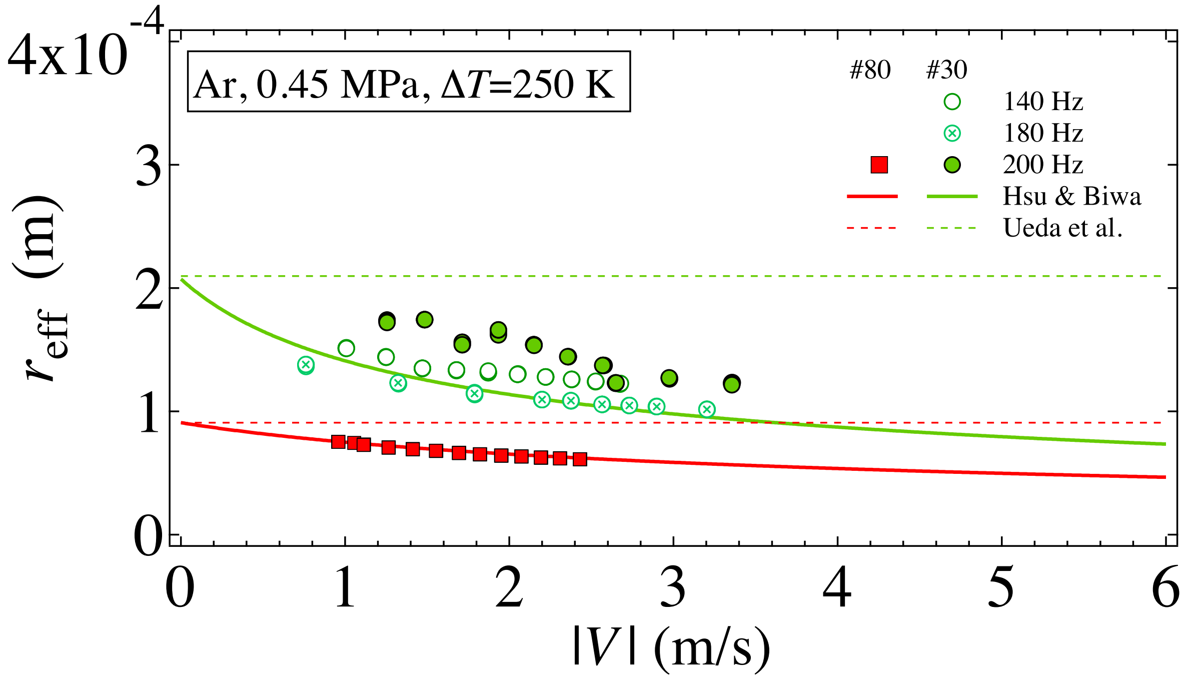

Figure 4.6: Relation between r_{eff} and $|V|$. Symbols represent the experimental effective radius of the stacked-screen regenerator of #30 mesh and # 80 mesh. The curve stands for Equation (4.17) with thermal properties of the gas determined from a temperature averaged in T_{R} and T_{H}. The horizontal dashed line represents the effective radius r_0 of Ueda et al. (Figure adapted from Reference 64 and modified by author.)

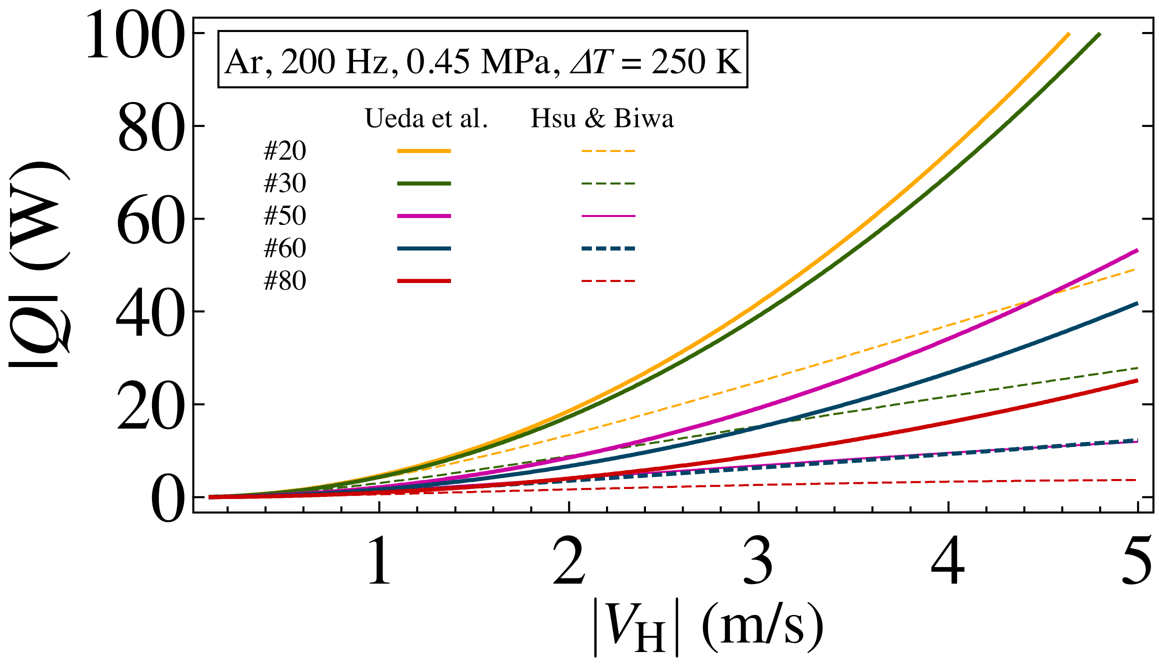

Figure 4.7: Comparisons between predictions of heat flow $|Q|$ given respectively by the effective radius of Ueda et al. and Hsu & Biwa, for stacked-screen regenerators in pressurized argon gas with 0.45 MPa and oscillation frequency of 200 Hz. (Figure adapted from Reference 64 and modified by author.)

4.5 Conclusions

Heat flow rate $|Q|$ transmitted through the stacked screen regenerators was measured in oscillatory flow using pressurized argon gas with the mean pressure of 0.45 MPa. Experimentally obtained $|Q|$ was compared with predictions estimated from four empirical equations which was expressed in terms of by r_0/δ_α and/or Re_h. All of empirical equations reproduced the measured heat flow rates to the similar extent to each other. The Ueda's formulation using the effective radius r_0 would be useful for designing thermoacoustic engines, because of its simplicity. The acoustic field, however, was better explained by the effective radius r_eff than r_0. This results mean that the effective radius r_eff should be used to describe the acoustic field, and then r_0 should be used to determine the acoustic heat transport in the stacked screen regenerators.

Chapter 5

Experimental verification of the effective radii

5.1 Introduction

For thermoacoustic oscillation systems consisting of regular flow channels, a linear stability analysis has been successfully demonstrated to predict a critical temperature ratio of hot to cold parts at the onset of gas oscillations. Rott [5–10] derived linearized basic equations of hydrodynamics for a circular flow channel to determine a neutral stability curve of Taconis oscillations [11] occurring in a gas-filled tube with a very steep temperature gradient. While Rott assumed a step-function like temperature distribution, Sugimoto [70] reconsidered the stability problem by assuming a more realistic temperature profile without discontinuity. The linear stability analysis has been carried out for predicting the critical temperature ratio of various thermoacoustic engines [71–74], and the availability was confirmed by experiments as long as the flow channel shapes are regular in all the components. Therefore, if one can extend this analysis to thermoacoustic engines having stacked-screen mesh regenerators, a useful design method would be gained for developing practical thermoacoustic engines, as they employ stacked-screen meshes instead of stack of plates [19, 22].

In previous chapters, the effective radius r_{eff} was proposed based on measurements of the acoustic fields, which gave reasonable prediction of the acoustic power difference ΔW across the stacked-screen regenerator with and without the axial temperature difference. Also from measurements of the heat flow transmitted through the regenerator, the effective radius r_0, originally proposed by Ueda [49], was shown to better describe the heat flow rate than r_{eff}. The effective radii r_{eff} and r_0 are respectively written as:

$$r_{\mathrm{eff}} = \left(\frac{0.8\nu}{4\delta_\nu^2 \omega d_{\mathrm{h}}^2} Re_{\mathrm{h}} + {r_0}^{-2} \right)^{-\frac{1}{2}}, \tag{5.1}$$

and

$$r_0 = \frac{\sqrt{d_\mathrm{h} d_\mathrm{w}}}{2}. \tag{5.2}$$

In these two effective radii, ω stands for the oscillation angular frequency, δ_ν and ν respectively denote the viscous penetration depth and kinematic viscosity of the working gas, d_w and d_h respectively signify the wire diameter of woven mesh screens and hydraulic diameter of the stacked-screen regenerator. Also, the Reynolds number Re_h is defined as $Re_\mathrm{h} = |V| d_\mathrm{h}/\nu$, where $|V|$ denotes the spatial mean velocity amplitude in the region of the stacked-screen regenerator. As can be seen in Equation (5.1), r_eff decreases from r_0, when the velocity increases from zero to finite value through the Reynolds number dependent term. As the thermoacoustic oscillation spontaneously grows from a small disturbance, it would be reasonable to consider that r_0 characterizes the onset conditions of the thermoacoustic engine. After the engine onset, however, r_eff would come to play as the acoustic amplitude increases in the regenerator. Finally the steady oscillations would be achieved when the engine becomes neutrally stable with r_eff for a given temperature ratio. That temperature ratio should be greater than the critical one, because the viscous loss is increased by the reduction of r_eff. In the steady state, the heat flow due to gas oscillations would be estimated by using r_0. By using the acoustic power increase ΔW in the stacked-screen regenerator, the thermal efficiency could be calculated as $\Delta W/Q_\mathrm{in}$, where Q_in includes the heat flow due to gas oscillations and the conduction heat given by thermal conductivity of the gas and the solids.

In this chapter, model thermoacoustic engines of a looped tube type and a straight tube are tested. A calculation method of the performances is proposed by incorporating the effective radii r_eff and r_0 into the linear analysis of thermoacoustic oscillations. The calculation results are compared with measurements of the critical temperature ratio for the onset of oscillations, saturation pressure amplitude at the steady oscillation state, and the thermal efficiency given by $\Delta W/Q_\mathrm{in}$, to see the applicability of a design method of thermoacoustic engines using stacked-screen regenerators.

5.2 Experimental method

5.2.1 Model thermoacoustic engines

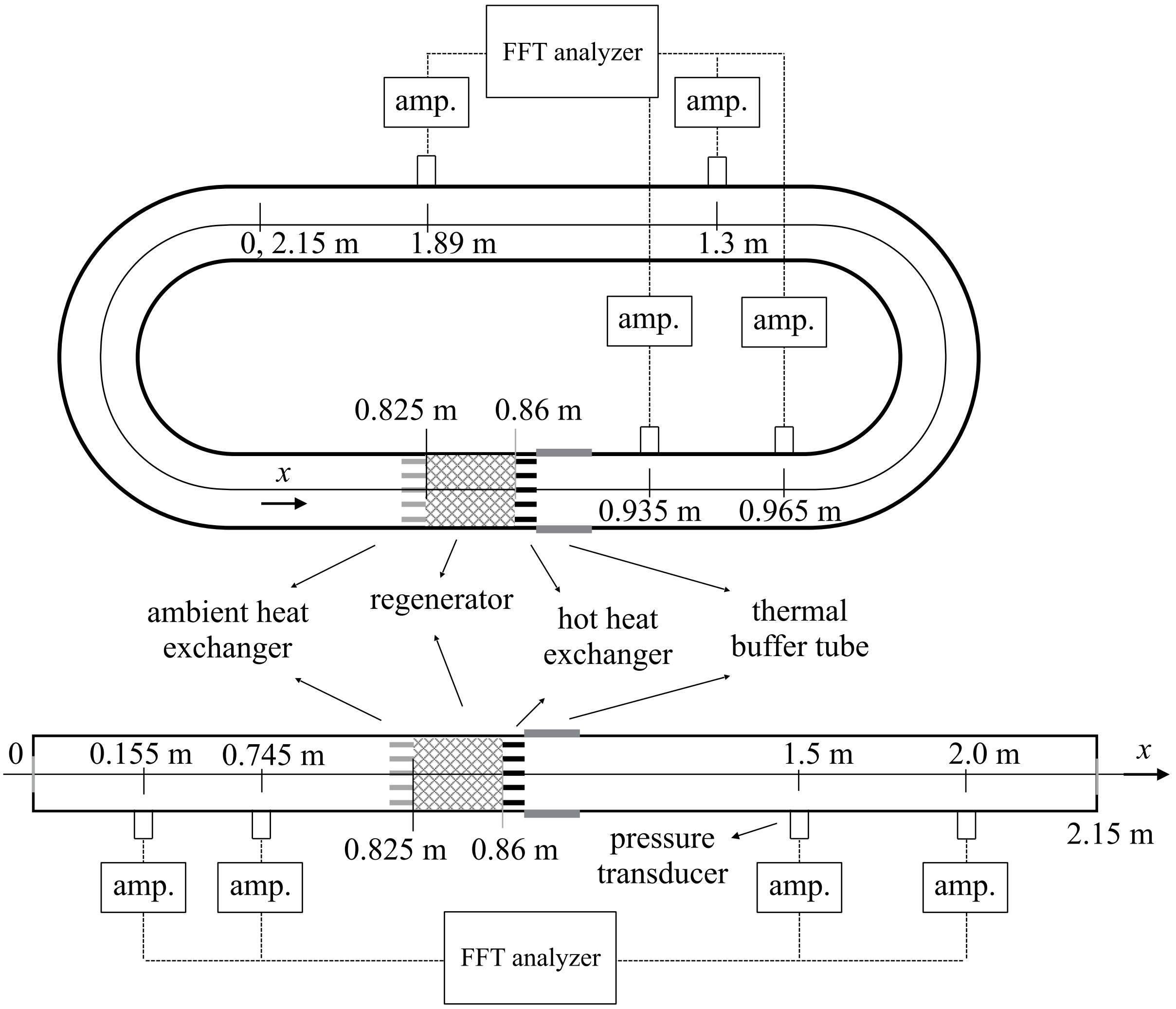
FFT analyzer
amp.
amp.
0, 2.15 m
1.89 m
1.3 m
amp.
amp.
0.825 m
0.86 m
x
0.935 m
0.965 m
ambient heat exchanger
regenerator
hot heat exchanger
thermal buffer tube
0
0.155 m
0.745 m
1.5 m
2.0 m
x
0.825 m
0.86 m
pressure transducer
2.15 m
amp.
amp.
amp.
amp.
FFT analyzer

Figure 5.1: Schematic diagram of the experimental setups of the looped tube engine (top) and the straigh tube engine (bottom).

Figure 5.1 presents two types of model thermoacoustic engines employed in this study. One is the looped tube engine [18]. The loop was made of 40-mm inner diameter cylindrical tubes and elbows of the same internal cross-sectional area. The average length of the loop is $L = 2.15$ m. The loop contained a regenerator unit consisting of an ambient heat exchanger, a stacked-screen regenerator, a hot heat exchanger, and a thermal buffer tube. Metallic woven mesh screens of #30, #40, #50, and #60, listed in Table. 5.1 with the detailed information, were tested as the regenerator material. The engine was filled with different working gases and mean pressures, as listed in the Table 5.2.

The other is the straight tube engine [16], whose regenerator material and working gas are also listed in the Table 5.2. The tube consisted of 40-mm inner diameter cylindrical tubes. The tube length was also $L = 2.15$ m. The same regenerator unit as the looped tube engine was inserted in the straight tube. In order to achieve the same working frequency, the regenerator unit was intentionally placed at a position $3L/8$ away from one end of the tube, with facing the ambient side to that end. By doing so, the second mode oscillations, or the one-wavelength mode oscillations, was introduced in the straight tube engine. This oscillation mode has the same wavelength and the same frequency as the fundamental mode of the looped tube.

For the straight thermoacoustic engine, the axial coordinate x was taken to the right along the central axis with $x = 0$ at the left end; for the looped thermoacoustic engine, the axial coordinate x ($0 \le x$ (m) ≤ 2.15) was directed from cold to hot in the regenerator, and the origin $x = 0$ was taken in the way that regenerator unit was placed in the same region of $0.825 < x$ (m) < 0.860 as the straight tube engine.

These two engines can be divided into six components as: waveguide tube 1 ($0 < x$ (m) < 0.805), ambient heat exchanger ($0.805 < x$ (m) < 0.825), stacked-screen regenerator ($0.825 < x$ (m) < 0.86), hot heat exchanger ($0.86 < x$ (m) < 0.88), thermal buffer tube ($0.88 < x$ (m) < 0.93), and waveguide tube 2 ($0.93 < x$ (m) < 2.15). Here, the heat exchangers and the thermal buffer tube in the experimental setup of this chapter were identical to those used in previous chapters. The hot heat exchanger was heated by three identical electrical cartridge heaters connected to a DC power supply. The heat power Q_{in} to the engine is given by the total heat input from those electrical heaters. The ambient heat exchanger and one end of the thermal buffer tube were maintained at 293 K by cooling water circulating around them. Type-K thermocouples were inserted at $x = 0.825$ m and $x = 0.86$ m to determine temperatures at both ends of the regenerator. The ambient end temperature is denoted as T_{R} and the hot end temperature as T_{H}. The temperature ratio $T_{\mathrm{H}}/T_{\mathrm{R}}$ between two ends of the regenerator were recorded.

Table 5.1: Geometrical properties of regenerators used in the thermoacoustic engines.

Mesh number	Wire diameter (mm) d_{w}	Hydraulic diameter (mm) d_{h}	Volume porosity ϕ
#30	0.22	0.8	0.78
#40	0.2	0.63	0.82
#50	0.14	0.47	0.77
#60	0.12	0.28	0.77

5.2.2 Experimental procedure

The model thermoacoustic engines were tested in the following way. Heat power Q_{in} was supplied from the hot heat exchanger to the regenerator, and it was kept until the steady state was achieved. When the heat power exceeded a threshold value, the gas column started to oscillate spontaneously. The oscillation mode was of the fundamental mode in the looped tube engine and of the second mode in the straight tube engine, so the oscillation frequencies were essen-

Table 5.2: Experimental conditions for testing the thermoacoustic engines.

Working gas	Mean pressure (MPa)	Engine type	Mesh number
Ar	0.45	straight	#30, #40, #50
		loop	#30, #60
N_2	0.6	straight	#30, #40, #50
	0.65	loop	#40

tially the same as each other. The temperature ratio $T_\mathrm{H}/T_\mathrm{R}$ between the ends of the regenerator at the threshold heat power was measured as the critical temperature ratio of the engine, which is used to plot the stability curve of the engine.

The acoustic pressures at the steady oscillation state were measured by using two pairs of pressure transducers flush mounted on the tube walls of waveguide tubes 1 and 2 shown in Figure 5.1. Pressure signals of 8192 sampling points were sampled at a sampling frequency 800 Hz, from which the amplitude spectrum and phase spectrum were determined via a fast-Fourier-transform algorithm. The two-sensor method was then adopted to determine the acoustic fields of acoustic pressure $p(x) = \mathrm{Re}\Big[P(x)\exp(i\omega t)\Big]$ and the radial average of the axial acoustic particle velocity $u(x) = \mathrm{Re}\Big[U(x)\exp(i\omega t)\Big]$ in the region of waveguide tubes 1 and 2. The acoustic field measurements were carried out for $T_\mathrm{H}/T_\mathrm{R}$ values above the onset temperature ratio, to observe the evolution of steady pressure oscillations with T_H.

The thermal efficiency of the energy conversion in the regenerator was determined using the heat power Q_in by the heater and the acoustic power increase ΔW across the regenerator as

$$\eta = \frac{\Delta W}{Q_\mathrm{in}}. \tag{5.3}$$

The heat power Q_in was determined from the measured voltage and current of the heaters, while the acoustic power increase ΔW was measured from acoustic powers at both ends of the regenerator. If the electroacoustic transducer (electric alternator) or a acoustic cooler is connected to the model engines, the acoustic power is supplied from the model engines to them. The maximum available acoustic power is given by ΔW, and therefore it is used to define the thermal efficiency of the engine.

5.3 Calculation method

5.3.1 Transfer matrices

This section introduces the method of using transfer matrices described in Chapter 3 for the stability analysis of the thermoacoustic engines, and explain how to modify it to be applicable to the engines having stacked-screen regenerators. The acoustic pressure $P(x)$ and the volume velocity, $AU(x)$, given by a product of the flow channel cross-sectional area A and the radial average $U(x)$ of the axial acoustic particle velocity at position x is related to those $P(x + \Delta x)$ and $AU(x + \Delta x)$ at position $x + \Delta x$ in the following equations. For components having the temperature gradient, such as the regenerator M_{REG} and thermal buffer tube M_{TBT}, the transfer matrix is expressed as

$$M_{\mathrm{REG\,or\,TBT}} = \exp\left(\frac{\mathbb{G}\Delta x}{2}\right)\begin{bmatrix} -\frac{\mathbb{G}}{\tau}\sinh(\lambda) + \cosh(\lambda) & \frac{2\mathbb{Z}}{\tau}\sinh(\lambda) \\ \frac{2\mathbb{Y}}{\tau}\sinh(\lambda) & \frac{G}{\tau}\sinh(\lambda) + \cosh(\lambda) \end{bmatrix}, \tag{5.4}$$

with $\tau = \sqrt{\mathbb{G}^2 + 4\mathbb{Y}\mathbb{Z}}$ and $\lambda = \tau\Delta x/2$, where Δx represents the length of the component. In the equation, definitions of $\mathbb{G}$, $\mathbb{Z}$, $\mathbb{Y}$, and τ are the same as those in Section 3.1.2, which are characterized by thermoacoustic functions of

$$\chi_{\sharp} = \frac{2J_1\left[(i-1)\frac{r}{\delta_{\sharp}}\right]}{(i-1)\frac{r}{\delta_{\sharp}}J_0\left[(i-1)\frac{r}{\delta_{\sharp}}\right]} \tag{5.5}$$

for cylindrical flow channels with radius r, as components of the regenerator and thermal buffer tube. For components with uniform temperature, like ambient and hot heat exchanger, and waveguide tube, the transfer matrix is formulated as

$$M_{\mathrm{T,\,R\,or\,H}} = \begin{bmatrix} \cosh\left(\grave{\lambda}\right) & \sqrt{\frac{\mathbb{Z}}{\mathbb{Y}}}\sinh\left(\grave{\lambda}\right) \\ \sqrt{\frac{\mathbb{Y}}{\mathbb{Z}}}\sinh\left(\grave{\lambda}\right) & \cosh\left(\grave{\lambda}\right) \end{bmatrix}, \tag{5.6}$$

where $\grave{\lambda} = \Delta x\sqrt{\mathbb{Y}\mathbb{Z}}$. For heat exchangers made of parallel plates with spacing $2r_{\mathrm{d}}$, thermoacoustic functions are given by

$$\chi_{\sharp} = \frac{\tanh\left[(1+i)\frac{r_{\mathrm{d}}}{\delta_{\sharp}}\right]}{(1+i)\frac{r_{\mathrm{d}}}{\delta_{\sharp}}}. \tag{5.7}$$

A linear temperature distribution was assumed in regions of the regenerator and the thermal buffer tube. The transfer matrices M_{R} and M_{TBT} were divided into 100 segments with respect to x direction, in the same way as in Section 3.2. The products of the divided matrices $M_{\mathrm{R},\dagger}$ and $M_{\mathrm{TBT},\dagger}$ are respectively used as the transfer matrices of the regenerator M_{R} and M_{TBT}, where subscript † represents the transfer matrix of the †-th segment specified by the thermal properties of the gas at the local temperature. The effective radius r_0 is employed as the regenerator pore channel radius for the discussion of the onset temperature ratio. Later, the velocity dependent effective radius r_{eff} is incorporated in the calculation.

The two thermoacoustic engines illustrated in Figure 5.1 are expressed with the transfer matrices as

$$M_{\mathrm{All}} = M_{\mathrm{tube,2}} M_{\mathrm{TBT}} M_{\mathrm{H}} M_{\mathrm{REG}} M_{\mathrm{R}} M_{\mathrm{tube,1}}, \tag{5.8}$$

where subscripts tube,1 or 2, R, REG, H, TBT of matrices M, respectively, stand for the 40-mm-diameter waveguide tube, cold heat exchanger, regenerator, hot heat exchanger, and thermal buffer tube. The transfer matrix M_{All} relates the acoustic states between both ends of the thermoacoustic engine as follows:

$$\begin{pmatrix} P_{\mathrm{L}} \\ AU_{\mathrm{L}} \end{pmatrix} = M_{\mathrm{All}} \begin{pmatrix} P_{\mathrm{o}} \\ AU_{\mathrm{o}} \end{pmatrix} = \begin{pmatrix} F_{11} & F_{12} \\ F_{21} & F_{22} \end{pmatrix} \begin{pmatrix} P_{\mathrm{o}} \\ AU_{\mathrm{o}} \end{pmatrix}, \tag{5.9}$$

where subscripts o and L of P and U respectively denote locations at $x = 0$ and $x = 2.15$ m in Fig 5.1, and $F_{\vee,\wedge}$ $(\vee, \wedge = 1, 2)$ stands for the matrix components of M_{All}.

The boundary conditions required for P and U are different in the looped tube engine and the straight tube engine. For the looped tube thermoacoustic engine, a periodic boundary condition of $P_{\mathrm{L}} = P_{\mathrm{o}}$ and $U_{\mathrm{L}} = U_{\mathrm{o}}$ should be satisfied. Therefore, Equation (5.9) is rewritten as

$$\frac{P_{\mathrm{o}}}{AU_{\mathrm{o}}} = \frac{F_{12}}{1 - F_{11}} = \frac{1 - F_{22}}{F_{21}}. \tag{5.10}$$

In order to have nonzero P_{o} and U_{o}, the following relation must be satisfied.

$$(1 - F_{11})(1 - F_{22}) - F_{12}F_{21} = 0. \tag{5.11}$$

For the straight thermoacoustic engine with both ends closed, the boundary conditions are given as $U_{\mathrm{o}} = 0$ and $U_{\mathrm{L}} = 0$. Therefore, the following relation must be satisfied.

$$F_{21} = 0. \tag{5.12}$$

5.3.2 Calculation of stability curve

The onset conditions of the looped tube engine and the straight tube engine are numerically solved with respect to the angular frequency by assuming the temperature ratio $T_{\mathrm{H}}/T_{\mathrm{R}}$ in Equations (5.11) or (5.12), respectively. The Newton-Raphson method with an initial angular frequency of $2\pi a/L$ was used for a complex angular frequency $\omega = \omega_\mathrm{R} + i\omega_\mathrm{I}$, where a is the adiabatic speed of sound of the working gas. It should be noted here that the acoustic pressure is expressed as

$$p(x,t) = \mathrm{Re}\Big[P(x)\exp(i\omega t)\Big] \tag{5.13}$$
$$= \mathrm{Re}\Big\{\Big[\exp(-\omega_\mathrm{I} t)P(x)\Big]\exp(i\omega_\mathrm{R} t)\Big\},$$

which means that $p(x,t)$ is temporally oscillating with the angular frequency ω_R while changing the instantaneous amplitude exponentially in time with attenuation/growth constant ω_I. Therefore, the system is stable (non-oscillating) if $\omega_\mathrm{I} > 0$; unstable if $\omega_\mathrm{I} < 0$, and at the onset of oscillation (neutrally stable) if $\omega_\mathrm{I} = 0$.

In this study, the onset of the thermoacoustic engine was judged whether the relation $|\omega_\mathrm{I}| < 10^{-8}$ is achieved for a certain value of $T_\mathrm{H}/T_\mathrm{R}$. Because the thermoacoustic oscillations start from a small fluctuation, the onset condition is calculated using the effective radius of Ueda et al. r_0 for M_REG. Thus, the stability curve was created by plotting the critical value of $T_\mathrm{H}/T_\mathrm{R}$ for a given value of r_0.

5.3.3 Calculation of oscillation amplitude

When the imaginary part ω_I of the angular frequency becomes negative for a given value of ΔT, the linear theory states that the oscillation amplitude should grow infinitely large after a time. In reality, however, the amplitude saturates at a certain value. The plausible reasons for the amplitude saturations are the velocity-dependent losses in the stacked screen regenerator, minor losses at elbows [75], tees [76], and cross-sectional area change [77, 78], wave distortion due to excitation of higher harmonics [79, 80], acoustic streaming [81–83] such as Rayleigh type [4] and Gedeon type [84], and heat exchanger performance that limits the absorption rate of heat from outside [85]. At the present understanding of thermoacoustics, the contribution of these mechanisms are unclear. We assume here that the amplitude saturation is solely caused by the velocity-dependent power losses in the stacked screen regenerator described in Chapter 2, and try to estimate the oscillation amplitude at steady oscillation state.

First, for a given value of r_0 and the corresponding value of $T_\mathrm{H}/T_\mathrm{R}$ that makes $|\omega_\mathrm{I}| < 10^{-8}$, all the matrix components of M_All are determined. By assuming a small P_o, U_o is obtained as $U_\mathrm{o} = \dfrac{P_\mathrm{o}}{A}\dfrac{1-F_{22}}{F_{21}}$ for the looped tube engine, whereas $U_\mathrm{o} = 0$ for the straight tube engine's boundary condition. The acoustic fields at both ends of the regenerator are calculated from following equations

$$\begin{pmatrix} P_\mathrm{R} \\ AU_\mathrm{R} \end{pmatrix} = M_\mathrm{R} M_{\mathrm{tube},1} \begin{pmatrix} P_\mathrm{o} \\ AU_\mathrm{o} \end{pmatrix} \tag{5.14}$$

and

$$\begin{pmatrix} P_{\mathrm{H}} \\ AU_{\mathrm{H}} \end{pmatrix} = M_{\mathrm{REG}} \begin{pmatrix} P_{\mathrm{R}} \\ AU_{\mathrm{R}} \end{pmatrix}, \tag{5.15}$$

where M_{REG} is evaluated using the effective radius r_0. From above equations, the velocity amplitude in the regenerator is determined as $|V| = \left|V_{\mathrm{H}} + V_{\mathrm{R}}\right|/2$, where $V_{\mathrm{H}} = U_{\mathrm{H}}/\phi$ and $V_{\mathrm{R}} = U_{\mathrm{R}}/\phi$ with the volume porosity ϕ.

Secondly, $T_{\mathrm{H}}/T_{\mathrm{R}}$ is set at the value greater than the onset temperature ratio. The resulting solution ω of Equations (5.11) or (5.12) should possess a negative ω_{I}. Considering that the pressure is given as $p_{\mathrm{o}}(t) = \mathrm{Re}\left\{\left[\exp(-\omega_{\mathrm{I}} t) P_{\mathrm{o}}\right] \exp(i\omega_{\mathrm{R}} t)\right\}$ in the time domain, $p_{\mathrm{o}}(t+\mathrm{t})$ would be amplified by a factor of $\exp(-\omega_{\mathrm{I}}\mathrm{t})$ after a short time interval t, where t was chosen as a/L. The increased pressure thus obtained is used to calculate U_{o} and then the velocity amplitude $|V|$ in the regenerator. From the velocity amplitude $|V|$, the velocity-dependent effective radius r_{eff} is calculated and it is used to update the transfer matrix M_{REG}.

Thirdly, by using the updated transfer matrix M_{REG}, ω_{I} is determined, which is again used to change the value of P_0, and then the velocity amplitude in the regenerator $|V|$. These processes are repeated until $\left|\omega_{\mathrm{I}}\right| < 10^{-8}$ is satisfied for the assumed value of $T_{\mathrm{H}}/T_{\mathrm{R}}$.

The final value of P_{o} is associated with the steady oscillation state with the oscillation frequency ω_{R}. The acoustic fields can be calculated from Equation (5.9). By using the acoustic fields thus obtained, Equations (5.14) and (5.15) enable to calculate acoustic power at both ends of the regenerator. The acoustic difference ΔW across the regenerator is thus given as

$$\Delta W = \frac{1}{2} A \left(\mathrm{Re}\left[\widetilde{P_{\mathrm{H}}} U_{\mathrm{H}}\right] - \mathrm{Re}\left[\widetilde{P_{\mathrm{R}}} U_{\mathrm{R}}\right] \right). \tag{5.16}$$

Also, the heat Q transmitted through the regenerator is calculated by

$$Q = -\frac{1}{2} A \mathrm{Re}\left[g P \widetilde{V} \right] + \frac{1}{2} A \frac{\rho_{\mathrm{m}} c_{\mathrm{p}}}{\omega} \mathrm{Im}\left[g_{\mathrm{D}} \right] \frac{dT_{\mathrm{m}}}{dx} |V|^2 \tag{5.17}$$

$$\text{with} \quad g = \frac{\chi_\alpha - \widetilde{\chi_\nu}}{(1+\sigma)\left(1 - \widetilde{\chi_\nu}\right)} \quad \text{and} \quad g_{\mathrm{D}} = \frac{\chi_\alpha + \sigma \widetilde{\chi_\nu}}{\left(1-\sigma^2\right)\left|1-\chi_\nu\right|^2}.$$

In the equation, thermoacoustic functions $\chi_\sharp$ ($\sharp = \nu, \alpha$) are estimated from r_0, based on the fact that r_0 gave a better estimation of Q than r_{eff} in Chapter 4. The total heat power Q_{in} is assumed as the sum of Q and the conduction heat through the gas and solids, and therefore, it is expressed as

$$\begin{aligned} Q_{\mathrm{in}} = |Q| + Ak\left(\phi \left| \frac{dT_{\mathrm{m,REG}}}{dx} \right| + \left| \frac{dT_{\mathrm{m,TBT}}}{dx} \right| \right) \\ + k_{\mathrm{s}} \left[\left(\texttt{ksFrac}\, A \left(1-\phi\right) + A_{\mathrm{s}} \right) \left| \frac{dT_{\mathrm{m,REG}}}{dx} \right| + A_{\mathrm{s}} \left| \frac{dT_{\mathrm{m,TBT}}}{dx} \right| \right], \end{aligned} \tag{5.18}$$

where $\frac{dT_\mathrm{m}}{dx}$ with subscripts of REG and TBT respectively denote axial temperature gradients along the regenerator and thermal buffer tube, k is the thermal conductivity of the working gas, and A_s and k_s are respectively the cross-sectional area and the thermal conductivity of the solid pipe. In the equation, a reduction factor `ksFrac` accounting for the solid heat conduction of the stacked-screen regenerator is used [86], which was determined as 0.3 in the calculation example of the thermoacoustic Stirling engine developed by Backhaus and Swift [76] shown in DeltaEC [38]. Also, `ksFrac` = 0.3 reproduced Q_OFF (Exp.: 75±5 W; Cal.: 78 W) of experimentations in Chapter 4, by the last two terms of the left-hand-side of Equation (5.18). Finally, the thermal efficiency η of the thermoacoustic engine is calculated as

$$\eta = \frac{\Delta W}{Q_\mathrm{in}}. \tag{5.19}$$

5.4 Experimental result and discussion

5.4.1 Stability curve

Figures 5.2 (a) and 5.2 (b) respectively present the critical temperature ratio for the looped tube engine and the straight tube engine. Here, the effective radius r_0 and the thermal diffusivity α at the spatial mean temperature of the regenerator are used to evaluate r/δ_α in the horizontal axis. The spontaneous oscillation frequency of both looped and straight engine are quantitatively agreed to the solution of ω_R given by $2\pi a/L$. The experimental critical temperature ratio ranged from 2.1 to 2.5 in the looped tube engine, whereas from 1.6 to 2.3 in the straight tube engine. The calculated critical temperature ratio showed a minimum for a given working gas in both engines. The minimum onset temperature ratios are achieved at $r/\delta_\alpha \approx 1.1$ for the looped engine and $r/\delta_\alpha \approx 1.9$ for the straight engine. The agreements between calculations and experimentations for the case of the straight tube engine filled with N_2 at the mean pressure of 0.6 MPa, the agreement was good; $T_\mathrm{H}/T_\mathrm{R} = 1.51$ by calculation and 1.65 by experiments for the regenerators of #40, and $T_\mathrm{H}/T_\mathrm{R} = 1.65$ by calculation and 1.77 by experiments for #50. In other conditions, however, the agreement is only qualitative, as reported in the cases for the regular flow channels in literatures [72, 73]. The relevant results are shown in Figures 5.3 and 5.4. Discrepancy between experimental and calculation results would indicate that the startup process of thermoacoustic oscillations are not yet fully understood by r_0, although previous Chapters 2 and 3 convince the applicability of r_0 for predicting the viscous loss and the thermoacoustic power production in small oscillation amplitude.

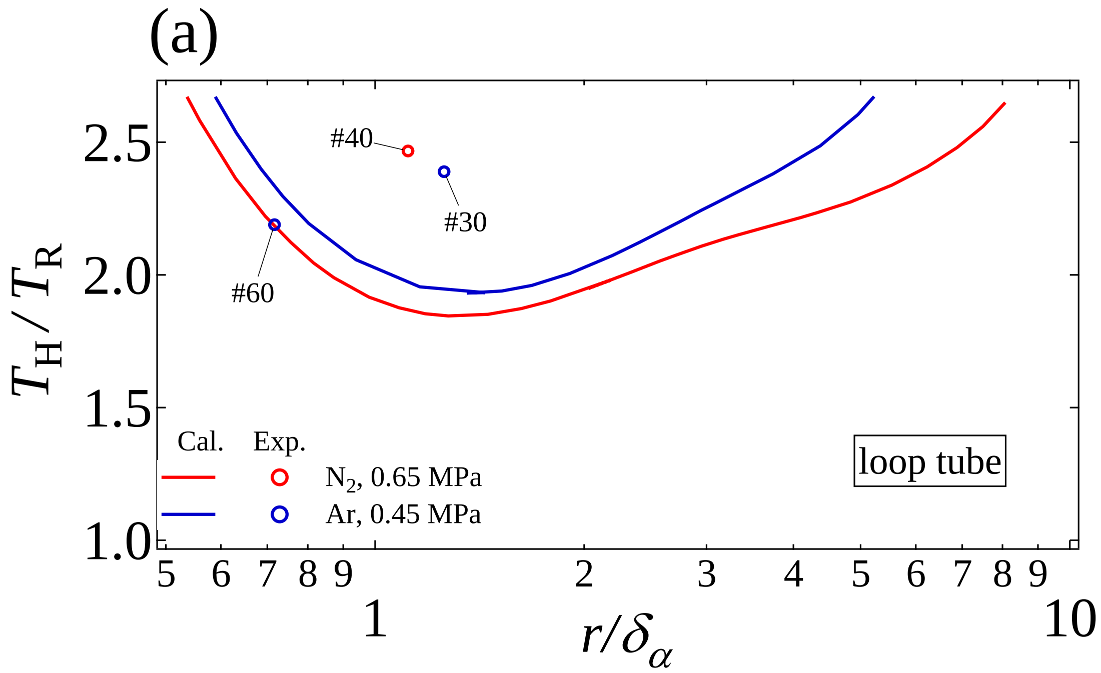

(a) Stability curve of the looped engine.

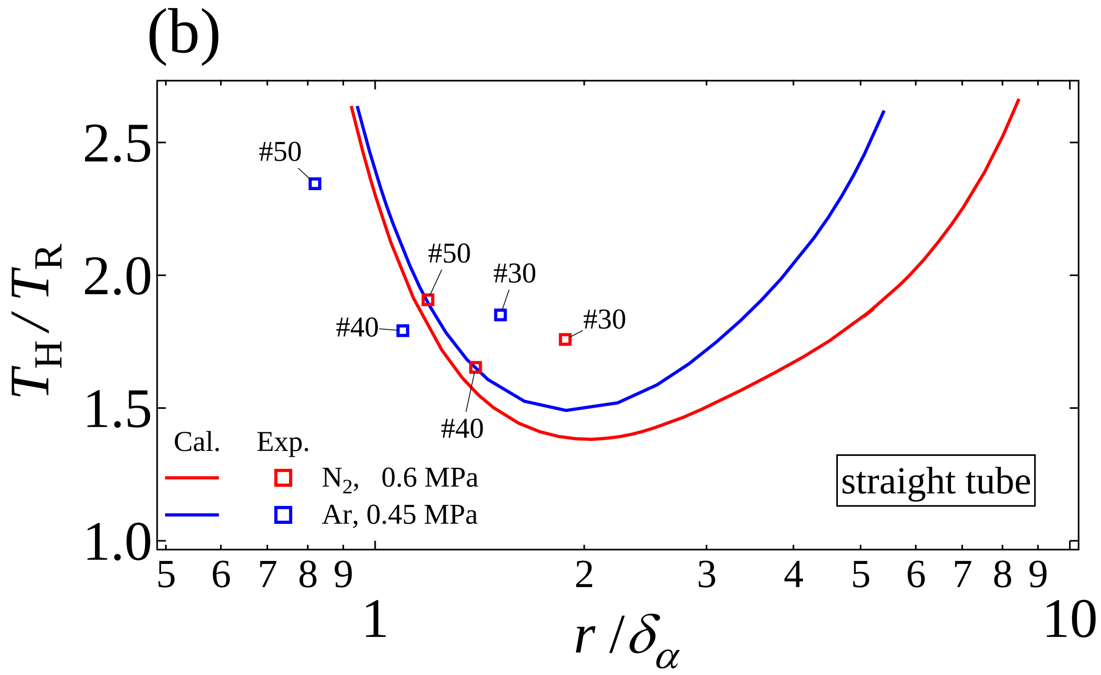

(b) Stability curve of the straight engine.

Figure 5.2: Comparisons of stability curves between experiments and calculations.

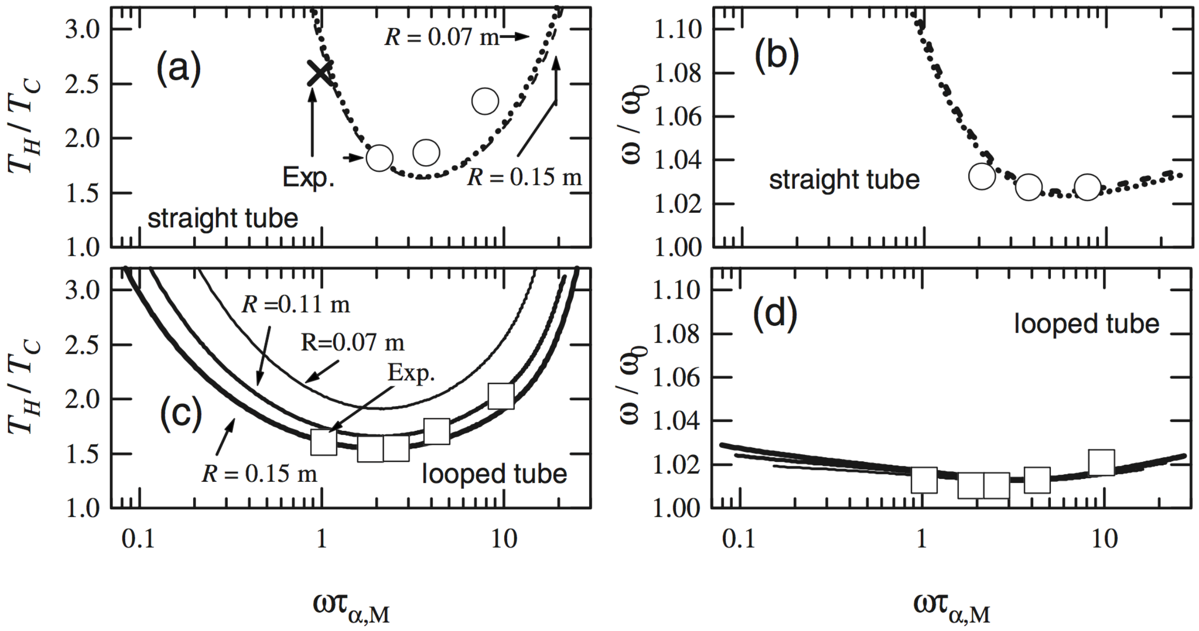

Figure 5.3: Comparisons of stability curves between experiments and calculations for the regular flow channel regenerator, reported by Ueda et al. [72].

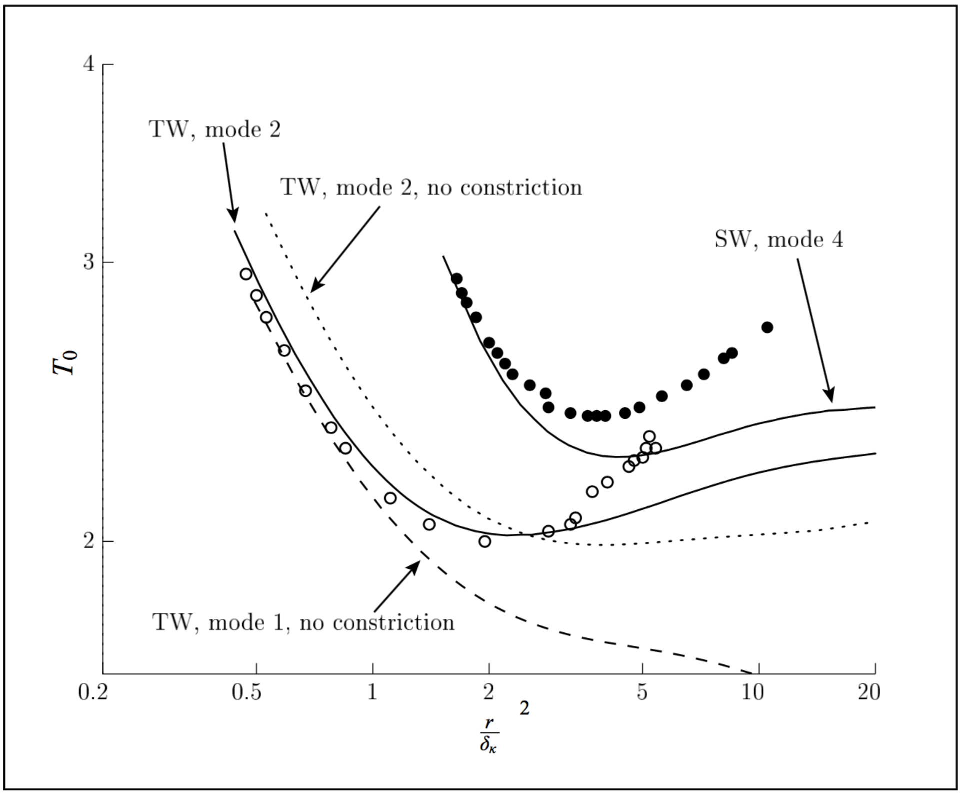

Figure 5.4: Comparisons of stability curves between experiments and calculations for the regular flow channel regenerator, reported by Guédra et al. [73].

5.4.2 Evolution of pressure amplitude

In this section, the relation between the pressure amplitude $|P|$ and the temperature difference across the regenerator ΔT are examined based on the experimental and calculation results. For the case of the loop tube engine tested in the working gases N_2 and Ar, experimental pressure amplitude at $x = 0.935$ m and the results of the calculation described in Subsection 5.3.3 using r_{eff} are plotted in Figure 5.5. Also, for the case of the straight tube engine tested in the working gas N_2, experimental pressure amplitude at $x = 0.155$ m and the results of the calculation using r_{eff} are plotted in Figure 5.6. In the figures, symbols and error bars are respectively represent the mean values and standard deviations obtained from the same experimental conditions repeated four times, whereas curves presents the calculation results.

As can be seen in Figure 5.6, both calculation and experiment results present a growth of pressure amplitudes when ΔT goes beyond the threshold temperature difference of the straight thermoacoustic engine. The result verifies the extension of the linear thermoacoustic theory to describe the nonlinear process due to the velocity-dependent flow resistance; if the velocity-independent effective radius r_0 is used, the amplitude becomes infinitely large without showing saturation behavior when $T_{\mathrm{H}}/T_{\mathrm{R}}$ exceeds the critical value. Therefore, use of r_{eff} is a great advancement from the previous calculation method.

The calculation results of looped tube are far from satisfactory, although the predicted amplitudes of the order of 10^3 Pa are in accordance with the measurements. It would be attributed to several nonlinear effects mentioned in Subsection 5.3.3 which are not considered in calculation transfer matrices of whole thermoacoustic engine system of the looped tube. In the case of the straight tube, the calculation results for #40 and #50 regenerators shows good agreement with the experimental results. The deviation of the calculation result of #30 regenerator would be attributable to the relatively larger error for the prediction of the onset of thermoacoustic instability.

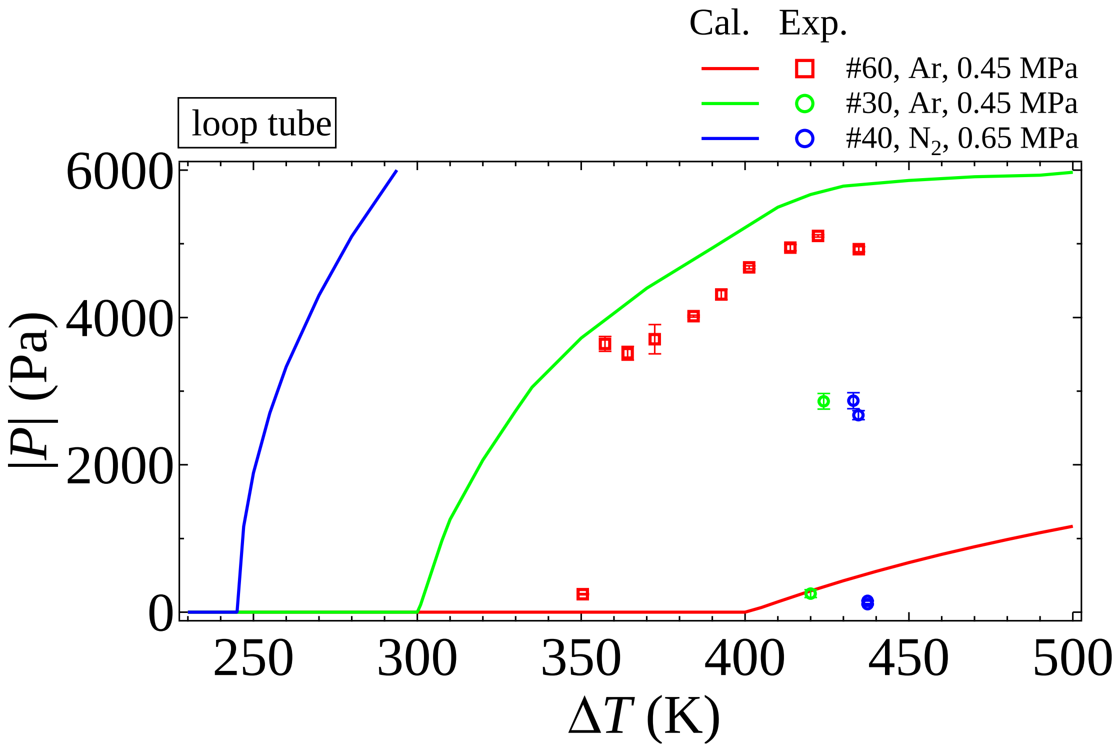

Figure 5.5: Growth of saturation pressure amplitude $|P|$ at $x = 0.935$ m of the loop tube engine as a function of the temperature difference ΔT.

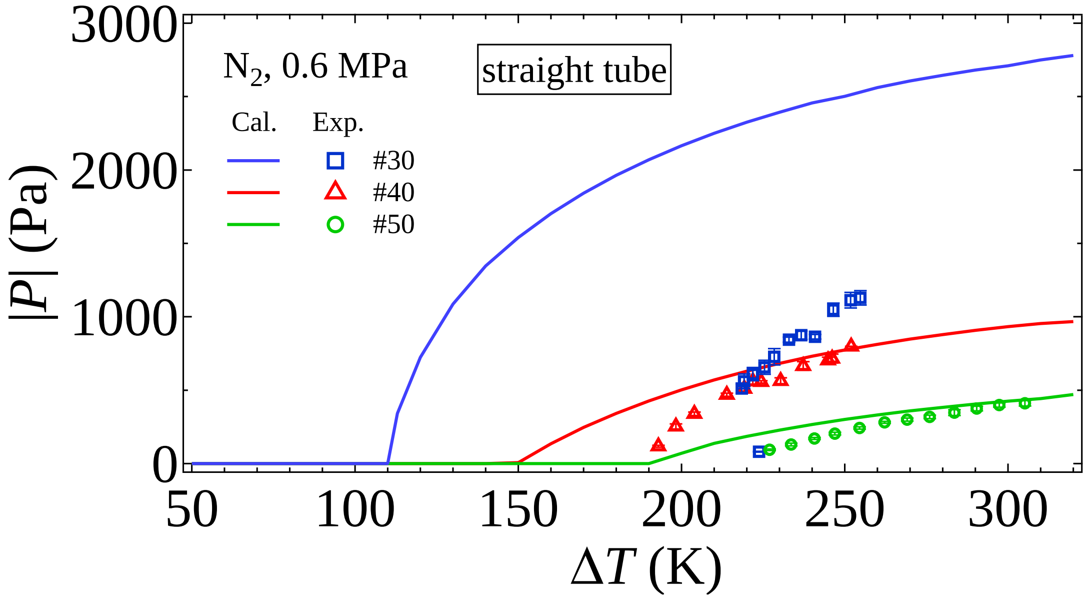

Figure 5.6: Growth of saturation pressure amplitude $|P|$ at $x = 0.155$ m of the straight tube engine as a function of the temperature difference ΔT.

5.4.3 Thermal efficiency of thermoacoustic engine and acoustic field

In the last subsection, the best agreement of the pressure evolution is presented in the case of #50 regenerator. For this particular case, the thermal efficiency $\eta (= \Delta W/Q_{\text{in}})$ vs the temperature difference ΔT across the regenerator is presented by Figure 5.7 for comparison between the experimental and calculation results. In Figure 5.7, η increases with increasing ΔT. Although the larger discrepancies are shown near the onset of the engine, good agreements are observed in the range of 280 K $< \Delta T <$ 310 K within maximum deviations < 30%.

Figure 5.8 illustrates acoustic field distributions in the straight thermoacoustic engine for the maximum value of the tested temperature difference of $\Delta T = 306$ K, where Figure 5.8 (a) shows distributions of oscillation amplitudes of $P(x)$ and $U(x)$ with solid line for measurements and dashed line for calculations, Figure 5.8 (b) presents the distribution of the specific acoustic impedance argument $\arg\left[Z(x)\right] = \arg\left[P(x)/U(x)\right]$, and Figure 5.8 (c) plots the distribution of the acoustic power $W(x) = \frac{1}{2}\left|P(x)\right|\left|U(x)\right|\cos\left\{\arg\left[Z(x)\right]\right\}$. Good agreements of oscillation amplitudes and the phase between calculations and measurements are presented, including a rapid increase of the velocity amplitude at the location of the regenerator. These results indicate that the calculation method using the transfer matrix of Equation (5.8) is applicable for the estimation of thermal efficiency and the acoustic field of the thermoacoustic engine equipped with the stacked-screen regenerator if the effective radius r_{eff} is used to describe the regenerator.

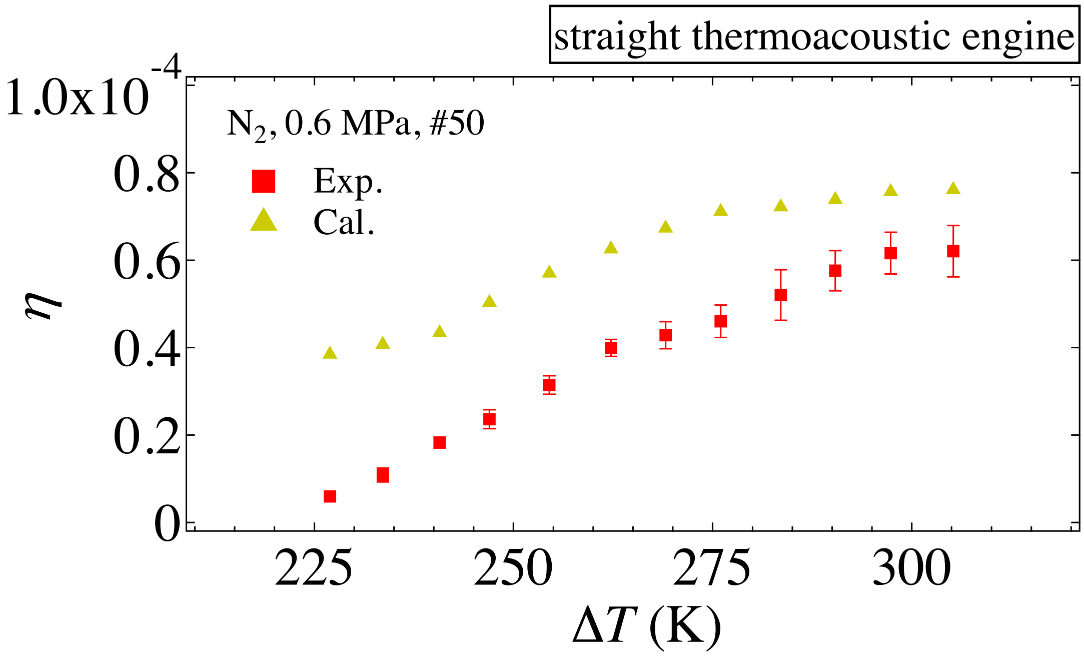

Figure 5.7: Thermal efficiency determined by experiments and calculation.

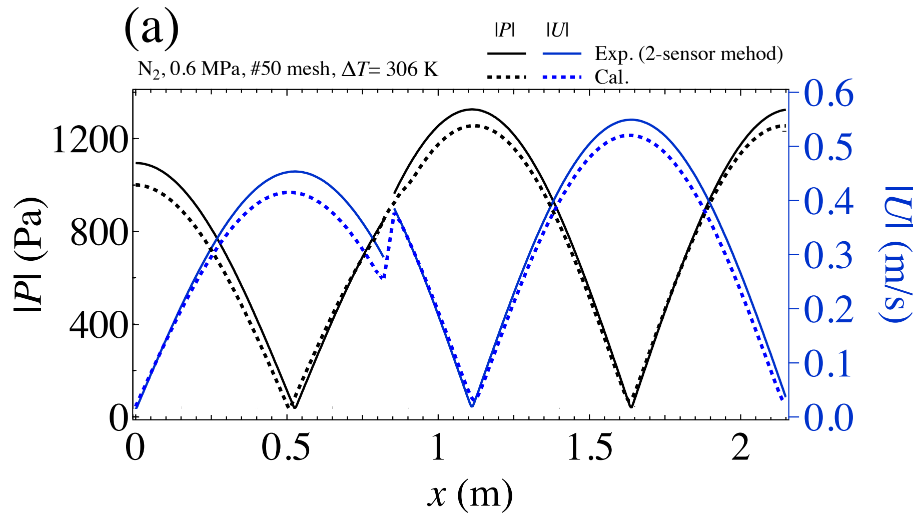

(a) Oscillation pressure and velocity distributions

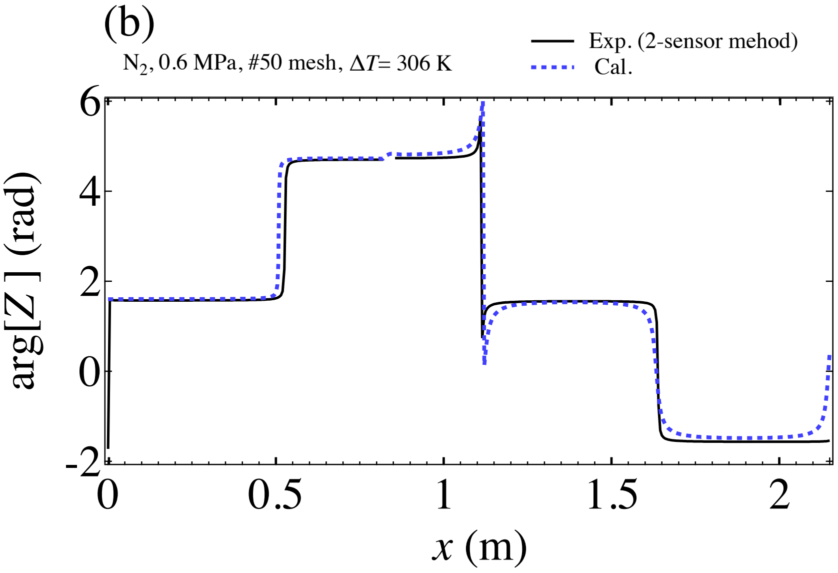

(b) Specific acoustic impedance argument distribution

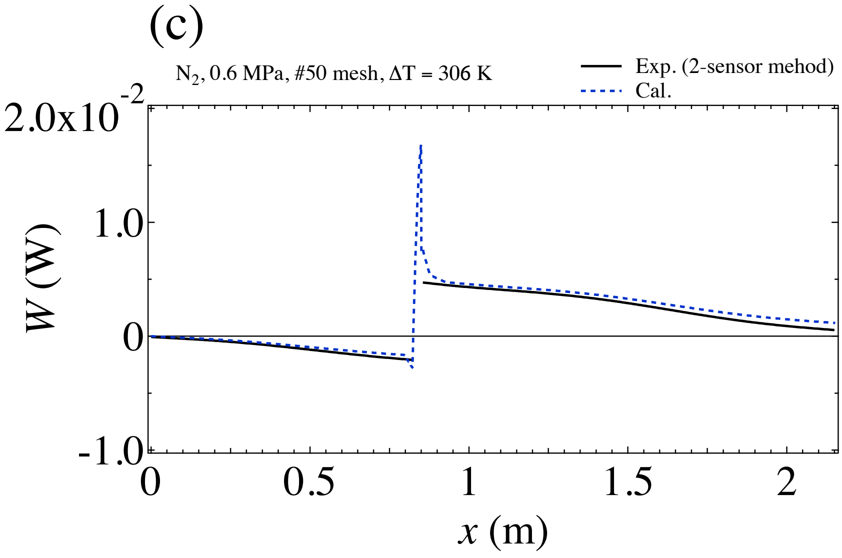

(c) Acoustic power distribution

Figure 5.8: Comparisons of acoustic field distribution between experimentations and calculations for the Standing wave thermoacoustic engine.

5.4.4 Discussion

The thermoacoustic calculation code DeltaEC [38] developed by Ward, Clark, and Swift has been used in the thermoacoustic community for engine design. It utilizes empirical formulations of Equations (2.7) and (4.6) respectively for the flow resistance and temperature oscillation to formulate a set of equations of momentum, energy, and mass conservation in order to characterize the stacked-screen regenerator. As mentioned in previous chapters, r_{eff} and r_0 predict ΔW and Q more accurately than empirical formulations of Swift and Ward. DeltaEC would be improved to give better estimations of the performance of thermoacoustic devices equipped with the stacked-screen regenerator if the effective radii concluded in this thesis is used.

Furthermore, r_{eff} can be used to significantly modify the transfer matrix method [72, 61, 60, 87–90]. Although the critical temperature ratio was evaluated for various thermoacoustic engines, and even the design of thermoacoustic engines were attempted using the transfer matrix method, estimation of the saturation amplitude at the steady oscillation state and hence the thermal efficiency is difficult in principle, because this method is basically a linear analysis. If one uses the velocity-dependent effective radius r_{eff}, the engine performance can be deduced as described in the previous subsections.

Some calculation algorithm conduct the iteration process of "guesses and targets" until certain boundary conditions or criteria are satisfied [38, 88]. In contrast to such methods, the method presented in this study provides an intuitive and simple numerical calculation method, which should save the calculation time required for the convergence.

5.5 Conclusions

To verify effective radii of r_0 and r_{eff} for the practical engine design, performances of two thermoacoustic engines of the looped tube and the straight tube equipped with the stacked-screen regenerators were experimentally obtained. The critical temperature ratio of thermoacoustic instability, saturation pressure amplitude, thermal efficiency, and acoustic field distributions were determined. The numerical calculation was proposed, which estimated the acoustic fields above the critical temperature ratio, in addition to the critical temperature ratio itself. Calculations gave good agreement in the case of stacked-screen regenerators of #50 and #40 mesh numbers tested in the straight thermoacoustic engine filled with N_2. Therefore, we consider that the conventional design method of thermoacoustic engine would be improved by using the effective radii r_{eff} and r_0.

Chapter 6

Conclusions and recommendations for future work

The experimental study presented in this thesis aimed at a better understanding of the stacked-screen regenerator which plays a critical role of the energy conversion in the thermoacoustic engine. In this chapter, the individual chapters are concluded in Sections 6.1–6.4, and a outlook of this research topic is provided in the last section for recommendations of further research.

6.1 Acoustic power dissipation with uniform temperature

The flow viscous resistance of the regenerator was measured in forced oscillatory flows with helium and argon gases at the mean pressure 0.45 MPa, from 20 to 100 Hz. In contrast to the Stirling engine studies which characterized the viscous effect by merely measuring pressures drop across the regenerator, the flow viscous resistance was experimentally determined from the acoustic power difference across the regenerator located at an acoustic field of the specific impedance close to $\rho_\mathrm{m}a$ with the uniform room temperature, where ρ_m stands for time-averaged density of the working gas and a signifies the adiabatic sound speed. Various regenerators made of stacked mesh screens were tested, and the velocity dependence of the flow resistance measurements was observed, whereas the regular channel regenerator showed a constant flow resistance against the velocity. The flow resistance of stacked-screen regenerator tested in a single oscillation frequency was proportional to the spatial mean velocity amplitude of the regenerator region, and varied with mesh numbers. The dependences of velocity and mesh number were organized with two non-dimensional ratios of Re_h and r_0/δ_ν, where Re_h is the Reynolds number, r_0 is the effective radius of Ueda et al., and δ_ν is the viscous penetration depth. The results were well characterized by the empirical equation of Obayashi et al., although the equation was originally obtained from experiments using air at atmospheric pressure as the working gas. Thus, the wide applicability to various gases of He, Ar, and air was ascertained by this study. The measured flow resistance were also compared with other two empirical equations respectively proposed by Swift & Ward and Gedeon & Wood, whose equations respectively aimed at thermoacoustic and

Stirling engines. Both of them presented the worse agreements than the Obayashi's empirical equation.

6.2 Effective radius

A capillary-tube-based modeling, assuming the tortuous pores by a bundle of cylindrical tubes, was applied to the stacked-screen regenerator. The empirical equation of Obayashi et al. parameterized by Re_h and r_0/δ_ν was converted to the expression for the effective radius r_eff. In order to verify the validity of r_eff, the differentially heated regenerators were experimented in oscillatory flow using helium and argon gases at the mean pressure 0.45 MPa, with changing the velocity amplitude and the oscillation frequency. The measured acoustic fields at both ends of the regenerator were used to estimate the experimental radius, and compared with the proposed r_eff. The result indicated that the cylindrical modeling was capable of describing the stacked-screen regenerator with and without the temperature gradients, as the effective radius r_eff well agreed with the experimentally determined one. Therefore, the effective radius derived from the flow resistance was concluded to adequately characterize the thermoacoustic power production conducted in the stacked-screen regenerator.

6.3 Heat transportation by oscillation flow

The oscillation-induced heat flow transmitted through the differentially heated regenerator was measured in forced oscillatory flow with argon gas at the mean pressure of 0.45 MPa. Stacked-screen regenerators made of five different mesh numbers of and one regular pore regenerator were tested. Measurements were conducted with keeping a constant temperature difference of 250 K and the specific impedance around $0.3\rho_\mathrm{m}a$. The velocity amplitude was the main experimental parameter. Experimental results on the stacked-screen regenerator was compared with four different empirical equations derived from: (1) the effective radius of Ueda et al. based on measurements of the characteristic wavenumber and impedance of acoustic propagation through the stacked-screen regenerator with the uniform temperature, (2) oscillating temperature formulation derived from steady flow data of Kays and London with a simple harmonic analysis by Swift and Ward, (3) Nusselt-Reynolds number correlation proposed by Tanaka et al. conducted the oscillatory flow experiments of maximum 10 Hz, and (4) Nusselt-Reynolds number correlation given by Gedeon and Wood for direct Stirling engine design which was proposed from the oscillatory flow of maximum 120 Hz. The effective radius of Ueda et al. r_0 was concluded as the formulation that was able to give essentially the same heat flow with the simplest formulation without using Nusselt number. Additionally, comparison with the effective radius r_eff was made with respect to both the acoustic field and the axial heat transport. The results showed that two effective pore radii of r_0 and r_eff were necessary to account for the heat transport and the acoustic field, respectively.

6.4 Usage of imaginary oscillation frequency

The calculation method of the onset temperature and the oscillation amplitude saturation was proposed such as the critical temperature ratio of thermoacoustic engines. For verifying the method, two thermoacoustic engines of the looped type and straight type with the same length were built and tested. Performances of the thermoacoustic engines, such as the thermoacoustic instability, the evolution of pressure amplitude, thermal efficiency, and acoustic field distributions, were compared with the calculation results. Good agreements were achieved in the cases of the standing wave engine filled with the pressurized nitrogen gas and equipped with two regenerators respectively stacked with mesh screens #40 and #50. The result guarantees the applicability of the proposed method. However, poor agreements were obtained in the looped thermoacoustic engines and in the standing wave engine with #30 mesh screens, which were attributed to a high specific acoustic impedance in the location of the regenerator.

6.5 Outlook

In this study, the viscous dissipation (Chapter 2), thermoacoustic power production (Chapter 3), oscillation-driven heat flow (Chapter 4) caused by the stacked-screen regenerator were clarified by experimental investigations, and characterized by the effective radii of r_{eff} and r_0. Under the framework of the thermoacoustic theory, using two effective radii to determine the onset temperature and the oscillation amplitude saturation for the thermoacoustic engine system was also proposed (Chapter 5). However, there are still some issues to be continuously investigated in the stacked-screen regenerator for practical thermoacoustic engine design.

The detail study of the traveling wave engine [76] designed by Backhaus and Swift [19] has reported that the spontaneous oscillation of the engine induces the velocity amplitudes at the ambient end of the regenerator with 0.53~2 m/s while the specific acoustic impedance at the location of the regenerator is about 30 times $\rho_{\mathrm{m}}a$. In such acoustic fields of large velocity amplitudes as well as high acoustic impedances at the location of the stacked-screen regenerator, the thermal-relaxation loss is supposed to become comparable to the viscous loss. Still, the loss due to thermal conductivity between gas and solid walls of tortuous flow channels made of stacked mesh screens remains still unclear.

Chapter 4 reported that the heat flow under the condition of negligibly small heat flow component Q_{A}. This heat flow Q_{A} can become also considerably high when the regenerator imposed by a large velocity amplitude with a high acoustic impedance. So it should be studied further.

Also, notably hydrodynamic/thermal entrance effects (vortex shedding [91], transitional turbulence [92], and nonlinear temperature fluctuations [93]) occurring at the ends of the regenerator or stack with regular pores have been reported theoretically and experimentally. The complexity of those phenomena is not very well understand in the case of the stacked-screen regenerator with complex flow channels. Furthermore, acoustic streaming directly brings about unsteady heat and mass transfer passing through the regenerator. Characterization of these nonlinear phenomena is future challenges of experimental investigations.

The experimental setup in this study has been developed for broad ranges of the oscillation frequency and velocity with acoustic fields of low impedances. It should be improved to generate the large velocity amplitude with high acoustic impedances for investigating the thermal-relaxation loss and the compression-driven heat flow induced in the stacked-screen regenerator. Meanwhile, development of an optical technique enabling direct measurement for those nonlinear phenomena relating to the regenerator termination is urgent.

Appendix A

Experimental investigation of stacked-screen regenerator located in a high impedance acoustic field

A.1 Introduction

A thermoacoustic Stirling heat engine developed by Backhaus and Swift attained a high thermal efficiency of 30 %, equivalent to 41 % of the Carnot efficiency [19], which is comparable to the efficiency of conventional internal combustion engines. They attributed such a high efficiency to the stacked-screen regenerator which satisfies two conditions: the thermodynamic Stirling cycles conducted by oscillation gas parcels through excellent thermal contacts with the mesh screens, and a low viscous dissipation realized with a high specific acoustic impedance of 15-30 times of $\rho_{\mathrm{m}}a$ at the regenerator position. So far, the flow resistance and the axial heat transport in the stacked regenerator were investigated in the acoustic fields with $|Z| \approx \rho_{\mathrm{m}}a$, where Z is the specific acoustic impedance. It would be worth to test the performance of the stacked screen regenerator in the acoustic field with a high acoustic impedance for the development of thermoacoustic engine with high thermal efficiency.

There is another reason to study the stacked screen regenerator with the elevated acoustic impedance. In Chapter 5, certain deviations between calculations and experiments of the onset temperature ratio were observed in cases of the coarse mesh screens. Because the onset of thermoacoustic oscillations is triggered by an extremely small fluctuation when the thermoacoustic power production overtakes acoustic power dissipations, it is possible that unknown effects exist in the second term of the right hand side of Equation (2.2) expressed as

$$\frac{dW}{dx} = \frac{1}{2}A\mathrm{Re}\left[\widetilde{U}\frac{dP}{dx}\right] + \frac{1}{2}A\mathrm{Re}\left[\widetilde{P}\frac{dU}{dx}\right], \tag{A.1}$$

as its contribution was neglected in Chapter 2 yet not fully clarified in Chapter 3, in which the specific acoustic impedance was tuned as $Z \approx \rho_{\mathrm{m}}a$ at the location of the regenerator. In the

Equation, W is the acoustic power, A is the cross-sectional area of the flow channel, P and U respectively denote the complex amplitude of pressure and cross-sectional averaged velocity, $\mathrm{Re}\,[\cdots]$ means taking the real part, and $\widetilde{\cdots}$ stands for taking the complex conjugate.

The velocity gradient dU/dx in Equation (A.1) is expressed for a regular flow channel by the thermoacoustic theory of Equation (1.6) which is given as

$$\frac{dU}{dx} = -i\omega\frac{\left[1+(\gamma-1)\chi_\alpha\right]}{\gamma P_\mathrm{m}}P + \frac{\chi_\alpha-\chi_\nu}{(1-\chi_\nu)(1-\sigma)}\frac{1}{T_\mathrm{m}}\frac{dT_\mathrm{m}}{dx}U, \tag{A.2}$$

where ω denotes the oscillation angular frequency, γ and σ respectively signify the ratio of specific heats and Prandtl number, and P_m and T_m respectively stand for the time-averaged pressure and temperature. In the equation, $\chi_\sharp(\sharp = \nu, \alpha)$ are the thermoacoustic functions of the viscous (ν) and thermal (α) effects, which are given by Equations (5.5) or (5.7) depending on shape types of the regular flow channel. Inserting dP/dx of Equation (1.1) of the momentum and dU/dx above into Equation (A.1) gives

$$\frac{dW}{dx} = -\frac{1}{2}AR_\nu\,|U|^2 - \frac{1}{2}\frac{1}{R_\mathrm{P}}\,|P|^2 + \frac{1}{2}A\mathrm{Re}\,[\mathbb{G}]\,|P|\,|U|\cos\theta, \tag{A.3}$$

In the equation, the first term was derived from the momentum equation as already shown in Chapter 2, and the second term represents the thermal-relaxation dissipation caused by the non-uniformity of pressure-induced temperature oscillations in the cross-section of the flow channel, whereas the third term stands for the thermoacoustic power production when the temperature gradient is imposed on the flow channel. The factors $1/R_\mathrm{P}$ and $\mathbb{G}$ are respectively given as

$$\frac{1}{R_\mathrm{P}} = \frac{\gamma-1}{\gamma}\frac{\omega A\mathrm{Im}\left[-\chi_\alpha\right]}{P_\mathrm{m}} \quad \text{and} \tag{A.4}$$

$$\mathbb{G} = \frac{\chi_\alpha-\chi_\nu}{(1-\chi_\nu)(1-\sigma)}\frac{1}{T_\mathrm{m}}\frac{dT_\mathrm{m}}{dx}. \tag{A.5}$$

Considering the regenerator placed in a pipe, and the relationship between velocities U in the pipe region and V in the regenerator region with $AU = A\phi V$ (ϕ is the volume porosity of the regenerator.) as shown in Figure 2.5, the acoustic power difference ΔW across the regenerator of the length l can be given by

$$\Delta W \approx W_\nu + W_\mathrm{P} + W_\mathrm{T}, \tag{A.6}$$

with

$$W_\nu = -\frac{l}{2}A\phi R_\nu |V|^2, \tag{A.7}$$

$$W_\mathrm{P} = -\frac{l}{2}\frac{1}{R_P}|P|^2, \text{ and} \tag{A.8}$$

$$W_\mathrm{T} = \frac{l}{2}A\phi \mathbb{G}|P||V|\cos\theta, \tag{A.9}$$

where W_ν and W_P respectively denote the viscous and the thermal-relaxation power dissipation resulted from R_ν and $1/R_\mathrm{P}$. In the equation, W_T stands for the thermoacoustic power production/dissipation associated with g. For the stacked-screen regenerators, experimental investigations of W_P and W_T are still few at the moment. This appendix experimentally investigates the acoustic power difference ΔW across the stacked-screen regenerator by focusing on $1/R_\mathrm{P}$.

A.2 Experimental procedure

The experimental setup is the same as those used in the experiments of Chapters 2 and 3, as shown in Figures 2.2 and 3.1. The regenerator was made of randomly stacked stainless-steel wire mesh screens with a mesh number of 100, a wire diameter d_w =0.1-mm and volume porosity of ϕ =0.69. The hydraulic diameter of stacked wire mesh screens is 0.22-mm. The regenerator was sandwiched by the fin-type hot heat exchanger and ambient heat exchanger and positive temperature gradient was imposed by them. The hot heat exchanger having the cartridge electrical heater inside was connected with a regenerator holder and a thermal buffer tube. The cooling water circulated the ambient heat exchanger and one end of the thermal buffer tube to maintain the room temperature (293 K). Type-K thermocouples were used to measure the temperatures at the centers of the hot and cold surfaces of the regenerator for determining T_H and T_R. The temperature difference $\Delta T (= T_\mathrm{H} - T_\mathrm{R})$ between the ends of the regenerator was changed from 0 K to 250 K with every 50 K, by adjusting electrical power to the cartridge heater. The working gas contained in the tube was either Ar or He gas with a mean pressure of 0.45 MPa. Loudspeaker pairs located at ends of the cylindrical tube introduced acoustic oscillations of the gas in the experimental setup. The acoustic field of $P(x)$ and $U(x)$ in the cylindrical tube was monitored by two pairs of pressure transducers mounted on the sidewall of the cylindrical tube, and determined with the two-sensor method [58, 59]. From the measured $P(x)$ and $U(x)$, the acoustic power difference across the regenerator $\Delta W = W_2 - W_1$ was determined in the various experimental conditions of the temperature difference ΔT and the specific acoustic impedance $Z = P/U$, where the subscripts 1 and 2 denote the positions of cold and hot end of the regenerator in the same way as the previous chapters.

In the first experiment of this appendix, The regenerator was tested in the acoustic field with the impedance ranging from $\rho_\mathrm{m}a$ to $50\rho_\mathrm{m}a$, while keeping the spatial average velocity amplitude $|V|$ at a constant value; $|V|$ was 0.02 m/s for Ar and 0.05 m/s for He. These small velocity amplitudes were chosen to make the viscous dissipation as small as possible. Because of the

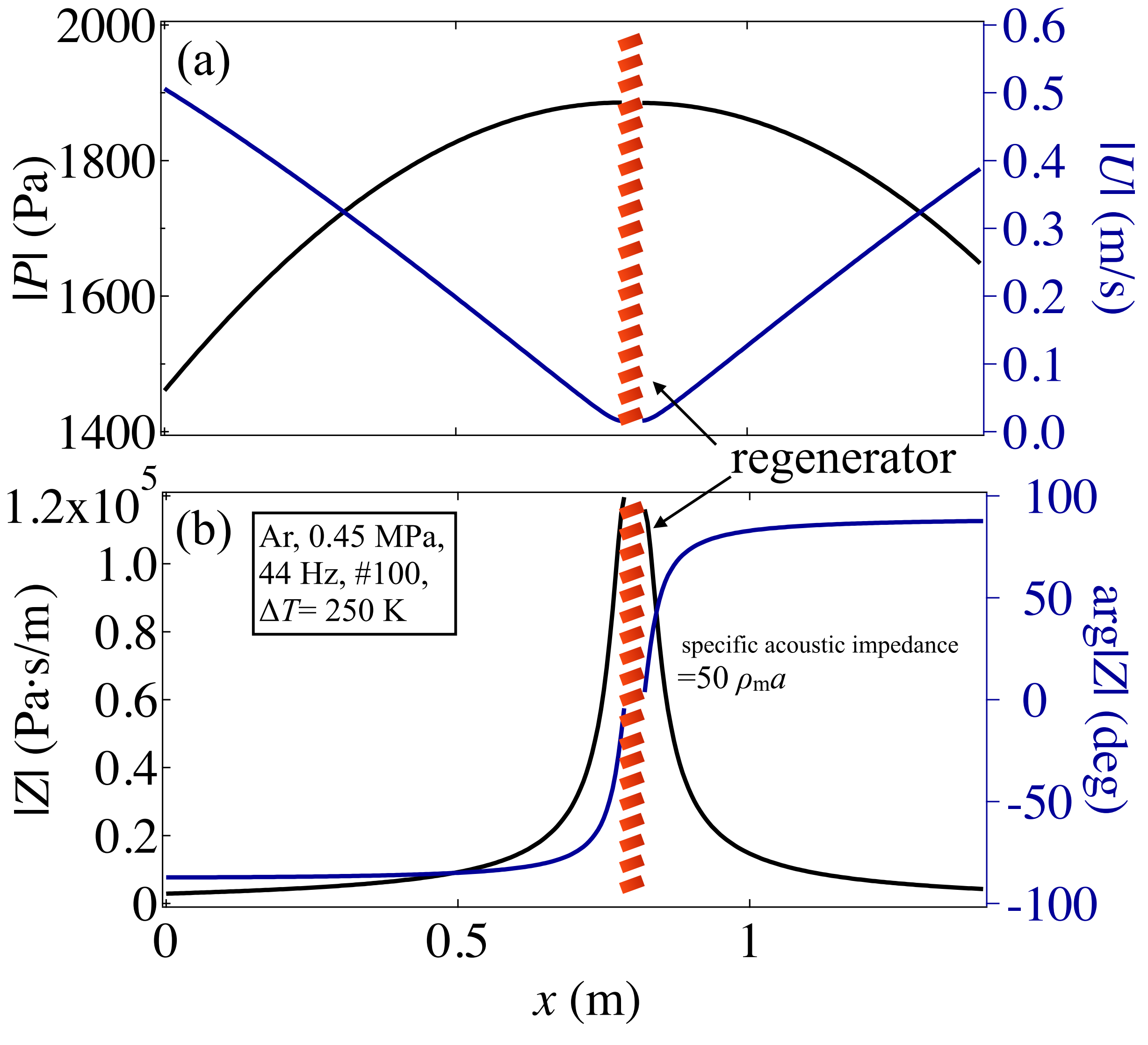

Figure A.1: Measured acoustic field with #100 mesh, 44 Hz, $\Delta T = 250$ K, and argon gas. In (a), the black curve represents the pressure amplitude $|P|$, whereas the blue curve represents the radial averaged velocity amplitude $|U|$. In (b), the black curve represents the magnitude $|Z|$, and the blue curve presents the phase $\arg[Z]$

relatively small velocity amplitude, the velocity-dependent effective radius r_{eff} hardly changes from r_0, as can be seen from Figures 3.6 and 3.7 of Chapter 3.

Figure A.1 shows an example of experimental acoustic fields of the high specific acoustic impedance $50\rho_{\mathrm{m}}a$, where the regenerator was placed at the pressure maximum. Throughout the study of this appendix , the phase difference between pressure and velocity $\theta = \arg[Z]$ was adjusted to become close to zero in the outlet side of the regenerator.

In the second experiment, the velocity dependence of W_{P} is addressed. For this purpose, the uniform temperature regenerator was tested at a constant acoustic impedance but with changing the oscillation amplitude. From the measured acoustic power decrease ΔW (without W_{T}) across the regenerator, the experimental W_{P} was estimated from $\Delta W - W_{\nu}$, where W_{ν} was calculated from Equation (A.7) whose R_{ν} is estimated by using the empirical flow resistance formulation of Obayashi et al. of Equation (2.9). Based on Equation (A.8), the experimental $1/R_{\mathrm{P}}$ was then obtained as

$$\frac{1}{R_{\mathrm{P}}} = -\frac{2W_{\mathrm{P}}}{l\left|P_{\mathrm{ave}}\right|^2}, \tag{A.10}$$

where $\left|P_{\mathrm{ave}}\right|$ (= $\left|P_1 + P_2\right|/2$) is the spatial mean pressure amplitude in the regenerator region.

A.3 Experimental results and discussion

A.3.1 Constant velocity amplitude

Experimental results of the acoustic power difference ΔW are plotted by symbols in Figures A.2 and A.3 for Ar and He gases, respectively. The oscillation frequency was 44.0 Hz. The horizontal axis is $\left|Z_{\mathrm{ave}}\right|/\left(\rho_{\mathrm{m}}a\right)$, which means the magnitude of the spatial averaged acoustic impedance $\left|Z_{\mathrm{ave}}\right|$ (= $\left|Z_1 + Z_2\right|/2$) normalized with respect to the characteristic acoustic impedance $\rho_{\mathrm{m}}a$. Because the velocity amplitude is constant in present experiments, $\left|Z_{\mathrm{ave}}\right|/\left(\rho_{\mathrm{m}}a\right)$ varied through the pressure amplitude $|P|$ at the regenerator position. So, Figures A.2 and A.3 can be seen as the pressure amplitude dependence of ΔW.

In the case of the uniform temperature regenerator ($\Delta T = 0$), the measured ΔW was always negative, which means the occurrence of acoustic power dissipation in the regenerator. For comparison, the sum of W_{ν} and W_{P} estimated by inserting $|V|$ and $|P|$ into Equations (A.7) and (A.8) (using the relationship of $P = ZU$) are shown in Figures A.2 and A.3 by solid curves. Here, by assuming the effective radius r_0 of Ueda et al., R_{ν} was obtained from Equation (2.4) and $1/R_{\mathrm{P}}$ from Equation (A.4). Although the calculated W_{P} changes in proportional to $|P|^2$, its contribution is so small that the curves in Figures A.2 and A.3 are presented almost as horizontal lines, with small offsets corresponding to the viscous dissipation W_{ν}. Although we have reported that r_0 provides good predictions of R_{ν} for small $|V|$, discrepancies between the solid curves and the experimental results are obvious and increases with $\left|Z_{\mathrm{ave}}\right|$. This result indicates that the factor $1/R_{\mathrm{P}}$ obeys the different mechanism from R_{ν}.

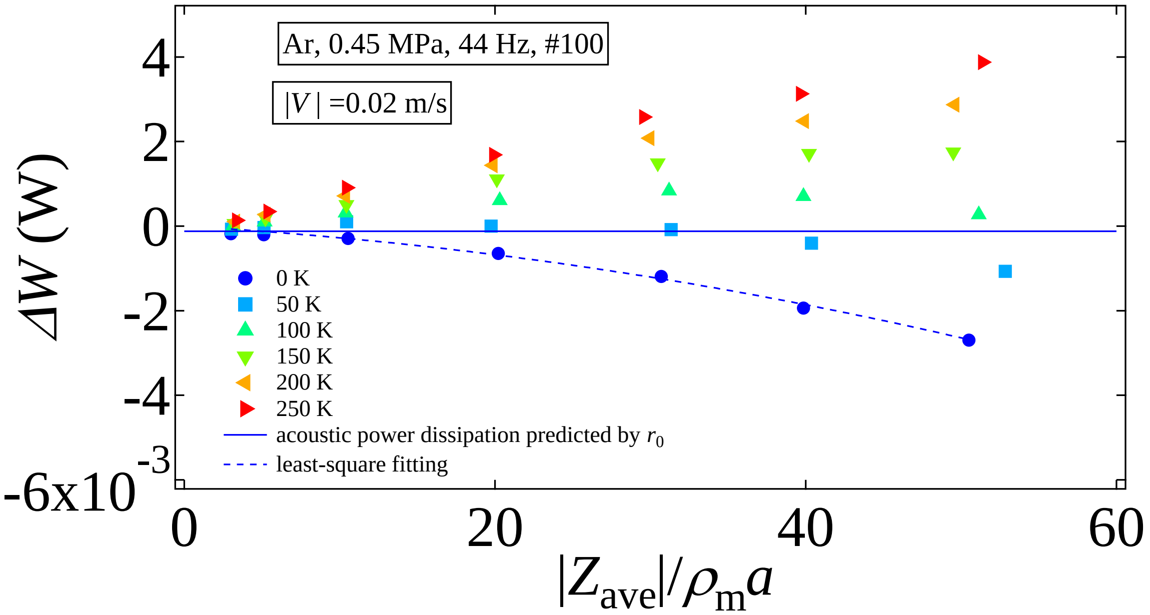

Figure A.2: Experimental results of ΔW in the case of Ar. The velocity amplitude was kept at 0.02 m/s. Colors represent the temperature difference ΔT of the regenerator. (Figure adapted from Reference 94 and modified by author.)

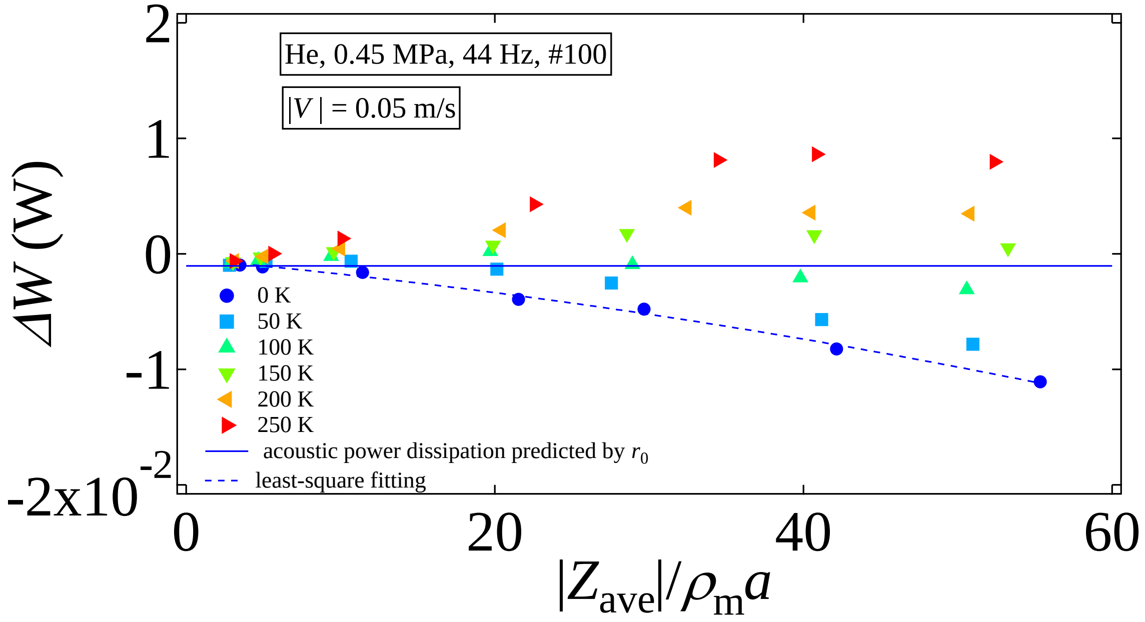

Figure A.3: Experimental results of ΔW in the case of He. The velocity amplitude was kept at 0.05 m/s. Colors represent the temperature difference ΔT of the regenerator. (Figure adapted from Reference 94 and modified by author.)

In the case of the regenerator with positive temperature differences, the measured ΔW can become positive, showing the thermoacoustic power production with a sufficiently high ΔT values. In order to extract the contribution of W_{T} from ΔW with $\Delta T \geq 0$, the experimental ΔW with $\Delta T = 0$ was fitted to a curve $\Delta W = e_1 \left(|Z_{\mathrm{ave}}|/\rho_{\mathrm{m}}a\right)^2 + e_2 \left(|Z_{\mathrm{ave}}|/\rho_{\mathrm{m}}a\right) + e_3$, (= $W_\nu + W_{\mathrm{P}}$, estimated from least-square fitting). The fitting results are shown by the dashed curves in Figures A.2 and A.3, and the coefficients e_1, e_2, and e_3 are tabulated in Table A.1.

Table A.1: Coefficients of polynomial fit.

Working gas	e_1	e_2	e_3
Ar	-0.79×10^{-6}	-1.15×10^{-5}	-1.15×10^{-4}
He	-1.36×10^{-6}	-1.20×10^{-5}	-4.23×10^{-4}

The contribution of the temperature difference to the acoustic power production, W_{T}, is obtained by $W_{\mathrm{T}} = \Delta W - (W_\nu + W_{\mathrm{P}})$, namely by subtracting ΔW with $\Delta T = 0$ from ΔW with nonzero ΔT. Figures A.4 and A.5 present W_{T} by symbols for Ar and He, respectively. Almost linear relationships between W_{T} and $|Z_{\mathrm{ave}}|/\left(\rho_{\mathrm{m}}a\right)$ plotted are observed. Furthermore, W_{T} is well reproduced by Equation (A.9) (using the relationship of $P = ZU$) by inserting the effective radius r_0 of Ueda et al. into $\mathbb{G}$ of Equation (A.5). Good agreements between experimental results and predictions gave the maximum deviation of 5 % and 14 % respectively for Ar and He. It reveals that the thermoacoustic power production W_{T} achieved by the stacked-screen regenerator is characterized by the effective radius r_0 given by Equation (2.10), although inserting the effective radius r_{eff} gives essentially the same results because of the small velocity amplitude of the experiments.

A.3.2 Constant acoustic impedance

This section further investigates the oscillation amplitude dependence of $1/R_{\mathrm{P}}$ of the uniform temperature stacked-screen regenerator, where $1/R_{\mathrm{P}}$ was obtained from W_{P} by using Equation (A.8). Figure A.6 shows $1/R_{\mathrm{P}}$ of the uniform temperature regenerator of #30 tested in pressurized Ar at 0.45 MPa of 100 Hz. In Figure A.6, the same $1/R_{\mathrm{P}}$ are shown in panels of A.6 (a) and A.6 (b) whose horizontal axes are respectively represented by spatial mean amplitude of pressure $|P_{\mathrm{ave}}|$ and velocity $|V|$. As can be seen in Figure A.6, the measured $1/R_{\mathrm{P}}$ of the stacked-screen regenerator dotted by symbols presents an oscillation amplitude dependence, although the results of the thermoacoustic theory provide the horizontal line that was given using Equation (A.4) and r_0. Moreover, comparing experimental data in panels of A.6 (a) and A.6 (b), $1/R_{\mathrm{P}}$ of the stacked-screen regenerator seems to be proportional to the velocity amplitude because the symbols fall onto a single lie with a constant slope in Figure A.6 (b).

$1/R_{\mathrm{P}}$ is further investigated with various oscillation frequencies and relatively low specific acoustic impedances of 9 and 5 $\rho_{\mathrm{m}}a$ with the larger velocity amplitude. But the velocity and the

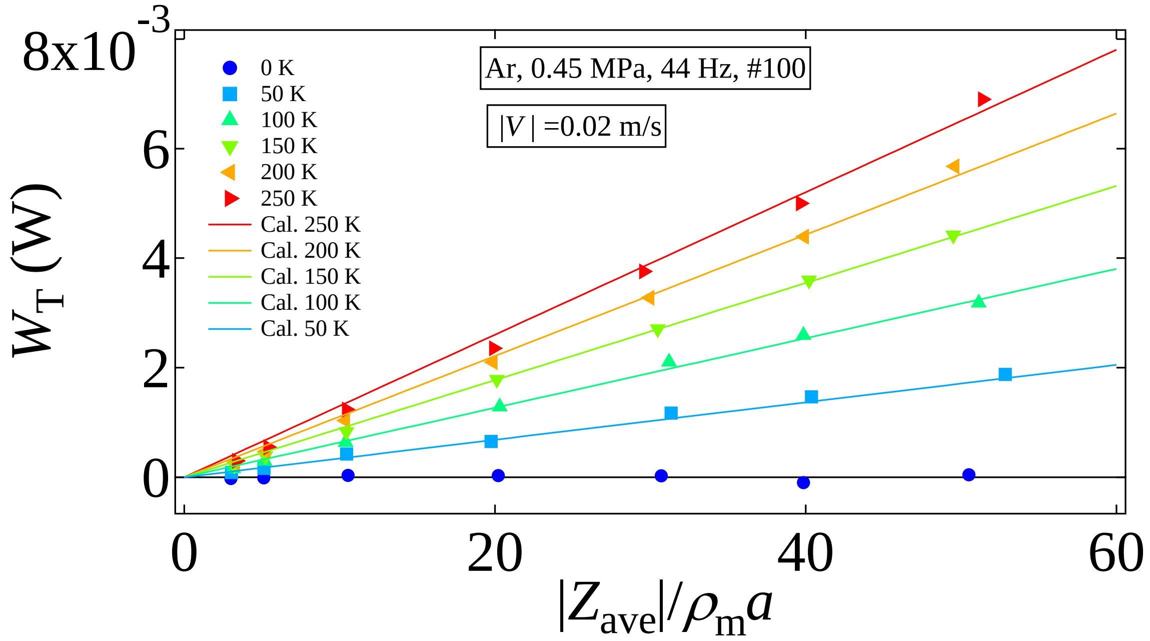

Figure A.4: Experimental results of W_T in the case of Ar. Colors represent the temperature difference ΔT of the regenerator. W_T represents the contribution of the temperature difference to the acoustic power production ΔW. (Figure adapted from Reference 94 and modified by author.)

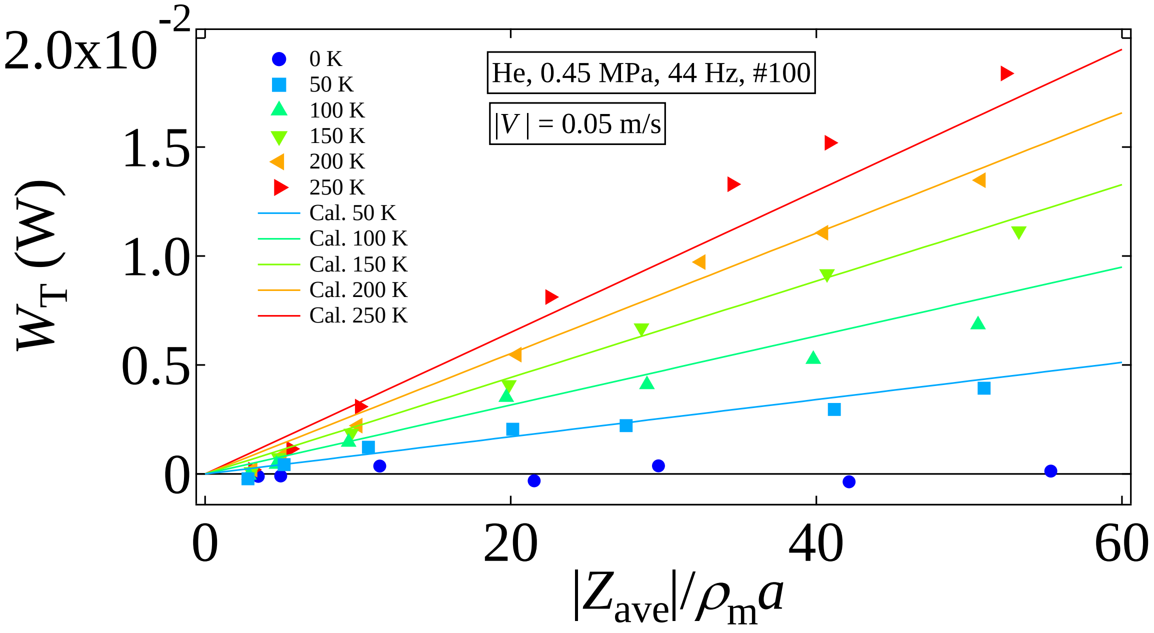

Figure A.5: Experimental results of W_T in the case of He. Colors represent the temperature difference ΔT of the regenerator. W_T represents the contribution of the temperature difference to the acoustic power production ΔW. (Figure adapted from Reference 94 and modified by author.)

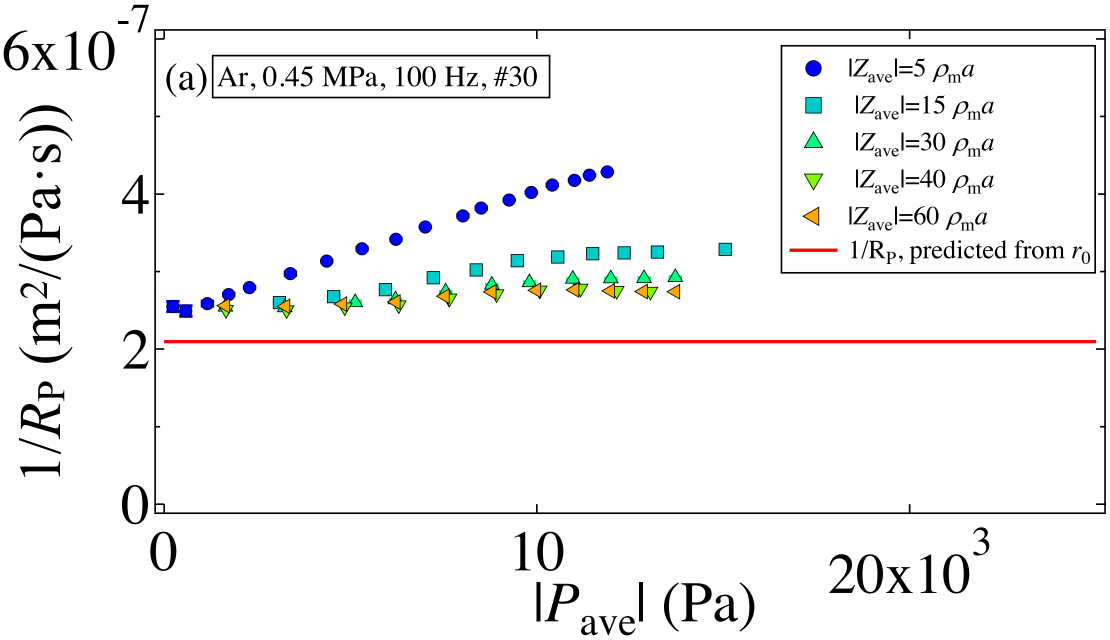

(a) Experimental results plotted in pressure amplitude.

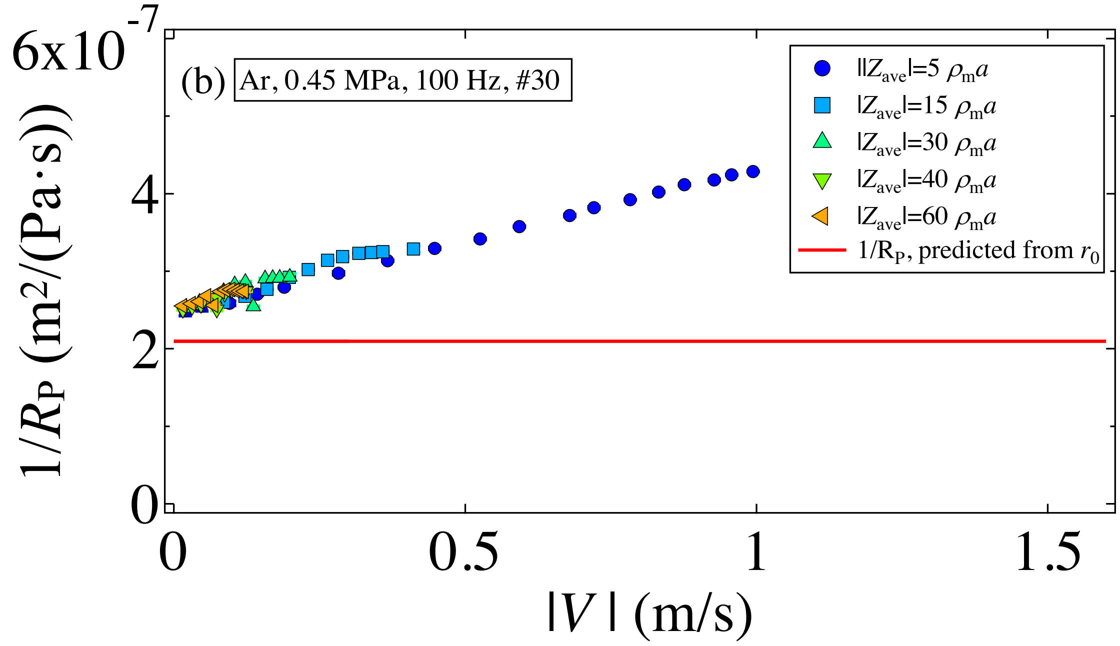

(b) Experimental results plotted in velocity amplitude.

Figure A.6: Experimental results of $1/R_\mathrm{P}$ tested with #30 regenerator. Panels (a) and (b) are plotted with identical measured data with respective horizontal axes of $\left|P_\mathrm{ave}\right|$ and $|V|$.

oscillation frequency are apparently responsible for the change of measured $1/R_{\mathrm{P}}$ values of #100 mesh experimented in pressurized Ar at 0.45 MPa, as shown in Figure A.8. The result presents a demand of an empirical equation parameterized by the dimensionless velocity and oscillation frequency for capturing the thermal-relaxation resistance of the stacked-screen regenerator at high acoustic impedance.

A.3.3 Discussion

Liu and Garrett [95] have analytically discussed the relation between Nusselt number and the thermoacoustic function, and provided a relation between Nu and χ_α in the case of the uniform temperature flow channel as follows:

$$\dot{\chi}_\alpha = \frac{Nu}{\frac{i}{8}\left(\frac{d_{\mathrm{h}}}{\delta_\alpha}\right)^2 + Nu}, \tag{A.11}$$

where dotted $\dot{\chi}_\alpha$ is the thermoacoustic function χ_α rewritten by Nu. If the relation of Equation (A.11) is used in Equation A.4, $1/R_{\mathrm{P}}$ becomes a function of the velocity amplitude.

For stacked-screen regenerator, empirical equations of Nusselt number had been provided by Swift & Ward [37], Tanaka et al. [32], and Gedeon & Wood [33]. Those empirical equations are respectively expressed as follows:

$$Nu_{\mathrm{S}} = \left(3.81 - 11.29\phi + 9.47\phi^2\right)\sigma^{\frac{1}{3}}\left(1 + Re_{\mathrm{h}}^{3/5}\right), \tag{A.12}$$

$$Nu_{\mathrm{T}} = 0.33 {Re_{\mathrm{h}}}^{0.67}, \text{ and} \tag{A.13}$$

$$Nu_{\mathrm{G}} = \left(1 + 0.99\left(Re_{\mathrm{h}}\sigma\right)^{0.66}\right)\phi^{1.79}, \tag{A.14}$$

where subscripts S, T, and G of Nu denote empirical equations of Nusselt number respectively propused by Swift & Ward, Tanaka et al., and Gedeon. With the relation between Nu and χ_α of Equation (A.11), the thermal-relaxation resistance $1/R_{\mathrm{P}}$ of Equation (A.4) is thus able to be given by Nusselt number equations listed above.

Figure A.7 plots experimental data of $1/R_{\mathrm{P}}$ of the uniform temperature regenerator of #30 tested in pressurized Ar at 0.45 MPa of 100 Hz again, which shows comparisons between experimental results of $1/R_{\mathrm{P}}$ and predictions based on those $Nu - Re_{\mathrm{h}}$ correlations. Comparisons are unsatisfactory in both tendency and accuracy. It is obvious that experimental $1/R_{\mathrm{P}}$ coincide with a certain non-zero value when velocity amplitude $|V|$ is extremely small. However, All of the predictions based on proposed empirical equations of Nusselt number is started from exceedingly small $1/R_{\mathrm{P}}$ with the increase of $|V|$. Also, general trends along the velocity amplitude of those predictions are totally different from obtained experimental results. The result of Figure A.7 indicates that listed Nusselt number correlations above are incapable of evaluating the thermal-relaxation loss of the stacked-screen regenerator. A new empirical formulation for evaluating the thermal-relaxation resistance of the stacked-screen regenerator is urgent.

Because obtained experimental results of thermal relaxation resistance presents a linear velocity dependence with a intercept in the plot of $1/R_\mathrm{P}$ vs $|V|$, the thermoacoustic function χ_α is supposed to be parted to two for respectively describing the intercept and the velocity amplitude dependence, in order to empirically formulate $1/R_\mathrm{P}$ of the stacked-screen regenerator. The thermal relaxation resistance is therefore given as follows:

$$\left(\frac{1}{R_\mathrm{P}}\right)_\mathrm{Emp.} = \frac{\gamma - 1}{\gamma}\frac{\omega A}{P_\mathrm{m}}\left(\mathrm{Im}\left[\chi_\alpha\right] + \mathrm{Im}\left[\dot{\chi_\alpha}\right]\right). \tag{A.15}$$

By fitting the equation above to present experimental data, χ_α in Equation (A.15) is estimated from cylindrical flow channels with radius r, using an empirical radius determined as $\sqrt{\mathfrak{p}^2 + d_\mathrm{w}^2}/3$, and Nusselt number used in $\dot{\chi_\alpha}$ is substituted by the form of an empirical equation proposed by Hilpert [28] as $Nu = 0.001 Re_\mathrm{h} \sigma^{1/3}$, where $\mathfrak{p}$ signifies the lattice pitch of the wire screen of square mesh. Equation (A.15) with attempted empirical radius and Nusselt number correlation demonstrates good empirical fittings to the regenerator of #100 for cases of 120, 160, and 200 Hz, while larger deviations are observed in cases of 44, 60, and 80 Hz. As a result, more experiments with wider ranges of the oscillation frequency, velocity amplitude, and mesh number should be tested for confirming correct parameters and Nusselt number in Equation (A.15).

A.4 Conclusions

The acoustic power dissipation/production across the stacked-screen regenerator was measured in acoustic fields of the elevated specific acoustic impedance. Comparisons between the measured acoustic power dissipation/production and predictions estimated from the cylindrical tube modeling of r_0 with the thermoacoustic theory indicated that the effective radius r_0 successfully captured the nature of thermoacoustic power production, but failed to estimate the thermal-relaxation dissipation of the stacked-screen regenerator in high specific acoustic impedance. By testing the stacked-screen regenerator in the high specific acoustic impedance, measurements of the thermal-relaxation resistance of $1/R_\mathrm{P}$ revealed both dependences on the oscillation frequency and the velocity amplitude.Using the thermoacoustic theory with adjusting the characteristic radius of tortuous flow channels would capable of empirically interpret the oscillation frequency dependence, and Nusselt number formulation may possible to practically realize the velocity amplitude dependence of $1/R_\mathrm{P}$ of the regenerator. However, more experiments with various mesh number, different frequency, and larger velocity amplitude should be conducted for characterizing this property.

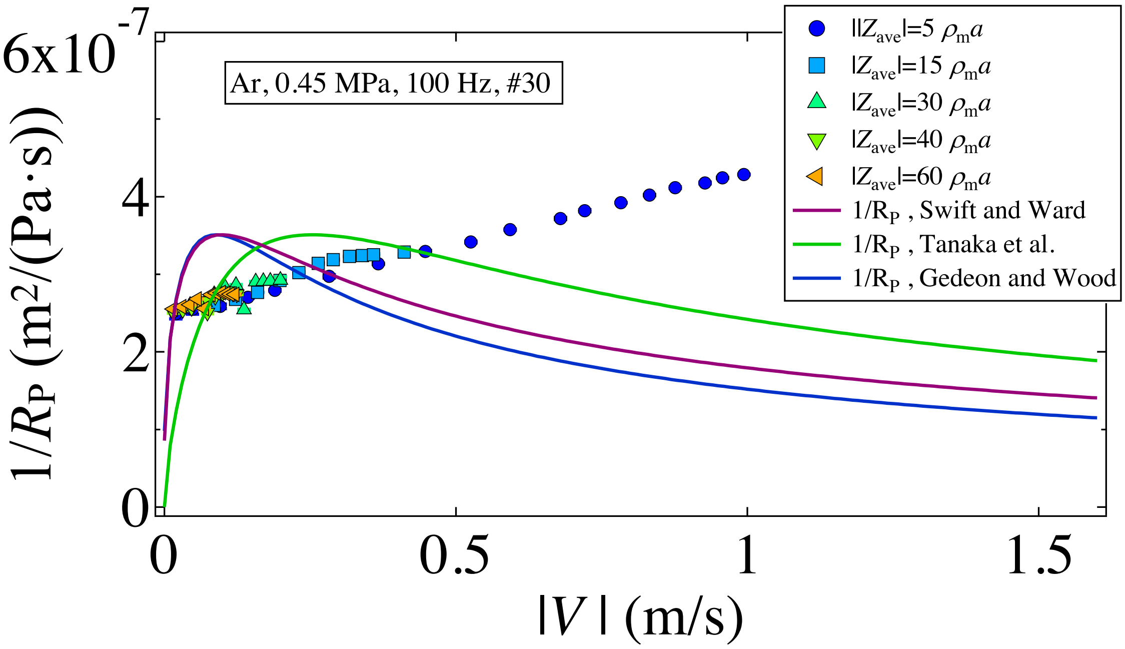

Figure A.7: Experimental results of $1/R_P$ tested with stacked-screen regenerator of #30 mesh. Symbols are measured data, and curves are predictions using empirical equations of Nusselt number respectively proposed by Swift & Ward, Tanaka et al., and Gedeon & Wood.

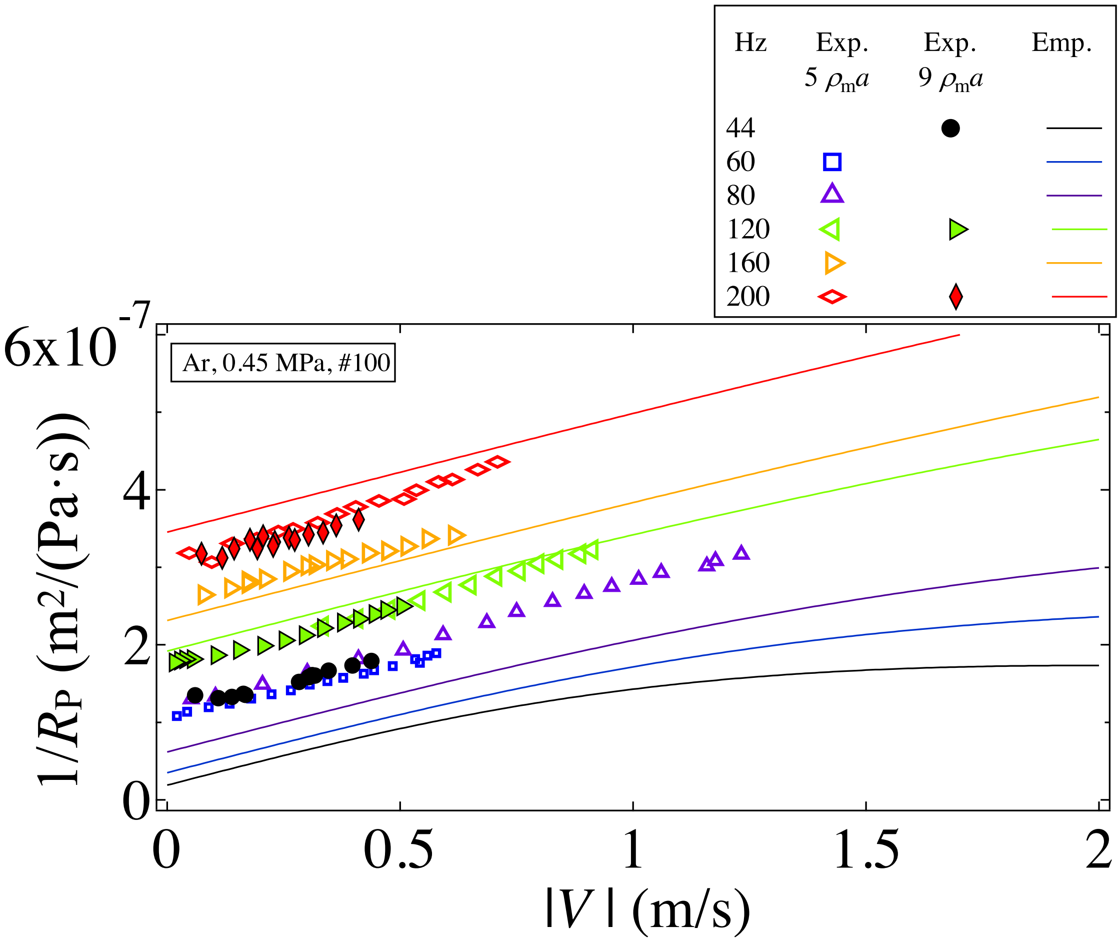

Figure A.8: Experimental results of $1/R_P$ tested with #100 regenerator. Symbols are measured data, and curves are empirical fitting.

Appendix B

Publications

B.1 Journal papers

1. S. H. Hsu, T. Biwa "Measurement of heat flow transmitted through a stacked-screen regenerator of thermoacoustic engine." *Appl. Sci.*, **7**, 303, 2017. dx.doi.org/10.3390/app7030303
2. S. H. Hsu, T. Biwa "Modeling of a stacked-screen regenerator in an oscillatory flow." *Jpn. J. Appl. Phys.*, **56**, 017301, 2016. dx.doi.org/10.7567/JJAP.56.017301
3. 大林敦，許書涵，琵琶哲志 "積層ワイヤーメッシュの熱音響特性の振幅依存性" 低温工学 , **47**, 562-567, 2012. dx.doi.org/10.2221/jcsj.47.562

B.2 Proceedings papers

1. 許書涵，琵琶哲志 "使用於熱聲引擎之金屬網蓄熱器實驗調查" 第二十五屆中華民國振動與噪音工程學術研討會，新北市，台灣，2017。
2. S. H. Hsu, T. Biwa "Measurement of axial heat transport in stacked-screen regenerator of thermoacoustic Stirling engine" The 17th International Stirling Engine Conference, Newcastle upon Tyne, United Kingdom, 2016.
3. S. H. Hsu, T. Biwa "Experimental investigation of stacked-screen regenerator located in a high impedance acoustic field" The 22nd International Congress of Sound and Vibration, Florence, Italy, 2015.
4. S. H. Hsu, T. Biwa "Experiments on thermoacoustic properties of stacked mesh screen" The 24th International Symposium on Transport Phenomena, Yamaguchi, Japan, 2013.
5. 許書涵，大林敦，琵琶哲志 "積層メッシュの熱音響特性評価" 第 17 回動力・動力・エネルギー技術シンポジウム，福岡市，日本，2012.

References

[1] A. Ueda. *Ugetsu Monogatari (雨月物語, Tales of Moonlight and Rain).* 1776.

[2] C. Sondhauss. "Über die schallschwingungen der luft in erhitzten glasröhren und in gedeckten pfeifen von ungleicher weite." *Annalen der Physik*, **155**(1):1–34, 1850. dx.doi.org/10.1002/andp.18501550102

[3] P. L. Rijke. "Notiz über eine neue art, die in einer an beiden enden offenen röhre enthaltene luft in schwingungen zu versetzen." *Annalen der Physik*, **183**(6):339–343, 1859. dx.doi.org/10.1002/andp.18591830616

[4] J. W. S. B. Rayleigh (Lord Rayleigh). *The Theory of Sound (Second edition revised and enlarged)*, volume 2. Macmillan and Co., London, UK, 1896. archive.org/details/theoryofsound02raylrich

[5] N. Rott. "Damped and thermally driven acoustic oscillations in wide and narrow tubes." *ZAMP*, **20**:230–243, 1969. dx.doi.org/10.1007/BF01595562

[6] N. Rott. "Thermally driven acoustic oscillations. part ii: stability limit for helium." *ZAMP*, **24**:230–243, 1973. dx.doi.org/10.1007/BF01593998

[7] N. Rott. "The influence of heat conduction on acoustic streaming." *ZAMP*, **25**:417–421, 1974. dx.doi.org/10.1007/BF01594958

[8] N. Rott. "The heating effect connected with non-linear oscillations in a resonance tube." *ZAMP*, **25**:619–634, 1974. dx.doi.org/10.1007/BF01596123

[9] N. Rott. "Thermally driven acoustic oscillations, part iii: Second-order heat flux." *ZAMP*, **26**:43–49, 1975. dx.doi.org/10.1007/BF01596277

[10] N. Rott and G. Zouzoulas. "Thermally driven acoustic oscillations, part iv: Tubes with variable cross-section." *ZAMP*, **27**:197–224, 1976. dx.doi.org/10.1007/BF01590805

[11] K. W. Taconis, J. J. M. Beenakker, A. O. C. Nier, and L. T. Aldrich. "Measurements concerning the vapour-liquid equilibrum of solutions of He^3 in He^4 below 2.19° K." *Physica*, **15**(8-9):733–739, 1949. doi.org/10.1016/0031-8914(49)90078-6

[12] G. W. Swift. *Thermoacoustics: A Unifying Perspective for Some Engines and Refrigerators*. J. Acoust. Soc. Am., Melville, NY, USA, 2002. dx.doi.org/10.1121/1.1561492

[13] A. Tominaga. *Fundamental Thermoacoustics* （熱音響工学の基礎）. Uchida Rokakuho Publishing Co., Tokyo, Japan, 1998. (In Japanese) www.rokakuho.co.jp/data/books/5079.html

[14] A. Tominaga. “Thermodynamic aspects of thermoacoustic theory.” *Cryogenics*, **35**(7):427–440, 1995. dx.doi.org/10.1016/0011-2275(95)93576-L

[15] J. Wheatley, T. Hofler, G. W. Swift, and A. Migliori. “An intrinsically irreversible thermoacoustic heat engine.” *J. Acoust. Soc. Am.*, **74**(1):153–170, 1983. dx.doi.org/10.1121/1.389624

[16] G. W. Swift. “Thermoacoustic engines.” *J. Acoust. Soc. Am.*, **84**:1145–1180, 1988. dx.doi.org/10.1121/1.396617

[17] P. H. Ceperley. “Pistonless Stirling engine - traveling wave heat engine.” *J. Acoust. Soc. Am.*, **66**(5):1508–1513, 1979. dx.doi.org/10.1121/1.383505

[18] T. Yazaki, A. Iwata, T. Maekawa, and A. Tominaga. “Traveling wave thermoacoustic engine in a looped tube.” *Am. Phys. Soc. (Review letter)*, **81**:3128–3131, 1998. dx.doi.org/10.1103/PhysRevLett.81.3128

[19] S. Backhaus and G. W. Swift. “A thermoacoustic Stirling heat engine.” *Nature*, **399**:335–338, 1999. dx.doi.org/10.1038/20624

[20] K. de Blok. “Low operating temperature integral thermo acoustic devices for solar cooling and waste heat recovery.” *J. Acoust. Soc. Am.*, **123**(5):3541–3541, 2008. dx.doi.org/10.1121/1.2934526

[21] K. de Blok. “Novel 4-stage traveling wave thermoacoustic power generator.” In *Proceedings of ASME*, volume 3, pages 2–4, 2010. dx.doi.org/10.1115/FEDSM-ICNMM2010-30527

[22] K. de Blok. “Multi-stage traveling wave thermoacoustics in practice.” The 19th International Congress of Sound and Vibration, Vilnius, Lithuania, 2012. www.aster-thermoacoustics.com/wp-content/uploads/2013/02/Multi-stage-traveling-wave-feedback-thermoacoustics-in-practice-Kees-de-Blok.pdf

[23] D. L. Gardner and G. W. Swift. “A cascade thermoacoustic engine.” *J. Acoust. Soc. Am.*, **114**:1905–1909, 2003. dx.doi.org/10.1121/1.1612483

[24] T. Biwa, D. Hasegawa, and T. Yazaki. “Low temperature differential thermoacoustic Stirling engine.” *Appl. Phys. Lett.*, **97**:34102, 2010. dx.doi.org/10.1063/1.3464554

[25] L. S. Tong and A. L. London. “Heat-transfer and flow-friction characteristics of woven-screen and cross-rod matrices.” *Trans. ASME*, **10**:1558–1570, 1957. www.dtic.mil/docs/citations/ADA286687

[26] W. M. Kays and A. L. London. *Compact heat exchangers*. McGraw-Hill, New York, NY, USA, 1964. dx.doi.org/10.1115/1.3644004

[27] I. H. Shames. *Mechanics of Fluids*. McGraw-Hill, New York, NY, USA, fourth edition, 2002. highered.mheducation.com/sites/0072472103/index.html

[28] T. L. Bergman, F. P. Incropera, D. P. DeWitt, and A. S. Lavine. *Fundamentals of Heat and Mass Transfer*. John Wiley & Sons, New Jersey, USA, seventh edition, 2011. as.wiley.com/WileyCDA/WileyTitle/productCd-EHEP001810.html

[29] J. M. Kay. *An Introduction to Fluid Mechanics and Heat Transfer: with Applications in Chemical and Mechanical Process Engineering*. Cambridge University Press, Cambridge, England, UK, 1957. dx.doi.org/10.1119/1.1986503

[30] G. Rice, J. C. T. Thonger, and M. W. Dadd. "Regenerator effectiveness measurements." In *Proc. 20th IECEC*, volume 3, page 266, 1985.

[31] H. Miyabe, K. Hamaguchi, and K. Takahashi. "An approach to the design of Stirling engine regenerator matrix using packs of wire gauzes." In *Proc., Intersoc. Energy Convers. Eng. Conf.;(United States)*, volume 4. Department of Mechanical Engineering, Meiji University, 1-1-1 Higashimita Tama-ku, Kawasaki-shi, 1982. www.osti.gov/scitech/biblio/5411939

[32] M. Tanaka, I. Yamashita, and F. Chisaka. "Flow and heat transfer characteristics of the Stirling engine regenerator in an oscillating flow." *JSME Int. J.*, **33**:283–289, 1990. dx.doi.org/10.1299/jsmeb1988.33.2_283

[33] D. Gedeon and J. G. Wood. *Oscillating-flow regenerator test rig: hardware and theory with derived correlations for screens and felts*. NASA Contractor Report 198442; NASA-Lewis Research Center, Cleveland, OH, USA, 1996. archive.org/details/nasa_techdoc_19960015878

[34] S. Isshiki, A. Sakano, I. Ushiyama, and N. Isshiki. "Studies on flow resistance and heat transfer of regenerator wire meshes of stirling engine in oscillatory flow." *JSME Int. J. B. Fluid T.*, **40**(2):281–289, 1997. dx.doi.org/10.1299/jsmeb.40.281

[35] T. S. Zhao and P. Cheng. "Oscillatory pressure drops through a woven-screen packed column subjected to a cyclic flow." *Cryogenics*, **36**:333–341, 1996. dx.doi.org/10.1016/0011-2275(96)81103-9

[36] T. S. Zhao and P. Cheng. "Oscillatory heat transfer in a pipe subjected to a laminar reciprocating flow." *J. Heat transfer*, **118**:592–597, 1996. dx.doi.org/10.1115/1.2822673

[37] G. W. Swift and W. C. Ward. "Simple harmonic analysis of regenerators." *J. Therm. Heat Transf.*, **10**(4):652–662, 1996. dx.doi.org/10.2514/3.842

[38] B. Ward, J. Clark, and G. W. Swift. *Design Environment for Low-amplitude Thermoacoustic Energy Conversion DeltaEC Version 6.3b11 Users Guide*. Los Alamos National Laboratory, Los Alamos, NM, USA, 2012. dx.doi.org/10.1121/1.2942768

[39] G. Kirchhoff. "Ueber den einfluss der wärmeleitung in einem gase auf die schallbewegung." *Annalen der Physik*, **210**(6):177–193, 1868. dx.doi.org/10.1002/andp.18682100602

[40] C. W. Kosten and C. Zwikker. *Sound absorbing materials*. Elsevier, Amsterdam, Netherlands, 1949. catalog.hathitrust.org/Record/001479870

[41] K. Attenborough. "Acoustical characteristics of rigid fibrous absorbents and granular materials." *J. Acoust. Soc. Am.*, **73**(3):785–799, 1983. dx.doi.org/10.1121/1.389045

[42] Y. Champoux and M. R. Stinson. "On acoustical models for sound propagation in rigid frame porous materials and the influence of shape factors." *J. Acoust. Soc. Am.*, **92**(2):1120–1131, 1992. dx.doi.org/10.1121/1.405281

[43] J. F. Allard and Y. Champoux. "New empirical equations for sound propagation in rigid frame fibrous materials." *J. Acoust. Soc. Am.*, **91**(6):3346–3353, 1992. dx.doi.org/10.1121/1.402824

[44] L. A. Wilen. "Measurements of thermoacoustic functions for single pores." *J. Acoust. Soc. Am.*, **103**(3):1406–1412, 1998. dx.doi.org/10.1121/1.421299

[45] L. A. Wilen. "Dynamic measurements of the thermal dissipation function of reticulated vitreous carbon." *J. Acoust. Soc. Am.*, **109**(1):179–184, 2001. dx.doi.org/10.1121/1.1333422

[46] A. Petculescu and L. A. Wilen. "Lumped-element technique for the measurement of complex density." *J. Acoust. Soc. Am.*, **110**:1950–1957, 2001. dx.doi.org/10.1121/1.1401743

[47] H. S. Roh, R. Raspet, and H. E. Bass. "Parallel capillary-tube-based extension of thermoacoustic theory for random porous media." *J. Acoust. Soc. Am.*, **121**(3):1413–1422, 2007. dx.doi.org/10.1121/1.2436632

[48] H. S. Roh. "Experimental and theoretical temperature gradient coefficient in thermoacoustics." *Acta. Acust. United. Ac.*, **94**(4):636–640, 2008. doi.org/10.3813/AAA.918073

[49] Y. Ueda, T. Kato, and C. Kato. "Experimental evaluation of the acoustic properties of stacked-screen regenerators." *J. Acoust. Soc. Am.*, **125**:780–786, 2009. dx.doi.org/10.1121/1.3056552

[50] B. H. Song and J. S. Bolton. "A transfer-matrix approach for estimating the characteristic impedance and wave numbers of limp and rigid porous materials." *J. Acoust. Soc. Am.*, **107**(3):1131–1152, 2000. dx.doi.org/10.1121/1.428404

[51] A. Obayashi, S. H. Hsu, and T. Biwa. "Amplitude dependence of thermoacousic properties of stacked wire meshes." *J. Cryo. Soc. Jpn.*, **47**:562–567, 2012. (In Japanese) doi.org/10.2221/jcsj.47.562

[52] M. Guédra, F. C. Bannwart, G. Penelet, and P. Lotton. "Parameter estimation for the characterization of thermoacoustic stacks and regenerators." *Appl. Therm. Eng.*, **80**:229–237, 2015. dx.doi.org/10.1016/j.applthermaleng.2015.01.058

[53] J. R. Olson and G. W. Swift. "Similitude in thermoacoustics." *J. Acoust. Soc. Am.*, **95**(3):1405–1412, 1994. dx.doi.org/10.1121/1.407845

[54] H. J. Spurk and N. Aksel. *Fluid Mechanics*. Springer, Berlin, Heidelberg, Germany, second edition, 2008. dx.doi.org/10.1007/978-3-642-58277-6

[55] S. Choi, K. Nam and S. Jeong. "Investigation on the pressure drop characteristics of cryocooler regenerators under oscillating flow and pulsating pressure conditions." *Cryogenics*, **44**:203–310, 2004. doi.org/10.1016/j.cryogenics.2003.11.006

[56] C. Lawn. "Acoustic pressure losses in woven screen regenerators." *Appl. Acoust.*, **77**:42–48, 2014. doi.org/10.1016/j.apacoust.2013.09.019

[57] S. H. Hsu and T. Biwa "Modeling of a stacked-screen regenerator in an oscillatory flow." *Jpn. J. Appl. Phys.*, **56**:017301, 2016. dx.doi.org/10.7567/JJAP.56.017301

[58] A. Fusco, W. Ward, and G. W. Swift. "Two-sensor power measurements in lossy ducts." *J. Acoust. Soc. Am.*, **91**:2229–2235, 1992. dx.doi.org/10.1121/1.403656

[59] T. Biwa, Y. Tashiro, H. Nomura, Y. Ueda, and T. Yazaki. “Experimental verification of a two-sensor acoustic intensity measurement in lossy ducts.” *J. Acoust. Soc. Am.*, **124**:1584–1590, 2008. dx.doi.org/10.1121/1.2953311

[60] Y. Ueda. “Calculation method for the prediction of the performance of a traveling-wave thermoacoustic cooler.” *Journal of Power and Energy Systems*, **5**(2):1276–1282, 2008. doi.org/10.1299/jpes.2.1276

[61] G. Yu W. Dai, E. Luo. “A simple method to determine the frequency of engine-included thermoacoustic systems.” *Cryogenics*, **46**:804–808, 2006. doi.org/10.1016/j.cryogenics.2006.08.002

[62] S. Hasegawa, T. Yamaguchi, and Y. Oshinoya. “A thermoacoustic refrigerator driven by a low temperature- differential, high-efficiency multistage thermoacoustic engine.” *Appl. Therm. Eng.*, **58**:394–399, 2013. doi.org/10.1016/j.applthermaleng.2013.04.030

[63] S. Hasegawa, Y. Ashigaki, and Mariko Senga. “Thermal diffusion effect of a regenerator with complex flow channels.” *Appl. Therm. Eng.*, **104**:237–242, 2016. doi.org/10.1016/j.applthermaleng.2016.05.023

[64] S. H. Hsu and T. Biwa. “Measurement of heat flow transmitted through a stacked-screen regenerator of thermoacoustic engine.” *Appl. Sci.*, **7**:303, 2017. dx.doi.org/10.3390/app7030303

[65] D. Gedeon. *Sage User’s Guide*. Gedeon Associates, Athens, OH, USA, v11 edition, 2016. www.sageofathens.com/Documents/SageStlxHyperlinked.pdf

[66] D. K. Wilson, J. D. McIntosh, and R.F. Lambert. “Forchheimer-type nonlinearities for high-intensity propagation of pure tones in air-saturated porous media.” *J. Acoust. Soc. Am.*, **84**:350–359, 1988. dx.doi.org/10.1121/1.396937

[67] J. D. McIntosh, M. T. Zuroski, and R. F. Lambert. “Standing wave apparatus for measuring fundamental properties of acoustic materials in air.” *J. Acoust. Soc. Am.*, **88**:1929–1938, 1990. dx.doi.org/10.1121/1.400216

[68] J. D. McIntosh and R. F. Lambert. “Nonlinear wave propagation through rigid porous materials. i: Nonlinear parametrization and numerical solutions.” *J. Acoust. Soc. Am.*, **88**:1939–1949, 1990. dx.doi.org/10.1121/1.400217

[69] S. C. Costa, M. Tutar, I. Barreno, J.-A. Esnaola, H. Barrutia, D. García, M. A. González, and J. I. Prieto. “Experimental and numerical flow investigation of Stirling engine regenerator.” *Energy*, **72**:800–812, 2014. doi.org/10.1016/j.energy.2014.06.002

[70] N. Sugimoto and M. Yoshida. “Marginal condition for the onset of thermoacoustic oscillations of a gas in a tube.” *Phys. Fluids*, **19**(7):074101, 2007. dx.doi.org/10.1063/1.2742422

[71] A. A. Atchley and F. M. Kuo. “Stability curves for a thermoacoustic prime mover.” *J. Acoust. Soc. Am.*, **95**(3):1401–1404, 1994. dx.doi.org/10.1121/1.408580

[72] Y. Ueda and C. Kato. “Stability analysis of thermally induced spontaneous gas oscillations in straight and looped tubes.” *J. Acoust. Soc. Am.*, **124**(2):851–858, 2008. dx.doi.org/10.1121/1.2939134

[73] M. Guédra and G. Penelet. “On the use of a complex frequency for the description of thermoacoustic engines.” *Acta. Acust. United. Ac.*, **98**(2):232–241, 2012. doi.org/10.3813/AAA.918508

[74] H. Hyodo and N. Sugimoto. “Stability analysis for the onset of thermoacoustic oscillations in a gas-filled looped tube.” *J. Fluid Mech.*, **741**:585–618, 2014. doi.org/10.1017/jfm.2013.621

[75] J. R. Olson and G. W. Swift. “Energy dissipation in oscillating flow through straight and coiled pipes.” *J. Acoust. Soc. Am.*, **100**(4):2123–2131, 1996. dx.doi.org/10.1121/1.417922

[76] S. Backhaus and G. W. Swift. “A thermoacoustic-Stirling heat engine: detail study.” *J. Acoust. Soc. Am.*, **107**(6):3148–3166, 2000. dx.doi.org/10.1121/1.429343

[77] B. L. Smith and G. W. Swift. “Measuring second-order time-average pressure.” *J. Acoust. Soc. Am.*, **110**(2):717–723, 2001. dx.doi.org/10.1121/1.1382615

[78] B. L. Smith and G. W. Swift. “Power dissipation and time-averaged pressure in oscillating flow through a sudden area change.” *J. Acoust. Soc. Am.*, **113**(5):2455–2463, 2003. dx.doi.org/10.1121/1.1564022

[79] T. Yazaki and A. Tominaga. “Measurement of sound generation in thermoacoustic oscillations.” In *Proceedings of the Royal Society of London A: Mathematical, Physical and Engineering Sciences*, volume 454, pages 2113–2122. The Royal Society, 1998. dx.doi.org/10.1098/rspa.1998.0251

[80] V. E. Gusev, H. Bailliet, P. Lotton, S. Job, and M. Bruneau. “Enhancement of the Q of a nonlinear acoustic resonator by active suppression of harmonics.” *J. Acoust. Soc. Am.*, **103**(6):3717–3720, 1998. dx.doi.org/10.1121/1.423090

[81] V. Gusev, S. Job, H. Bailliet, P. Lotton, and M. Bruneau. “Acoustic streaming in annular thermoacoustic prime-movers.” *J. Acoust. Soc. Am.*, **108**(3):934–945, 2000. dx.doi.org/10.1121/1.1287023

[82] H. Bailliet, V. Gusev, R. Raspet, and R. A. Hiller. “Acoustic streaming in closed thermoacoustic devices.” *J. Acoust. Soc. Am.*, **110**(4):1808–1821, 2001. dx.doi.org/10.1121/1.1394739

[83] J. R. Olson and G. W. Swift. “Suppression of acoustic streaming in tapered pulse tubes.” In *Cryocoolers 10*, pages 307–313. Springer, 2002. doi.org/10.1007/0-306-47090-X_36

[84] D. Gedeon. “DC gas flows in Stirling and pulse-tube cryocoolers.” *Cryocoolers*, **9**:385–392, 1997. doi.org/10.1007/978-1-4615-5869-9_45

[85] A. Piccolo, R. Siclari, F. Rando, and M. Cannistraro. “Comparative performance of thermoacoustic heat exchangers with different pore geometries in oscillatory flow. implementation of experimental techniques.” *Appl. Sci.*, **7**(8):784, 2017. dx.doi.org/10.3390/app7080784

[86] M. A. Lewis, T. Kuriyama, F. Kuriyama, and R. Radebaugh. “Measurement of heat conduction through stacked screens.” In *Advances in cryogenic engineering*, pages 1611–1618. Springer, 1998. doi.org/10.1007/978-1-4757-9047-4_202

[87] M. Guédra, G. Penelet, P. Lotton, and J. P. Dalmont. "Theoretical prediction of the onset of thermoacoustic instability from the experimental transfer matrix of a thermoacoustic core." *J. Acoust. Soc. Am.*, **130**(1):145–152, 2011. dx.doi.org/10.1121/1.3592227

[88] W. Dai, E. Luo, Y. Zhang, and H. Ling. "Detailed study of a traveling wave thermoacoustic refrigerator driven by a traveling wave thermoacoustic engine." *J. Acoust. Soc. Am.*, **119**(5):2686–2692, 2006. dx.doi.org/10.1121/1.2184267

[89] W. Dai H. Ling, E. Luo. "A numerical simulation method and analysis of a complete thermoacoustic-stirling engine." *Ultrasonics*, **44**:e1511–e1514, 2006. doi.org/10.1016/j.ultras.2006.08.007

[90] Q. Tu, Q. Li, F. Wu, and F. Z. Guo. "Network model approach for calculating oscillating frequency of thermoacoustic prime mover." *Cryogenics*, **43**(6):351–357, 2003. doi.org/10.1016/S0011-2275(03)00090-0

[91] P. Blanc-Benon, E. Besnoin, and O. Knio. "Experimental and computational visualization of the flow field in a thermoacoustic stack." *Comptes Rendus Mecanique*, **331**(1):17–24, 2003. doi.org/10.1016/S1631-0721(02)00002-5

[92] C. Scalo, S. K. Lele, and L. Hesselink. "Linear and nonlinear modelling of a theoretical travelling-wave thermoacoustic heat engine." *J. Fluid Mech.*, **766**:368–404, 2015. doi.org/10.1017/jfm.2014.745

[93] V. Gusev, P. Lotton, H. Bailliet, S. Job, and M. Bruneau. "Thermal wave harmonics generation in the hydrodynamical heat transport in thermoacoustics." *J. Acoust. Soc. Am.*, **109**(1):84–90, 2001. /dx.doi.org/10.1121/1.1332383

[94] S. H. Hsu and T. Biwa. "Experimental investigation of stacked-screen regenerator located in a high impedance acoustic field." The 22nd International Congress of Sound and Vibration, Florence, Italy, 2015.

[95] J. Liu and S. L. Garrett. "Relationship between Nusselt number and the thermoviscous (Rott) functions." *J. Acoust. Soc. Am.*, **119**:1457–1462, 2006. dx.doi.org/10.1121/1.2165000

Acknowledgements

English translation:

Noting a sigh

Life is like a silkworm in the spring season
Self-bounding within a cocoon
Once antennae and wings mature
Breaking free from the bind will also be by itself

—LU You (1125–1209,
in the period of the Southern Song Dynasty of China)

〈書歎〉[1]
人生如春蠶
作繭自纏裹
一朝眉羽成
鑽破亦在我
|南宋|陸游

On my journey of pursuing Ph.D. degree, I am the self-bounding silkworm toward the inner metamorphoses, as this little poetry described. The road upward to reach is long. Upon the journey, there are dark and obstacles in front of me, through which I have to make my way.

I owe my deepest gratitude to my parents for that they give me the perseverance character trait running in my blood. This personality always drives me forward. Thanks for their understanding and encouragement in any of my undertakings, my accomplishment of Ph.D. would not have been possible without their incomparable love and financial support.

As the only guide who helps me to come through those dark and obstacles into a sunlight broader, I would like to express my great appreciation to my supervisor—Professor BIWA Tetsushi. It is he, who has given me the invaluable opportunity to come and study at Tohoku University. The Greek philosopher Aristotle says: *Plato is dear to me, but dearer still is truth.* Professor BIWA Tetsushi plays a mentor role as like Plato, in my opinion. Without saying his coaching, patience, encouragement, and feedback to me, it is worth mentioning that he has been very tolerant of me to be contrary to his comments and allowed me to conduct research in an independent manner, for which I am very grateful.

I would like to extend my sincere thanks to Professor FUKUNISHI Yu of Department of Mechanical Systems Engineering of Tohoku University and Professor NAGAI Hiroki of Institute of Fluid Science of Tohoku University for serving on my doctoral thesis committee members. I am very appreciative of their valuable pieces of advice and suggestions.

Also, I would like to thank all of the former and present members of BIWA laboratory for contributing to my master and doctor careers significantly through enjoyable hours of discussion and problem-solving.

Lastly, I give thanks to myself. I most admire the self-challenging spirit expressed by the little poetry in the beginning of this page. On the way of life, a man should orientate himself toward striving, because it is the only way to make himself superiority. On the journey of my life, Ph.D. is just one of destinations. Fighting on the way to the superior self is my ultimate destiny.

---

[1] Cited from《劍南詩稿》(Jian Nan Shi Gao, the draft of poems when holding a sword in the southern borders).

Vita

HSU Shu Han

HSU Shu Han （許書涵） was born on 1985 and grew up in Banqiao, Taipei (renamed as Banqiao District, New Taipei City in 2010), Taiwan. In 2004, he graduated from Hai Shan (renamed as New Taipei in 2010) Industrial Vocational High School in Tucheng, Taipei, and began his undergraduate studies in Department Mechanical Engineering of National Taipei University of Technology in Taiwan.

In 2007, HSU Shu Han received his Bachelor of engineering degree and undertaken his alternative military service for one year. After finished his military service, he was hired by a company and worked as a project manager and a mechanical engineer for designing commercial backlight modules used in thin film transistor liquid crystal display industry.

Later, HSU Shu Han decided to *march to his own drummer*[2] and to pursue an advanced degree in Tohoku University, Japan. With continuous struggles of learning Japanese and preparations of studying abroad, he passed the admission examination and enrolled the master program in Department of Mechanical Systems Engineering of Tohoku University in April 2011, soon after the aftermath of 311 Tohoku earthquake and tsunami（東日本大震災）. He embarked on the work of characterization the stacked-screen regenerator used in thermoacoustic engines as the beginning of his academic research.

In 2013, HSU Shu Han completed his master thesis titled as “Experiments on Thermoacoustic Properties of Stacked Mesh Screens”（積層した金属ワイヤメッシュの熱音響特性の実験的研究）, and thereafter began his doctoral study at Tohoku University for conducting the same research subject in depth.

---

[2] Quotation from David Thoreau, American essayist and poet (1817–1862).